



# Complex oscillations with multiple timescales - Application to neuronal dynamics

Mathieu Desroches

## ► To cite this version:

Mathieu Desroches. Complex oscillations with multiple timescales - Application to neuronal dynamics . Dynamical Systems [math.DS]. Université Pierre et Marie Curie, 2015. <tel-01254956>

**HAL Id: tel-01254956**

**<https://hal.inria.fr/tel-01254956>**

Submitted on 12 Jan 2016

**HAL** is a multi-disciplinary open access archive for the deposit and dissemination of scientific research documents, whether they are published or not. The documents may come from teaching and research institutions in France or abroad, or from public or private research centers.

L'archive ouverte pluridisciplinaire **HAL**, est destinée au dépôt et à la diffusion de documents scientifiques de niveau recherche, publiés ou non, émanant des établissements d'enseignement et de recherche français ou étrangers, des laboratoires publics ou privés.

UNIVERSITÉ PIERRE ET MARIE CURIE - PARIS 6

Mémoire présenté pour obtenir  
**le diplôme d'habilitation à diriger des recherches**  
de l'Université Pierre et Marie Curie - Paris 6

Spécialité : Mathématiques

par

**Mathieu DESROCHES**

*Chargé de Recherche Inria*

**Complex oscillations with multiple timescales**  
**Application to neuronal dynamics**

**Rapporteurs :**

EUSEBIUS J. DOEDEL, Professeur (Concordia University, Montréal, Canada)

CHRISTOPHER K. R. T. JONES, Professeur (University of North Carolina at Chapel Hill, USA)

DANIEL PANAZZOLO, Professeur (Université de Haute-Alsace, France)

**Soutenance le vendredi 11 décembre 2015 devant un jury composé de :**

STEPHEN COOMBES, Professeur, examinateur (University of Nottingham, UK)

PETER DE MAESSCHALCK, Professeur, examinateur (Universiteit Hasselt, België)

OLIVIER FAUGERAS, Directeur de Recherche Inria, examinateur (Inria Sophia Antipolis, France)

JEAN-PIERRE FRANÇOISE, Professeur, président du jury (Université Pierre & Marie Curie, France)

CHRISTOPHER K. R. T. JONES, Professeur, rapporteur (University of North Carolina, USA)

DANIEL PANAZOLLO, Professeur, rapporteur (Université de Haute-Alsace, France)



# CONTENTS

0	OUTLINE	1
1	INTRODUCTION	2
1.1	Slow-fast dynamical systems and canards	2
1.1.1	The critical manifold and the slow flow	3
1.1.2	The canard phenomenon	6
1.2	Numerical continuation methods	9
2	“ONE SLOW/ONE FAST” SYSTEMS: CANARD EXPLOSIONS	11
2.1	Numerical continuation techniques for planar slow-fast systems	11
2.1.1	Numerical continuation as a well-suited tool for slow-fast systems	11
2.1.2	Limit cycles in some slow-fast Liénard systems	12
2.2	Canards and inflection lines	20
2.2.1	The inflection-line method and its formulation in terms of singularity theory	20
2.2.2	The “smallness” of $\varepsilon$	28
2.2.3	Application to neuronal excitability	30
3	“TWO SLOW/ONE FAST” SYSTEMS: CANARD-INDUCED MMOS	39
3.1	Slow-fast mechanisms for MMOs; application to neuronal dynamics	40
3.1.1	Three main slow-fast scenarios	40
3.1.2	MMOs in a reduced Hodgkin–Huxley system	45
3.2	Computing slow manifolds and canards in MMO systems	48
3.2.1	A Boundary-Value Problem approach	49
3.2.2	Finding and following canard orbits	51
3.3	Extending the inflection-line method to folded-node systems	53
4	“ONE SLOW/TWO FAST” SYSTEMS: CANARDS AND BURSTING	57
4.1	Introduction to bursting	57
4.2	Spike-adding canard explosion in square-wave bursters	58
4.3	From spiking to bursting: torus canards	62
5	“TWO SLOW/TWO FAST” SYSTEMS: BURSTING WITH FOLDED SINGULARITIES	65
5.1	Mixed-Mode Bursting Oscillations (MMBOs)	65
5.1.1	MMBOs as a slow passage through a spike-adding canard explosion	67
5.1.2	Controlling the number of SAOs in MMBOs using folded node theory	69
5.2	Spike-adding mechanism in parabolic bursters	71
5.2.1	Plant’s model and its new polynomial approximation	74
5.2.2	Rinzel’s three-dimensional theta model	81
	BIBLIOGRAPHY	86



## LIST OF FIGURES

Figure 1	Phase portraits of the Van der Pol equation (7) for $\lambda = 0$ (a) and for $\lambda = 1$ (b).	5
Figure 2	Canard explosion at the lower fold in the van der Pol system. . . . .	6
Figure 3	Critical manifold and slow flow near a folded node. . . . .	8
Figure 4	Backward and forward integrating two orbits through $(0, Y_1)$ and $(0, Y_2)$ . . .	14
Figure 5	The canard curve of (20), for $\varepsilon = 0.1$ . . . . .	15
Figure 6	Left: The canard curve of (20), for $\varepsilon = 0.03$ . Right: $\varepsilon$ -location of the folds. . . .	16
Figure 7	(a) Curve $b = b(Y)$ in the $F^\#$ -system [102] for $\varepsilon = 0.003$ ; (b) Enlargement. . . .	17
Figure 8	(a) Branch of limit cycles in the $F^\#$ -system for different $\varepsilon$ ; (b) Magnification. . .	18
Figure 9	Locus of fold bifurcations of limit cycles in the two-parameter plane $(b, \varepsilon)$ . . .	19
Figure 10	Canard explosion in the 2D Hodgkin-Huxley model. . . . .	21
Figure 11	Inflection sets $I_0$ for $\varepsilon = 0$ computed in the FitzHugh-Nagumo system (71)-(72). .	23
Figure 12	Inflection sets $I_\varepsilon$ for $\varepsilon > 0$ , computed in the FHN system (71)-(72). . . . .	24
Figure 13	Inflection lines $I_\varepsilon$ for $\varepsilon > 0$ just before the transition focus-node: $ \alpha  < \sqrt{\varepsilon}$ . . .	25
Figure 14	Inflection lines $I_\varepsilon$ for $\varepsilon > 0$ at the transition focus-node: $ \alpha  = \sqrt{\varepsilon}$ . . . . .	26
Figure 15	Inflection lines $I_\varepsilon$ for $\varepsilon > 0$ just after the transition focus-node: $ \alpha  > \sqrt{\varepsilon}$ . . . .	27
Figure 16	Local curvature of a canard with head and a headless canard near $S^r$ . . . . .	28
Figure 17	Limit cycles of the VDP system with inflection curves for different $\varepsilon$ . . . . .	29
Figure 18	Inflection curves of VDP for different $\varepsilon$ -values from 0.01 to 0.25. . . . .	30
Figure 19	Inflection curves in the classical FitzHugh-Nagumo equations. . . . .	31
Figure 20	Inflection lines of the 2D Hodgkin-Huxley model together with canard cycles. . . .	33
Figure 21	Excitability threshold and the inflection line: (a) integrator, (b) resonator. . . . .	36
Figure 22	Headless canard cycle of the FHN system crossing the inflection line. . . . .	37
Figure 23	Slow manifolds of (100) with $\nu = 0.025$ in a neighborhood of the folded node. . .	41
Figure 24	Numerical study of the number of rotational sectors for (100) with $\nu = 0.025$ . . . .	42
Figure 25	Candidate periodic orbit $\Gamma_c$ that gives rise to MMOs near a folded node. . . . .	43
Figure 26	Secondary canards $\xi_5$ and $\xi_6$ of the 3D reduced Hodgkin-Huxley model (101) . . . .	46
Figure 27	Bifurcation diagram in $I$ and MMOs of the 3D reduced HH model (101). . . . .	47
Figure 28	Computation of slow manifolds by numerical continuation of BVPs. . . . .	51
Figure 29	Continuation of secondary canards of the Koper model (103). . . . .	52
Figure 30	Figure extracted from Golubitsky and Schaeffer [58]. . . . .	54
Figure 31	Inflection curve configuration near a folded-node singularity. . . . .	55
Figure 32	HR burster: Bifurcation diagram in $z$ and phase portraits of the fast subsystem. .	59
Figure 33	First spike-adding canard explosion in the HR burster. . . . .	60
Figure 34	Second spike-adding canard explosion in the HR burster. . . . .	61
Figure 35	Example of sub-Hopf/fold cycle bursting in the HR burster. . . . .	62
Figure 36	Bifurcation diagram in $b_1$ of the HR system (144) at $s = -1.95$ . . . . .	63
Figure 37	Torus canards (with and without head) in the HR system (144) at $s = -1.95$ . . .	64
Figure 38	Example of MMBO in the extended HR model (146)-(149) . . . . .	66
Figure 39	Periodic MMBOs of system (146)-(149) for different $(k, \varepsilon)$ -values. . . . .	68
Figure 40	Periodic MMBOs of system (146)-(149) for different $k$ -values and $\varepsilon = 10^{-5}$ . . .	69
Figure 41	Periodic $192^3$ -MMBOs of system (146)-(149) for $k = 0.45$ and $\varepsilon = 10^{-5}$ . . . .	71
Figure 42	Bursting solution of Plant's model (42) containing a canard segment. . . . .	73
Figure 43	Slow flow and flow of the DRS of Plant's model (42): folded saddle. . . . .	75
Figure 44	Slow flow of the canonical parabolic bursting model (164). . . . .	77
Figure 45	Spike-adding (folded-saddle) canard explosion in the canonical model (164). . . .	79
Figure 46	Solution of Rinzel's theta model (180) containing a canard segment. . . . .	83
Figure 47	Solutions of Rinzel's theta model (180) corresponding to case 2. . . . .	84

Figure 48	Continuous (Plant's model) vs. discontinuous (Rinzel's model) spike-adding.	85
-----------	---	----

## ACRONYMS

---

BVP	Boundary-Value Problem
DAE	Differential Algebraic Equation
DRS	Desingularised Reduced System
FHN	FitzHugh-Nagumo
GSPT	Geometric Singular Perturbation Theory
HR	Hindmarsh-Rose
HH	Hodgkin-Huxley
IDE	Implicit Differential Equation
LAO	Large-Amplitude Oscillation
MMO	Mixed-Mode Oscillation
MMBO	Mixed-Mode Bursting Oscillation
PWL	PieceWise-Linear
SAO	Small-Amplitude Oscillation

## OUTLINE

---

The main topics to be discussed in this thesis are briefly introduced in Chapter 1. Namely, multiple time scale dynamical systems near non-hyperbolic points, giving rise to canard-type solutions, and numerical continuation methods adapted for such systems both from the viewpoint of bifurcation structures and that of (locally) invariant objects. The results presented in this manuscript correspond to the published papers [3, 23, 24, 25, 27, 28, 29, 30] and to the submitted work [31].

Chapter 2 is dedicated to planar slow-fast systems displaying a canard explosion. We first investigate the use of standard numerical continuation tools in order to compute canard cycles. This can be usefully applied to theoretical problems —e.g. finding “more limit cycles than expected” in Liénard systems, in relation to Hilbert 16<sup>th</sup> problem— and applied problems such as the generation of action potentials in planar neuronal models like, e.g., the FitzHugh-Nagumo (FHN) model or a reduction of the famous Hodgkin-Huxley (HH) model. We then present results relating the geometry of inflection lines of the flow in such systems, with the presence of canard cycles and, in the neuronal context, with the approximation of excitability thresholds.

Chapter 3 is focused on “two slow/one fast” systems displaying Mixed-Mode Oscillations (MMOs). For systems possessing multiple time scales, MMOs have been shown to result from a local passage near a folded singularity and a global return mechanism. After recalling the main theoretical results linking MMOs to slow-fast dynamical objects, we present a numerical approach based on the continuation of parametrised families of two-point Boundary-Value Problems (BVPs) to compute two-dimensional slow manifolds and their transversal intersection curves, which correspond to canards in this three-dimensional context. This method is then adapted to compute branches of canard solutions in parameter space. Finally, we present a first attempt to study the geometry of inflection lines near a folded singularity of node type.

Chapter 4 is dedicated to bursting oscillations in systems with one slow and two fast variables, concentrating on the spike-adding mechanism by which the number of spikes per burst can change upon parameter variation. Due to the time scale separation and to the geometry of the problem, this spike-adding mechanism often involves canard solutions. After briefly recalling the main slow-fast formalism used to understand bursting oscillations since the seminal work of Rinzel in the 1980s, we review the spike-adding canard explosion mechanism as an extension of the classical canard explosion in planar Van der Pol type systems. We then briefly remark that spike-adding via canards can also occur at the level of homoclinic connections, and subsequently we introduce the concept of torus canards which are canard solutions within fast oscillations in bursting systems and organise, in many neuronal systems, the transition from the spiking regime to the bursting regime. We finally analyse an example of neuronal burster displaying torus canards solutions, namely, the Hindmarsh-Rose model.

In Chapter 5, we present a recent work on systems with two slow variables and two fast variables, combining canard phenomena related both to “two slow/one fast” systems (due to the presence of a folded singularity) and to “one slow/two fast” systems (due to a spike-adding canard explosion). We treat two cases: first, the combination of folded-node dynamics with square-wave bursting, which produces new types of complex oscillations with multiple time scales that we term Mixed-Mode Bursting Oscillations (MMBOs); second, the combination of folded-saddle dynamics with a SNIC (Saddle-Node on an Invariant Circle) oscillator, which produces parabolic bursting oscillations. In the latter case, we also show that for all parabolic bursters that we could investigate, the spike-adding mechanism is the one described above, which provides a new level of description of this important class of bursting systems.

## INTRODUCTION

---

The geometry of multiple time scale dynamical systems is intricate. Beginning with the work of the “Strasbourg” school [33] and Takens’ work [145] on “constrained vector fields” in the 1970’s, geometric methods have been used to study generic multiple time scale systems with two slow variables and one fast variable. *Canard points* and *folded singularities* are a prominent phenomenon in the present work. They lie on a fold of the *critical manifold*, where an attracting and a repelling sheet meet. Furthermore, they yield equilibria of a *Desingularized Reduced system (DRS)* that is constructed in the singular limit of the time scale parameter. More recently, Dumortier and Roussarie [41], and Krupa, Szmolyan and Wechselberger [93, 144] introduced singular blow-up techniques for the analytical study of the dynamics near these special points. These methods give information about *canard orbits* that connect attracting and repelling *slow manifolds*. Complementary to theoretical advances in the analysis of slow-fast systems, numerical methods have been developed to compute and visualize geometric structures that shape the dynamics of these systems. Slow manifolds and canard orbits can now be computed in concrete systems; see Guckenheimer [62, 65] and Desroches, Krauskopf and Osinga [24, 25, 26, 27]. The combination of new theory and new numerics has produced new understanding of complex oscillations with multiple time scales, in particular *Mixed-Mode Oscillations (MMOs)* in systems with at least two variables and one fast variable, and *bursting oscillations* in systems with one slow and at least two fast variables. Canard phenomena are crucial to understand the geometry of these complicated solutions and their organisation in parameter space. Beyond interesting mathematical questions, these complex oscillations appear in many models, in particular in the context of neuroscience.

### 1.1 SLOW-FAST DYNAMICAL SYSTEMS AND CANARDS

We consider here a slow-fast vector field that takes the form

$$\begin{cases} \varepsilon \dot{x} &= \varepsilon \frac{dx}{d\tau} = f(x, y, \lambda, \varepsilon), \\ \dot{y} &= \frac{dy}{d\tau} = g(x, y, \lambda, \varepsilon), \end{cases} \quad (1)$$

where  $(x, y) \in \mathbb{R}^m \times \mathbb{R}^n$  are state space variables,  $\lambda \in \mathbb{R}^p$  are system parameters, and  $\varepsilon$  is a small parameter  $0 < \varepsilon \ll 1$  representing the ratio of time scales. The functions  $f : \mathbb{R}^m \times \mathbb{R}^n \times \mathbb{R}^p \times \mathbb{R} \rightarrow \mathbb{R}^m$  and  $g : \mathbb{R}^m \times \mathbb{R}^n \times \mathbb{R}^p \times \mathbb{R} \rightarrow \mathbb{R}^n$  are assumed to be sufficiently smooth, typically  $C^\infty$ . The variables  $x$  are fast and the variables  $y$  are slow. System (1) can be rescaled to

$$\begin{cases} x' &= \frac{dx}{dt} = f(x, y, \lambda, \varepsilon), \\ y' &= \frac{dy}{dt} = \varepsilon g(x, y, \lambda, \varepsilon), \end{cases} \quad (2)$$

by switching from the slow time scale  $\tau$  to the fast time scale  $t = \tau/\varepsilon$ .

Several viewpoints have been adopted to study slow-fast systems, starting with asymptotic analysis [44, 110] using techniques such as matched asymptotic expansions [83, 96]. *Geometric Singular Perturbation Theory (GSPT)* takes a geometric point of view and focuses upon invariant manifolds, normal forms for singularities and analysis of their unfoldings [2, 52, 79, 80, 148]. Fenichel’s seminal work [52] on invariant manifolds was an initial foundation of GSPT and it is also called Fenichel theory. A third viewpoint was adopted by a group of French mathematicians in Strasbourg. Using nonstandard analysis, they made many important discoveries [8, 9, 10, 11, 12, 32, 33] about slow-fast systems. In this manuscript we will adopt the GSPT viewpoint.

### 1.1.1 The critical manifold and the slow flow

Solutions of a slow-fast system frequently exhibit slow and fast epochs characterized by the speed at which the solution advances. As  $\varepsilon$  tends 0, the trajectories of (1) converge during fast epochs to solutions of the *fast subsystem* or *layer equations*

$$\begin{cases} \dot{x}' &= f(x, y, \lambda, 0), \\ \dot{y}' &= 0, \end{cases} \quad (3)$$

which is a family of dynamical systems for the fast variables  $x$  of the initial problem, parametrised by the slow variables whose dynamics have been “frozen” in this singular limit. During slow epochs, on the other hand, trajectories of (2) converge to solutions of

$$\begin{cases} 0 &= f(x, y, \lambda, 0), \\ \dot{y} &= g(x, y, \lambda, 0), \end{cases} \quad (4)$$

which is a *Differential-Algebraic Equation (DAE)* called the *slow flow* or *reduced system*. One goal of GSPT is to use the fast and slow subsystems, (3) and (4), to understand the dynamics of the full system (1) or (2) for  $0 < \varepsilon \ll 1$ . The algebraic equation in (4) defines the *critical manifold*

$$S := \{(x, y) \in \mathbb{R}^m \times \mathbb{R}^n \mid f(x, y, \lambda, 0) = 0\}.$$

We remark that  $S$  may have singularities [90], but we assume here that this does not happen so that  $S$  is a smooth manifold. The points of  $S$  are equilibrium points for the layer equations (3).

Fenichel theory [52] guarantees the persistence of  $S$  (or a compact subset  $M \subset S$ ) as a slow manifold of (1) or (2) for  $\varepsilon > 0$  small enough if  $S$  (or  $M$ ) is *normally hyperbolic*. The notion of normal hyperbolicity is defined for invariant manifolds more generally, effectively stating that the attraction to and/or repulsion from the manifold is stronger than the dynamics on the manifold itself; see [49, 50, 51, 72] for the exact definition. Normal hyperbolicity is often difficult to verify when there is only a single time scale. However, in our slow-fast setting,  $S$  consists entirely of equilibria and the requirement of normal hyperbolicity of  $M \subset S$  is satisfied as soon as all  $p \in M$  are hyperbolic equilibria of the layer equations, that is, the Jacobian  $(D_x f)(p, \lambda, 0)$  has no eigenvalues with zero real part. We call a normally hyperbolic subset  $M \subset S$  *attracting* if all eigenvalues of  $(D_x f)(p, \lambda, 0)$  have negative real parts for  $p \in M$ ; similarly  $M$  is called *repelling* if all eigenvalues have positive real parts. If  $M$  is normally hyperbolic and neither attracting nor repelling we say it is of *saddle type*.

Hyperbolicity of the layer equations fails at points on  $S$  where its projection onto the space of slow variables is singular. Generically, such points are folds in the sense of singularity theory [2]. At a fold point  $p_*$ , we have  $f(p_*, \lambda, 0) = 0$  and  $(D_x f)(p_*, \lambda, 0)$  has rank  $m - 1$  with left and right null vectors  $w$  and  $v$ , such that  $w \cdot [(D_{xx}^2 f)(p_*, \lambda, 0)(v, v)] \neq 0$  and  $w \cdot [(D_y f)(p_*, \lambda, 0)] \neq 0$ . These inequalities state that the tangencies of the critical manifold to the affine spaces of fast variables are similar to a quadratic function. Singularity theory makes the stronger statement that there are local coordinates in which the function  $f$  becomes  $y_1 = x_1^2$  [2]. The set of fold points forms a submanifold of codimension one in the  $n$ -dimensional critical manifold  $S$ . In particular, when  $m = 1$  and  $n = 2$ , the fold points form smooth curves that separate attracting and repelling sheets of the two-dimensional critical manifold  $S$ . Here we do not consider more degenerate singular points of the projection of  $S$  onto the space of slow variables.

Away from fold points the implicit function theorem implies that  $S$  is locally the graph of a function  $h(y) = x$ . Then the reduced system (4) can be expressed as

$$\dot{y} = g(h(y), y, \lambda, 0). \quad (5)$$

We can also keep the DAE structure and write (4) as the restriction to  $S$  of the vector field

$$\begin{cases} \dot{x} &= \pm (D_x f)^{-1} (D_y f) g, \\ \dot{y} &= g, \end{cases} \quad (6)$$

on  $\mathbb{R}^m \times \mathbb{R}^n$  by observing that  $f = 0$  and  $\dot{y} = g$  imply  $\dot{x} = \pm (D_x f)^{-1} (D_y f) g$ . The vector field (6) blows up when  $f$  is singular. It can be *desingularized* by scaling time by  $\pm \det(D_x f)$ , where we choose the sign so that the orientation of trajectories remains unchanged on the attracting sheets of  $S$ . This desingularized reduced system (DRS) plays a prominent role in much of the analysis we present here. If  $S$  is normally hyperbolic, not only  $S$ , but also the slow flow on  $S$  persists for  $\varepsilon > 0$ ; this is made precise in the following fundamental theorem.

**Theorem 1.1.1 (Fenichel's Theorem [52])** *Suppose  $M = M_0$  is a compact normally hyperbolic submanifold (possibly with boundary) of the critical manifold  $S$  of (2) and that  $f, g \in C^r$ ,  $r < \infty$ . Then for  $\varepsilon > 0$  sufficiently small the following holds:*

- (F1) *There exists a locally invariant manifold  $M_\varepsilon$  diffeomorphic to  $M_0$ . Local invariance means that  $M_\varepsilon$  can have boundaries through which trajectories enter or leave.*
- (F2)  *$M_\varepsilon$  has a Hausdorff distance of  $O(\varepsilon)$  from  $M_0$ .*
- (F3) *The flow on  $M_\varepsilon$  converges to the slow flow as  $\varepsilon$  tends to 0.*
- (F4)  *$M_\varepsilon$  is  $C^r$ -smooth.*
- (F5)  *$M_\varepsilon$  is normally hyperbolic and has the same stability properties with respect to the fast variables as  $M_0$  (attracting, repelling or saddle type).*
- (F6)  *$M_\varepsilon$  is usually not unique. In regions that remain at a fixed distance from the boundary of  $M_\varepsilon$ , all manifolds satisfying (F1)–(F5) lie at a Hausdorff distance  $O(e^{-K/\varepsilon})$  from each other for some  $K > 0$  with  $K = O(1)$ .*

The normally hyperbolic manifold  $M_0$  has associated local stable and unstable manifolds

$$W_{\text{loc}}^s(M_0) = \bigcup_{p \in M_0} W_{\text{loc}}^s(p), \quad \text{and} \quad W_{\text{loc}}^u(M_0) = \bigcup_{p \in M_0} W_{\text{loc}}^u(p),$$

where  $W_{\text{loc}}^s(p)$  and  $W_{\text{loc}}^u(p)$  are the local stable and unstable manifolds of  $p$  as a hyperbolic equilibrium of the layer equations, respectively. These manifolds also persist for  $\varepsilon > 0$  sufficiently small: there exist local stable and unstable manifolds  $W_{\text{loc}}^s(M_\varepsilon)$  and  $W_{\text{loc}}^u(M_\varepsilon)$ , respectively, for which conclusions (F1)–(F6) hold if we replace  $M_\varepsilon$  and  $M_0$  by  $W_{\text{loc}}^s(M_\varepsilon)$  and  $W_{\text{loc}}^s(M_0)$  (or similarly by  $W_{\text{loc}}^u(M_\varepsilon)$  and  $W_{\text{loc}}^u(M_0)$ ).

We call  $M_\varepsilon$  a *Fenichel manifold*. Fenichel manifolds are a subclass of *slow manifolds*, invariant manifolds on which the vector field has speed that tends to 0 on the fast time scale as  $\varepsilon \rightarrow 0$ . We use the convention that objects in the singular limit have subscript 0, whereas the associated perturbed objects have subscripts  $\varepsilon$ . Geometrically, the stable manifold  $W_{\text{loc}}^s(M_\varepsilon)$  of a Fenichel manifold  $M_\varepsilon$  consists of points whose trajectories approach  $M_\varepsilon$  in forward time; similarly,  $W_{\text{loc}}^u(M_\varepsilon)$  consists of points whose trajectories approach  $M_\varepsilon$  in backward time.

#### 1.1.1.1 The critical manifold and the slow flow in the Van der Pol equation

We now illustrate these general concepts of GSPT with an example. One of the simplest systems in which the concepts are manifest, and historically perhaps also the first, is the Van der Pol equation [152, 153, 154] with constant forcing  $\lambda \in \mathbb{R}$  given by

$$\begin{cases} \varepsilon \dot{x} &= y - \frac{1}{3}x^3 + x, \\ \dot{y} &= \lambda - x. \end{cases} \quad (7)$$

This slow-fast system has only one fast and one slow variable, but it already exhibits complicated dynamics that were truly surprising when they were first discovered [33]. By setting  $\varepsilon = 0$  in (7), we obtain the reduced system with an algebraic equation that defines the critical manifold of (7) as the cubic curve

$$S = \{(x, y) \in \mathbb{R}^2 \mid y = \frac{1}{3}x^3 - x =: c(x)\}. \quad (8)$$



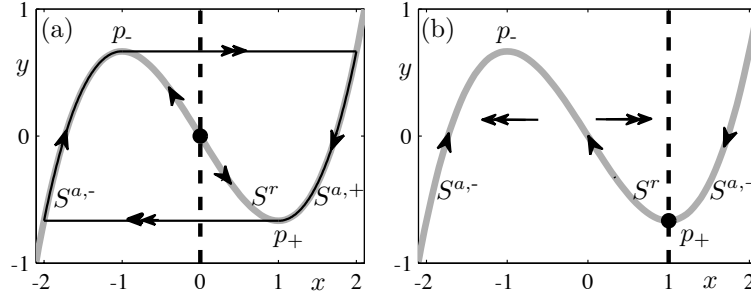


Figure 1: Phase portraits of the Van der Pol equation (7) for  $\lambda = 0$  (a) and for  $\lambda = 1$  (b). Shown are the critical manifold  $S$  (grey solid curve) and the  $y$ -nullcline (dashed line); double arrows indicate the direction of the fast flow and single arrows that of the slow flow. Panel (a) shows a candidate for a relaxation oscillation (black) surrounding an unstable equilibrium. Panel (b) is the moment of the singular Hopf bifurcation with a folded singularity at the local minimum  $p_+$ .

It is normally hyperbolic away from the local maximum and minimum  $p_{\pm} = (\pm 1, \mp \frac{2}{3})$  of the cubic, where  $S$  has a fold with respect to the fast variable  $x$ . At  $p_{\pm}$  normal hyperbolicity fails, since  $\frac{\partial}{\partial x} f(x, y, \lambda, 0) = 1 - x^2$  is zero at  $p_{\pm}$ . Hence,  $p_{\pm}$  are the fold points and they naturally decompose the critical manifold into three branches,

$$S = S^{a,-} \cup \{p_-\} \cup S^r \cup \{p_+\} \cup S^{a,+},$$

where  $S^{a,-} := S \cap \{x < -1\}$ ,  $S^{a,+} := S \cap \{x > 1\}$  and  $S^r = S \cap \{-1 < x < 1\}$ . From the sign of  $\frac{\partial}{\partial x} f(x, y, \lambda, 0)$  we conclude that the two branches  $S^{a,-}$  and  $S^{a,+}$  are attracting, and the branch  $S^r$  is repelling. The critical manifold  $S$  is shown as the grey cubic curve in Fig. 1; note that  $S$  and its attracting/repelling nature does not depend on  $\lambda$ , so it is the same both in panel (a), where  $\lambda = 0$ , and panel (b), where  $\lambda = 1$ . The dynamics of any point not on  $S$  is entirely controlled by the direction of the fast variable  $x$ , which is indicated in Fig. 1 by the horizontal double arrows; observe that the middle branch of  $S$  is repelling and the two unbounded branches are attracting.

To obtain the slow flow (5) on  $S$  in the Van der Pol equation (7) it is not actually necessary to solve the cubic equation  $y = c(x)$  for  $x$  on  $S^{a,-}$ ,  $S^r$  and  $S^{a,+}$ . It is more convenient to write the slow (reduced) flow in terms of the fast variable  $x$ . To this end, we differentiate  $f(x, y, \lambda, 0) = y - c(x) = 0$  with respect to  $\tau$  and obtain

$$\dot{y} = \dot{x} x^2 - \dot{x} = \dot{x} (x^2 - 1).$$

Combining this result with the equation for  $\dot{y}$  we get:

$$(x^2 - 1) \dot{x} = \lambda - x \quad \text{or} \quad \dot{x} = \frac{\lambda - x}{x^2 - 1}. \quad (9)$$

The direction of the slow flow on  $S$  is indicated in Fig. 1 by the arrows on the grey curve. The slow flow does depend on  $\lambda$ , because the direction of the flow is partly determined by the location of the equilibrium at  $x = \lambda$  on  $S$ . The slow flow is well defined on  $S^{a,-}$ ,  $S^r$  and  $S^{a,+}$ , but not at  $x = \pm 1$  (as long as  $\lambda \neq \pm 1$ ). We can desingularize the slow flow near  $x = \pm 1$  by rescaling time with the factor  $(x^2 - 1)$ . This gives the equation  $\dot{x} = \lambda - x$  of the *desingularized reduced flow*. Note that this time rescaling reverses the direction of time on the repelling branch  $S^r$ , so care must be taken when relating the phase portrait of the desingularized system to the phase portrait of the slow flow.

Let us now focus specifically on the case for  $\lambda = 0$ , shown in Fig. 1(a), because it is representative for the range  $|\lambda| < 1$ . The  $y$ -nullcline of (7), defined by  $\dot{y} = 0$ , is shown as the dashed black vertical line (the  $x$ -nullcline is  $S$ ) and the origin is the only equilibrium, which is a source for this value of  $\lambda$ . The closed curve is a singular orbit composed of two fast trajectories starting at the two fold points  $p_{\pm}$  concatenated with segments of  $S$ . Such continuous concatenations of trajectories of the layer equations and the slow flow are called *candidates* [9, 10]. The singular orbit follows the slow flow on  $S$  to a fold point, then it *jumps*, that is, it makes a transition to a fast trajectory segment that



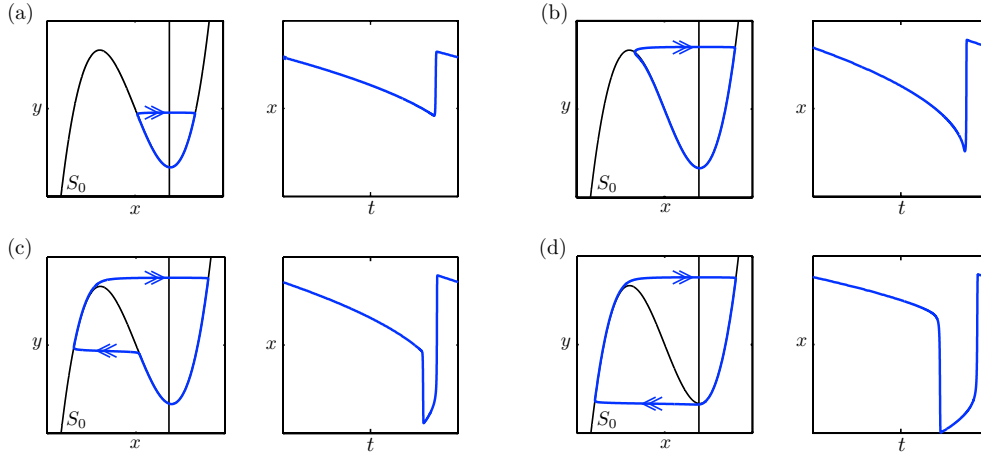


Figure 2: Canard explosion at the lower fold in the van der Pol system: the slow and the fast dynamics must be as shown and the slow nullcline (shown in black), must cross the fold transversely. Four cycles are presented (in blue): headless canard in panel (a), maximal canard in panel (b), canard with head in panel (c) and relaxation oscillation in panel (d). In each panel, the left plot corresponds to a phase plane representation of the cycle together with the fast cubic nullcline  $S_0$  and the slow linear nullcline (both in black); the right panel shows the time series of the  $x$  variable during the cycle.

flows to another branch of  $S$ . The same mechanism returns the singular orbit to the initial branch of  $S$ . It can be shown [91, 110] that the singular orbit perturbs for  $\varepsilon > 0$  to a periodic orbit of the Van der Pol equation that lies  $O(\varepsilon)$  close to this candidate. Van der Pol introduced the term *relaxation oscillation* to describe periodic orbits that alternate between epochs of slow and fast motion.

### 1.1.2 The canard phenomenon

#### 1.1.2.1 The classical canard explosion

When  $\lambda = 1$  in system (7), the DRS is such that the slow flow goes continuously through the right fold point of  $S_0$  from the attracting side to the repelling one: this is a *singular canard*; see Fig. 1 (b). For this particular parameter value, the fold point is then called a *canard point*. When the small parameter  $\varepsilon$  is perturbed away from 0, this behaviour persists and one obtains limit cycles that follow the repelling branch of  $S_0$  before jumping towards one of its attracting branches: these are *canard cycles*. For a general planar slow-fast systems

$$\dot{x}' = f(x, y) \quad (10)$$

$$\dot{y}' = \varepsilon g(x, y, \lambda), \quad (11)$$

where  $0 < \varepsilon \ll 1$  is again the small parameter measuring the separation of time scales, and  $\lambda \in \mathbb{R}$  is a parameter, the classical canard phenomenon can be described as follows. For  $\varepsilon = 0$ , these systems have a critical manifold  $S_0 = \{f(x, y) = 0\}$ . This manifold is assumed to be S-shaped curve with two non-degenerate quadratic fold points  $(x_m, y_m)$  and  $(x_M, y_M)$ , where  $f(x_i, y_i) = 0$  and  $\partial f / \partial x(x_i, y_i) = 0$  for  $i = m, M$ . In addition, we assume that for a locally unique value,  $\lambda_0$ , of the parameter  $\lambda$ ,  $g(x_m, y_m, \lambda_0) = 0$  and  $\frac{\partial g}{\partial \lambda}(x_m, y_m, \lambda_0) \neq 0$ . Hence, the slow nullcline transversely intersects  $S_0$  at one of the fold points, here the local minimum  $(x_m, y_m)$ , and the slow nullcline passes through this fold point with non-zero speed as  $\lambda$  changes through  $\lambda_0$ . Under these conditions, system (10)–(11) exhibits a standard *canard explosion* [12, 15, 41, 44, 91]. We illustrate these canard cycles in Fig. 2 with the Van der Pol example (i.e. with  $f(x, y) = y - (x^3/3 - x)$  and  $g(x, y, \lambda) = \lambda - x$ ). There is a Hopf bifurcation —typically referred to as a *singular Hopf bifurcation* [61, 62]— when the slow nullcline crosses any of the fold points of  $S_0$ , that is, at  $\lambda = \lambda_H = \pm 1$ . In Fig. 2(a), a limit cycle canard known as a headless canard (or duck), is shown. It has long segments near the attracting slow manifold (near the right branch of  $S_0$ ) and the repelling slow manifold (near the middle

branch of  $S_0$ ) in alternation and a fast jump from the latter back to the former to complete the cycle. Fig. 2(b) illustrates the maximal headless canard, which occurs for the unique parameter value,  $\lambda_c = \lambda_0 - (1/8)\varepsilon - (3/32)\varepsilon^2 + O(\varepsilon^3)$ , at which the attracting and repelling slow manifolds coincide. Then, for  $\lambda$  on the other side of  $\lambda_c$  the limit cycle canard jumps from the repelling (middle) branch to the left attracting slow manifold, forming a canard (duck) with a head, as shown in Fig. 2(c). Finally, for values of  $\lambda$  at the extreme of the canard explosion interval, the periodic solution is a full-blown relaxation oscillation, see Fig. 2(d).

The branch of limit cycles corresponding to the canard regime in the associated bifurcation diagram is almost vertical, this is because the entire explosive transition occurs within an exponentially-small range of the parameter, the canard cycles in Van der Pol type systems are said to be “short-lived”; see already Fig. 10 (b). Loosely speaking, the reason for this very brutal transition in terms of parameter variation is due to the fact that the flow near the repelling branch  $S^r$  of  $S_0$  is exponentially expanding away from  $S^r$ , therefore for canards to exist they have to be exponentially close to a repelling slow manifold, coming from an attracting one. This means that the associated parameter value has to be exponentially close to the unique value for which two such manifolds coincide, which results in a “connection” corresponding to the maximal canard. We will therefore take the following definition: A *maximal canard* is a connection between an attracting slow manifold and a repelling slow manifold. The term “canard explosion” was introduced by M. Brøns in [15].

We observe that even a standard canard explosion in slow-fast systems with one slow variable and one fast variable need not always be monotonic in the regular parameter ( $\lambda$  in the context of this section), see e.g. [91]. In other words, for some systems, the sequence of parameter values of  $\lambda$  corresponding to the canards in the canard explosion is a non-monotone sequence, within the exponentially-small interval. A very simple example of this is, for some parameter values, the FitzHugh-Nagumo system, which we will study in Chapter 2. This feature may result in the presence of turning points as well the coexistence of canard cycles for the same value of  $\lambda$ , but it does not alter the fundamental features of canard explosion, like the closeness to singular cycles and the exponentially-narrow width of the parameter interval. Due to this complication one usually does not think of a branch of canard cycles as parametrized by  $\lambda$  but rather as a curve parametrized by  $\lambda$  and another quantity characterizing the solution, which could be amplitude, often used in the context of Hopf bifurcations,  $L_2$  norm, the height of the corresponding singular canard [91], etc. The choice often made in the case of canards, partly imposed by the continuation program AUTO [38], is to use  $L_2$  norm; see Section 1.2. Keeping in mind this non-monotonicity, we will describe the evolution of canard solutions referring as a function of their position on the branch rather the corresponding value of the parameter, which does not need to be unique.

### 1.1.2.2 Folded singularities in systems with one fast and two slow variables

A canard explosion for a planar system happens in an exponentially-small parameter interval. However, as soon as there is more than one slow variable, canard orbits can exist for  $O(1)$  ranges of a parameter. To illustrate this, we consider (1) for the special case  $m = 1$  and  $n = 2$ , and write it as

$$\begin{cases} \varepsilon \dot{x} &= f(x, y, z, \lambda, \varepsilon), \\ \dot{y} &= g_1(x, y, z, \lambda, \varepsilon), \\ \dot{z} &= g_2(x, y, z, \lambda, \varepsilon). \end{cases} \quad (12)$$

We assume that the critical manifold  $S = \{f = 0\}$  of (12) has an attracting sheet  $S^a$  and a repelling sheet  $S^r$  that meet at a fold curve  $F$  as is shown in Fig. 3. We also assume that the fold points  $p_* \in F$  on  $S$  are generic in the sense of singularity theory, that is,

$$\begin{aligned} f(p_*, \lambda, 0) &= 0, & \frac{\partial f}{\partial x}(p_*, \lambda, 0) &= 0, \\ \frac{\partial^2 f}{\partial x^2}(p_*, \lambda, 0) &\neq 0, & D_{(y,z)} f(p_*, \lambda, 0) &\text{ has full rank one.} \end{aligned}$$

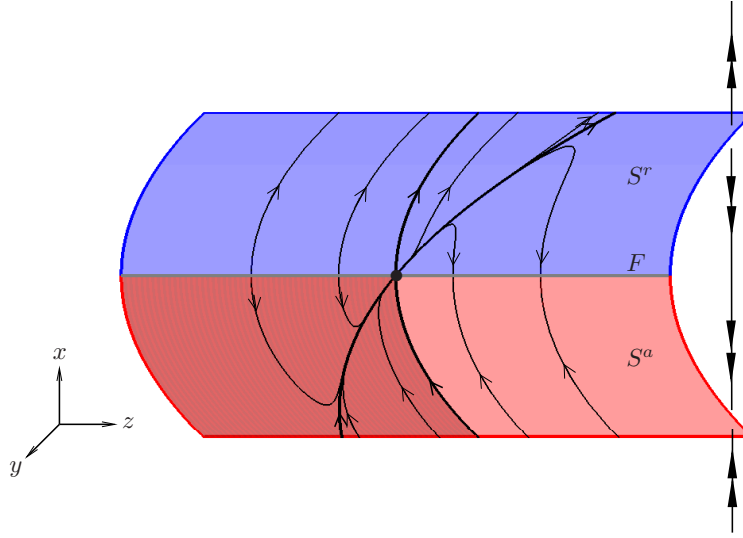


Figure 3: The critical manifold  $S$  with attracting sheet  $S^a$  (red) and repelling sheet  $S^r$  (blue) that meet at a fold curve  $F$  (grey). The fast flow transverse to  $S$  is indicated by double (large) arrows and the slow flow on  $S$  near a folded node by single (small) arrows. The darker shaded region of  $S^a$  is the funnel, consisting of all points that pass through the folded node.

The slow flow is not defined on the fold curve before desingularization. At most fold points, trajectories approach or depart from both the attracting and repelling sheets of  $S$ . In generic systems, there may be isolated points, called *folded singularities*, where the trajectories of the slow flow switch from incoming to outgoing. From that perspective, canard points are folded singularities in the context of planar slow-fast systems. Folded singularities are equilibrium points of the DRS, which can be expressed as

$$\begin{cases} \dot{x} = \left(\frac{\partial f}{\partial y}\right) g_1 + \left(\frac{\partial f}{\partial z}\right) g_2, \\ \dot{y} = -\left(\frac{\partial f}{\partial x}\right) g_1, \\ \dot{z} = -\left(\frac{\partial f}{\partial x}\right) g_2, \end{cases} \quad (13)$$

restricted to  $S$ . A fold point  $p_* \in F$  is a folded singularity if  $\dot{x} = 0$  in (13), or

$$g_1(p_*, \lambda, 0) \frac{\partial f}{\partial y}(p_*, \lambda, 0) + g_2(p_*, \lambda, 0) \frac{\partial f}{\partial z}(p_*, \lambda, 0) = 0$$

in terms of (12). Figure 3 shows an example of the slow flow on  $S$  and the thick dot on  $F$  is the folded singularity at which  $F$  changes from attracting to repelling (with respect to the slow flow).

There are different possibilities for the stability of  $p_*$  in (13). Let  $\sigma_1$  and  $\sigma_2$  denote the eigenvalues of the Jacobian matrix of (13) restricted to  $S$  and evaluated at a folded singularity  $p_*$ . We call  $p_*$  a

$$\begin{cases} \text{folded saddle,} & \text{if } \sigma_1 \sigma_2 < 0, \quad \sigma_{1,2} \in \mathbb{R}, \\ \text{folded node,} & \text{if } \sigma_1 \sigma_2 > 0, \quad \sigma_{1,2} \in \mathbb{R}, \\ \text{folded focus,} & \text{if } \sigma_1 \sigma_2 > 0, \quad \text{Im}(\sigma_{1,2}) \neq 0. \end{cases}$$

Note that the phase portrait for the slow flow in Fig. 3 is obtained by reversing the direction of the flow on  $S^r$  where  $\frac{\partial f}{\partial x} > 0$ , that is, by reversing the arrows in the phase portrait of the desingularized slow flow where  $x > 0$ . It is an important observation that the trajectories of the slow flow that lie along the eigendirections of the folded node (or of the folded saddle) connect the two sheets of the critical manifold through the folded singularity in finite (slow) time; such a trajectory is called a *singular canard*. Note that there are no singular canards for the case of a folded focus. For the case of a folded node one generically has an inequality of the form  $|\sigma_1| > |\sigma_2|$ , and we write  $|\sigma_s| > |\sigma_w|$ , replacing the numeric labels with  $s$  and  $w$  to emphasize the strong and weak eigendirections. Notice

further for the case of the folded node in Fig. 3 that the strong singular canard  $\tilde{\gamma}_s$  and the fold curve  $F$  bound a full (shaded) sector of trajectories that cross from  $S^a$  to  $S^r$  by passing through the folded node. This sector and the corresponding region for the full system (12) are called the *funnel* of the folded node.

Singular canards act as candidates of maximal canards of the full system for  $\varepsilon > 0$ . This is described in the next theorem [8, 11, 18, 144, 156].

**Theorem 1.1.2 (Canards in  $\mathbb{R}^3$ )** *For the slow-fast system (12) with  $\varepsilon > 0$  sufficiently small the following holds:*

- (C1) *There are no maximal canards generated by a folded focus.*
- (C2) *For a folded saddle the two singular canards  $\tilde{\gamma}_{1,2}$  perturb to maximal canards  $\gamma_{1,2}$ .*
- (C3.1) *For a folded node let  $\mu := \sigma_w/\sigma_s < 1$ . The singular canard  $\tilde{\gamma}_s$  (“the strong canard”) always perturbs to a maximal canard  $\gamma_s$ . If  $\mu^{-1} \notin \mathbb{N}$  then the singular canard  $\tilde{\gamma}_w$  (“the weak canard”) also perturbs to a maximal canard  $\gamma_w$ . We call  $\gamma_s$  and  $\gamma_w$  primary canards.*
- (C3.2) *For a folded node suppose  $k > 0$  is an integer such that  $2k + 1 < \mu^{-1} < 2k + 3$  and  $\mu^{-1} \neq 2(k + 1)$ . Then, in addition to  $\gamma_{s,w}$ , there are  $k$  other maximal canards, which we call secondary canards.*
- (C3.3) *The primary weak canard of a folded node undergoes a transcritical bifurcation for odd  $\mu^{-1} \in \mathbb{N}$  and a pitchfork bifurcation for even  $\mu^{-1} \in \mathbb{N}$ .*

The proof of this theorem is based upon analysis of a canonical (normal) form of a slow-fast system near a folded singularity. Recall that a maximal canard corresponds to a (transverse) intersection of the slow manifolds  $S_\varepsilon^a$  and  $S_\varepsilon^r$  near a folded singularity. After a rescaling of coordinates (a ‘blow-up’), the canonical system becomes a regular perturbation problem and the variational equation along the ‘blown-up’ singular canards ( $\varepsilon = 0$  problem) becomes a classical *Weber equation* that also arises in mathematical physics. [117]. Properties of the Weber equation imply a transverse intersection of  $S_\varepsilon^a$  and  $S_\varepsilon^r$  for  $\mu^{-1} \notin \mathbb{N}$  and hence existence of maximal canards (parts (C2)–(C3.1)) for sufficiently small perturbations  $0 < \varepsilon \ll 1$ . The proof of parts (C3.2)–(C3.3) is more involved and is based upon an extension of *Melnikov theory* [155] to show the bifurcation of secondary canards from the primary weak canard for  $\mu^{-1} \in \mathbb{N}$ .

## 1.2 NUMERICAL CONTINUATION METHODS

After introducing the main mathematical objects that we are going to study in the remaining part of this manuscript, we now present the main numerical tool that we will use to study them, namely, *numerical continuation* methods. The term numerical continuation refers to a family of algorithms — denoted under the very general term of *path-following methods*, see [1] — used to compute branches of solutions of nonlinear equations of the form

$$F(x) = 0, F: \mathbb{R}^{n+1} \rightarrow \mathbb{R}^n. \quad (14)$$

Equation (14) is underdetermined as there is one more unknown than equations. Therefore, away from singularities one expects the solution set of (14) to be a one-dimensional manifold, which we will refer to as a *solution branch*, embedded in  $(n + 1)$ -dimensional space. A number of problems can be put in the form of (14); one important example comes from the discretisation of parametrized families of differential equations of the form

$$\dot{x} = F(x, \lambda), \quad (15)$$

where  $x \in \mathbb{R}^n$  correspond to the state variables and  $\lambda \in \mathbb{R}$  is a given control parameter of the system. In this framework, various solutions to (15) can be computed by solving a nonlinear equation of the form  $\tilde{F}(x, \lambda) = 0$ , where  $\tilde{F}$  can be equal to  $F$  or also involve additional terms. In particular, when looking for  $\lambda$ -dependent families of stationary solutions of (15), one needs to solve exactly

$F(x, \lambda) = 0$ . Parametrized families of periodic solutions of (15) and, more generally, parametrized families of orbit segments solution of (15), can also be computed, together with suitable boundary and integral conditions, within the general framework of (14).

The main theoretical tool on which numerical continuation relies is the Implicit Function Theorem (IFT), applied to a suitable parametrization of the solution curve that allows to compute it past fold points, namely, the parametrization by the arclength of the solution curve. This idea is one of the cornerstones of numerical continuation. Indeed, by parametrizing the solution curve by the projection of the arclength onto the tangent curve to the solution branch at a given point, one can compute this curve past fold points and, hence, in the dynamical context, trace unstable as well as stable branches of solutions (stationary or periodic). The way the solution is actually computed is through a *predictor-corrector* procedure. The predictor is taken along the tangent to the curve already computed at the last computed point  $(x_0, \lambda_0)$ , at a fixed distance from it. Then, the corrector is obtained by applying a Newton type iteration, perpendicularly to the tangent to the curve at the last computed point, to find the next point on the curve. This amounts to append to equation (14) the *pseudo-arclength equation*

$$(\lambda - \lambda_0)\dot{\lambda}_0 + (x - x_0)\dot{x}_0 - \delta s = 0, \quad (16)$$

where  $s$  is the arclength of the curve, measured along the tangent space, and  $\delta s$  is the continuation step size. Equation (14) together with equation (16) form a square system of algebraic equations and one can compute a unique solution of this system. In the case of periodic solutions, one needs to add to this procedure the discretisation of the periodic orbit. This is usually done by means of *orthogonal collocation*, where the orbit is approximated by piecewise-polynomials defined inside mesh intervals. They interpolate the original vector field at certain well-chosen points (collocation points) in each of these mesh intervals, and solve exactly the system at the boundary points of the mesh intervals. Note that the time is rescaled so that the actual period  $T$  of the solution becomes a parameter that can be solved for. Finally, the system is closed by adding to the algebraic equation (14) and the pseudo-arclength equation (16) an integral condition that selects uniquely the periodic solution to be computed by fixing its phase. For more informations about the implementation details of pseudo-arclength continuation schemes for stationary, periodic and general boundary-value problems, we refer the reader to classical articles and textbooks such as [1, 34, 36, 37, 127, 139], together with references therein.

Throughout the present manuscript, we will make use of numerical continuation to understand the bifurcation structure of slow-fast systems, in particular, the bifurcation structure of fast subsystems when one (or two) slow variables are considered as parameters; see Chapter 4 and 5. However, we also wish to get numerical access to canard solutions, which are defined as transversal intersections between attracting and repelling two-dimensional slow manifolds, in the context of minimal systems possessing a folded singularity. The main underlying idea of our approach is that one can compute (a finite part of) a two-dimensional invariant manifold of a system of ordinary differential equations as a collection of orbit segments by numerical continuation of a one-parameter family of two-point Boundary-Value Problems (BVPs). This approach can be applied in a wide variety of contexts [88]. In Chapter 3, we will explain how to use this strategy to compute attracting and repelling slow manifolds associated with a slow-fast system of the form (12) with a folded node, obtain good numerical approximation of their associated canard solutions, and then compute branches of such canards in parameter space. This is the main numerical contribution presented in this manuscript.



Elements of the material presented in this chapter have been published in [23, 30, 100]. Two contributions are exposed, both related to canard-explosive planar systems. In the first section, we apply standard numerical continuation method to suitably-chosen slow-fast Liénard systems possessing “more limit cycles than expected” due to the time scale separation. We give numerical evidence that continuation is an efficient tool to find these additional cycles and estimate the range in  $\varepsilon$  for which they exist as well as mechanisms for their disappearance in parameter space. In the second section, we present different results, related to the inflection lines of the flow in such planar slow-fast systems, in the canard regime. We first analyse the geometry of these inflection lines by means of singularity theory. We then use their  $\varepsilon$ -dependence to propose an upper bound in  $\varepsilon$  for canard cycles to exist and, finally, we investigate how inflection lines approximate the excitability threshold in both integrator and resonator neuron models.

## 2.1 NUMERICAL CONTINUATION TECHNIQUES FOR PLANAR SLOW-FAST SYSTEMS

Continuation techniques have been known to successfully describe bifurcation diagrams appearing in slow-fast systems with more than one slow variable (see. [27] and Chapter 3). In this section we investigate the usefulness of numerical continuation techniques dealing with some solved and some open problems in the study of planar slow-fast systems. More precisely, we verify known theoretical results, thereby showing the reliability of this numerical tool, on the appearance of multiple limit cycles of relaxation-oscillation type. More precisely, we analyse numerically the number of limit cycles in some families of planar slow-fast systems, mostly of Liénard type, using numerical continuation. We start by recalling the main facts concerning the advantage one gains in using numerical continuation schemes for slow-fast dynamical systems.

### 2.1.1 Numerical continuation as a well-suited tool for slow-fast systems

Numerical continuation is very much adapted to multiple time scale problems. The main advantages of using numerical continuation in order to address the question of trajectories (in particular, cycles) corresponding to solutions of slow-fast planar systems are of two kinds.

First, orbits are approximated using orthogonal collocation, which is well-suited for problems with multiple time scales in terms of error handling. Indeed, the error is spread along all the orbit instead of being concentrated at one end point as is the case with shooting techniques. To this extent, collocation can be seen as an “extreme” form of multiple shooting since, to be able to compute reliably trajectories containing canard segments, one usually needs hundreds of mesh intervals. Furthermore, the time scale separation parameter  $\varepsilon$  has the effect that trajectories near repelling slow manifolds diverge exponentially from one another. As a consequence, when advancing in time with a numerical integration algorithm, one needs a very high precision in the initial conditions to be able to track a canard segment over a long portion of repelling slow manifold. This numerical difficulty is made worse by the fact that canard cycles are “short-lived” in the sense that they exist in parameter ranges that are exponentially small in  $\varepsilon$ . This clearly adds a very strong sensitivity in the parameter precision to the already strong sensitivity to initial conditions that one faces when trying to compute such orbit segments by integration. On the other hand, this extreme sensitivity and strong repulsion in the normal direction to the orbit is much better handled by the boundary-value solvers used in continuation packages such as AUTO [38], which is the software that we will use for all the examples

treated in this work. This advantage of continuation over integration for canard computations has been previously investigated in [68]; it has also been studied and proven useful for the computation of canard orbits in three-dimensional systems with two slow variables [27, 28]. Of course, we do not wish to pretend here that numerical continuation is the ultimate tool to address the question of computing trajectories in slow-fast systems. Standard packages like AUTO07P also have their limitations when tackling singularly perturbed vector field, for instance, that of an accurate computation of Floquet multipliers is well-known [66, 68]. More sophisticated techniques such as *automatic differentiation* can be used to improve the treatment of these computational issues; see [60, 67] for more details. More generally, the presence of multiple time scales can introduce a plethora of convergence problems where  $\varepsilon$  gets “too small”; while quantifying the critical size of the small parameter as a function of various discretisation parameters (such as the number of mesh intervals) is still an open question, it is inevitable that all numerical methods will fail, sooner or later, as  $\varepsilon$  approaches the singular limit. For an example of error analysis and comparison between different numerical strategies to compute limit cycles in multiple time scale systems (number of iterations in the convergence of Newton’s method, condition number of the Jacobian, domains of convergence), we refer the reader to the book chapter [67] by Guckenheimer and Lamar. The methods compared are the collocation algorithm implemented in AUTO and multiple-shooting algorithms implemented by the authors. A similar comparison in the context of the questions which we chose to investigate is beyond the scope of this work; it is an important direction for future work. Instead, our point here is that we used a standard continuation package, without modifying a single line of code, and obtained valuable pieces of information about the number of limit cycles in planar slow-fast systems and their organisation in parameter space, not easily accessible via standard integration methods. Moreover, we do not address in general the question of the stability of these cycles and we do not investigate the occurrence of bifurcations of canard cycles other than fold bifurcations.

The second gain in using numerical continuation relies in the fact we are interested in investigating the presence of multiple limit cycles in certain families of planar systems, and we wish to understand how additional cycles appear as the timescale parameter  $\varepsilon$  decreases. It turns out that these additional cycles are associated with fold bifurcations of limit cycles in the one-parameter bifurcation diagram of the system under consideration. In this context, using a predictor-corrector scheme is very appropriate as it allows to trace a family of limit cycles born at a Hopf bifurcation as a given parameter is varied; typically, in this work we vary the parameter determining the position of the slow nullcline. We can then detect fold bifurcation points along the branch and trace out their loci as a secondary parameter is varied, in particular, the time scale parameter  $\varepsilon$ . This yields important information about the occurrence of additional cycles. In particular, we find that as  $\varepsilon$  is decreased, one fold bifurcation of cycles shifts towards the region where the Hopf bifurcation exists, allowing for multiple intersections of the branch of limit cycles with a vertical line, that is, multiple cycles to coexist in the system; see already Fig. 8. By continuing in two parameters relevant to fold bifurcations of cycles, we can detect the critical values of  $\varepsilon$  where this phenomenon starts and then ceases. In this way, we can estimate in a two-parameter plane (one parameter being  $\varepsilon$ ) the region where the system displays a given number of coexisting cycles; see already Fig. 6 (b) and Fig. 9.

### 2.1.2 Limit cycles in some slow-fast Liénard systems

Here, we will exclusively focus on planar, singularly perturbed, vector fields. More precisely, we will consider slow-fast Liénard systems, which are of the form

$$\begin{cases} \dot{x} &= y - f(x, \lambda) \\ \dot{y} &= \varepsilon g(x, \lambda) \end{cases} \quad (17)$$

where  $f$  and  $g$  are smooth  $\lambda$ -families of functions  $U \subset \mathbb{R} \rightarrow \mathbb{R}$ , and where  $\varepsilon > 0$  is the singular parameter. Liénard equations are interesting for themselves, first because planar systems can sometimes be reduced to Liénard equations (e.g. Van der Pol and FitzHugh-Nagumo type systems, and

see also [99]), and also because their study contributes to Smale's 13th problem [134] regarding "classical" Liénard systems (that is, where  $g(x, \lambda) = -x$ ).

Planar slow-fast systems can be used in applications to model situations where the dynamics behaves along two vastly different time scales. From the viewpoint of applications, one is primarily interested in stable periodic orbits and, to a large extent, one will avoid canard orbits. Under these conditions, planar slow-fast systems are easy to treat, both analytically and numerically. Analytically, a fairly complete treatment is given in [104], and numerically it is clear that if one wants to trace stable objects, a standard forward integration technique such as the Runge-Kutta scheme will suffice to capture the different behaviours of the system, that is, either globally stable stationary solutions or stable large-amplitude periodic solutions usually referred to as *relaxation oscillations* [153]. However, the analysis becomes a true challenge when the interest is extended towards treating canard orbits: not only do canard orbits contain parts that are extremely unstable with respect to variations of the initial conditions, but they themselves can change their shape drastically under the influence of small changes in the control parameter  $\lambda$ ; this dramatic change upon exponentially small parameter variation was termed "canard explosion" [15], an expression that has become customary in the slow-fast community. Besides their clear theoretical importance, the success of canard problems over the last three decades can be explained by the vast repertoire of applications where such dynamics has been encountered and proven to be of crucial relevance in the system, ranging from biological [113], physical [105], to chemical [16, 133] models. For reasons that we will now develop, standard forward integration techniques can experience important pitfalls and, hence, can be efficiently complemented by path-following methods when one wants to compute reliably parametrized families of canard orbits in the cases that we are interested in.

#### 2.1.2.1 Main goal

Restricting our attention to planar slow-fast systems of the kind (17), we focus on a specific problem, investigated in Section 2.1.2.2, which deals with the appearance of multiple canard cycles. We consider classical Liénard equations of the form

$$\begin{cases} \dot{x} &= y - f(x) \\ \dot{y} &= \varepsilon(b - x), \end{cases} \quad (18)$$

where  $b \approx 0$  and where the graph  $y = f$  is of "parabolic" type, with a minimum at the origin. It is known that for each choice of  $Y$  there exists a curve  $b = B_Y(\varepsilon)$  along which a canard orbit passes through  $(0, Y)$ . The family (18) then has at most one limit cycle (globally) when the function  $B_Y(\varepsilon)$  behaves monotonically with respect to  $Y$ . When it is not monotone, the graph  $Y \mapsto B_Y(\varepsilon)$ , for fixed  $\varepsilon$ , has a typical shape; in Section 2.1.2.2 we show how to numerically trace such graphs for specific examples where one can analytically prove the existence of 1, 2, 3 or more canard cycles. The results in that section clearly show how multiple limit cycles, proven to be present near the singular limit, disappear when  $\varepsilon$  increases. The interest in the presence of multiple limit cycles for planar systems originates in the Hilbert 16th problem, which was restated specifically for classical Liénard systems (18) by Smale in 2000 as Smale's 13th problem. This problem asks for a uniform upper bound of the number of limit cycles stated in terms of the degree of  $f(x)$ , and it was expected that the bound would be  $\lfloor \frac{n-1}{2} \rfloor$ , where  $n = \deg f$ , as conjectured in 1977 in [98]. It was only from 2007 onwards that counterexamples were produced, see [102] and [43]. Both examples deal with slow-fast systems, and the presence of multiple limit cycles is shown in the singular limit. In [102], 4 limit cycles were found in a system of degree 6, instead of the conjectured maximum 2. In that paper, an attempt is made to trace the limit cycles using forward integration techniques, with a brute force method using high precision computations. After long computations, 3 of the 4 limit cycles were numerically computed, the fourth one being unreachable. Here, we trace the limit cycles using standard continuation tools, which can then easily be reproduced and are more convincing than using an ad hoc algorithm. Our aim is not to prove that numerical continuation is the best tool to deal with this problem, for example when compared to stiff integrators and algorithms using automatic differentiation.



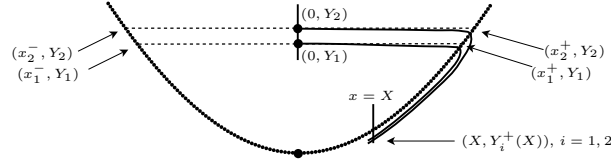


Figure 4: Backward and forward integrating two orbits through  $(0, Y_1)$  and  $(0, Y_2)$ , for  $\varepsilon > 0$  small. The points  $(x_i^\pm, Y_i)$  are  $\omega$  and  $\alpha$  limits of the orbit through  $(0, Y_i)$  for  $\varepsilon = 0$ .

However, we wish to prove, on one hand, that it is a reliable tool — a rather straightforward use of it yielding the results — and, on the other hand, that it is to be expected that these multiple cycles do not survive for reasonably large values of  $\varepsilon$ . This will be done in Section 2.1.2.5.

#### 2.1.2.2 More limit cycles than expected

The qualitative study of planar vector fields is relatively easy, besides the prediction of the number of limit cycles and their position in the plane. Two famous open problems relate to the limit cycles of planar vector fields: Hilbert 16th problem and Smale's 13th problem. We refer to [134] and [39] for the role of slow-fast systems in these problems. Our interest lies in the study of well-chosen systems that have a number of limit cycles; in other words, we will use slow-fast systems to give examples of low-degree polynomial vector fields that have many limit cycles. Theoretical results of this nature can, for example, be found in [103].

In this section, we will work with (18). We suppose that  $f$  is of parabolic type, i.e.  $f(x, \lambda) = x^2(1 + O(x))$ , and  $\frac{\partial f}{\partial x}/x$  is positive everywhere. We consider  $b \approx 0$ .

#### 2.1.2.3 The slow divergence integral

We first indicate the numerical difficulties involved in finding the limit cycles. To that end, we introduce the notion “slow divergence integral”, and present a rough outline of the proof of Theorem 2.1.1 stated below in this section, which relates isolated zeros of this slow divergence integral to isolate periodic orbits. A more detailed presentation of the proof can be found in [101].

Consider (18), and suppose we compute two orbits through  $(0, Y_1)$  and  $(0, Y_2)$  for some given  $Y > 0$ . Assume that  $Y_1 < Y_2$ . The orbits quickly move towards the right branch of the parabola near points  $(x_1^+, Y_1)$  and  $(x_2^+, Y_2)$ , after which they slide downwards along the parabola (since the slow dynamics is given by  $y' = b - x$ , which is negative for  $x > 0$  and  $b \approx 0$ ). Knowing that the singular points on the parabola are all stable, and knowing that the orbits spend an  $O(1/\varepsilon)$  amount of time along this branch, it is not surprising to find that both orbits get exponentially close to each other. More precisely, suppose the two orbits meet the section  $\{x = X\}$  (with  $X < x_1^+$ ) after some sliding downwards, and let  $(X, Y_1^+(X))$  and  $(X, Y_2^+(X))$  be the intersection points of the two orbits (see Fig. 4), then

$$Y_1^+(X) - Y_2^+(X) = \exp \left( \frac{1}{\varepsilon} \int_{x_1^+}^X \frac{\frac{\partial f}{\partial x}(s)^2}{s - b} ds + o(1) \right).$$

The integral appearing in this formula is the slow divergence integral taken between two sections  $\{x = x_1\}$  and  $\{x = X\}$  and it is strictly negative. Observe that the distance between the two orbits does not depend on  $(x_2^+, Y_2)$  up to first order. Apparently, this estimate also works when we replace  $X$  with 0, under the assumption that  $b = o(\sqrt{\varepsilon})$ . (One needs to do some work to achieve this.) We find

$$Y_1^+(0) - Y_2^+(0) = \exp \left( \frac{1}{\varepsilon} \int_{x_1^+}^0 \frac{\frac{\partial f}{\partial x}(s)^2}{s} ds + o(1) \right).$$

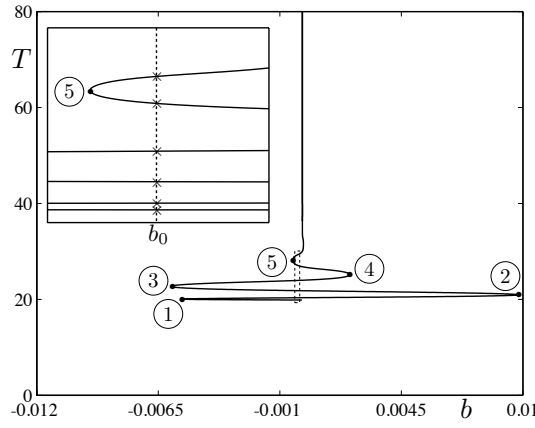


Figure 5: The canard curve of (20), for  $\varepsilon = 0.1$ . The 5 folds correspond to the 5 zeros of the slow divergence integral.

Similarly, we can track the orbits in negative time. Let  $(x_1^-, Y_1)$  and  $(x_2^-, Y_2)$  be the points of the parabola in  $\{x < 0\}$  so that  $f(x_i^-) = Y_i$ , and let  $(X, Y_i^-(X))$  be points of the orbits near the parabola, for  $X \leq 0$  small enough. Then

$$Y_1^-(0) - Y_2^-(0) = \exp \left( \frac{1}{\varepsilon} \int_{x_1^-}^0 \frac{\frac{\partial f}{\partial x}(s)^2}{s} ds + o(1) \right).$$

Both formulas work under assumption that  $b = o(\sqrt{\varepsilon})$  so write  $b = \sqrt{\varepsilon}B$  and let  $B = o(1)$ . It is known that

$$Y_1^-(0) - Y_1^+(0) = \sqrt{\varepsilon} (B + o(1))$$

(and similarly for  $Y_2^-(0) - Y_2^+(0)$ ). Therefore, we have the following situation: when integrating in positive time, orbits meet  $\{X = 0\}$  in an exponentially narrow wedge, and when integrating in negative time, the orbits meet  $\{X = 0\}$  in another exponentially narrow wedge; the distance between the two wedges is  $O(b)$ . In other words, we can easily choose  $b = b(Y_2)$  in terms of  $Y_2$  making the orbit through  $(0, Y_2)$  a periodic one. Similarly, for  $b = b(Y_1)$ , the orbit through  $(0, Y_1)$  is periodic.

If one is interested in finding multiple limit cycles, one might wonder whether along  $b = b(Y_2)$  the orbit through  $(0, Y_1)$  is also a periodic one. Heuristically, we have

$$Y_1^+ - Y_1^- = (Y_1^+ - Y_2^+) + \underbrace{(Y_2^+ - Y_2^-)}_0 + (Y_2^- - Y_1^-).$$

The difference is 0 if and only if the exponents appearing in the expressions for  $Y_1^+ - Y_2^+$  and  $Y_1^- - Y_2^-$  are equal, or, in other words, if and only if  $I(Y_1) + o(1) = 0$ , where

$$I(Y_1) = \int_{x_1^+}^{x_1^-} \frac{\frac{\partial f}{\partial x}(s)^2}{s} ds. \quad (19)$$

We recall that  $x_1^+$  and  $x_1^-$  are the two solutions of  $f(x) = Y_1$ ; in that sense the above integral is an algebraic expression depending on  $Y_1$ . Hence, it makes sense to denote it  $I(Y_1)$ . This expression is called the *slow divergence integral* for the slow-fast cycle at height  $Y_1$ . It is now heuristically clear that a sign change in  $I(Y)$  as  $Y$  varies leads to a solution of the above equation near the sign change. In other words, we have

**Theorem 2.1.1 ([42])** *Let the orbit through  $(0, Y_2)$  be periodic for  $\varepsilon > 0$  small enough. Let  $I(Y)$  be the slow divergence integral as defined above, for  $Y \in ]0, Y_2[$ . If  $I(Y)$  has  $N$  isolated and simple zeros, then the system has  $N$  additional periodic orbits, crossing the  $y$ -axis at  $y$ -coordinates close to the zeros of  $I(Y)$ .*

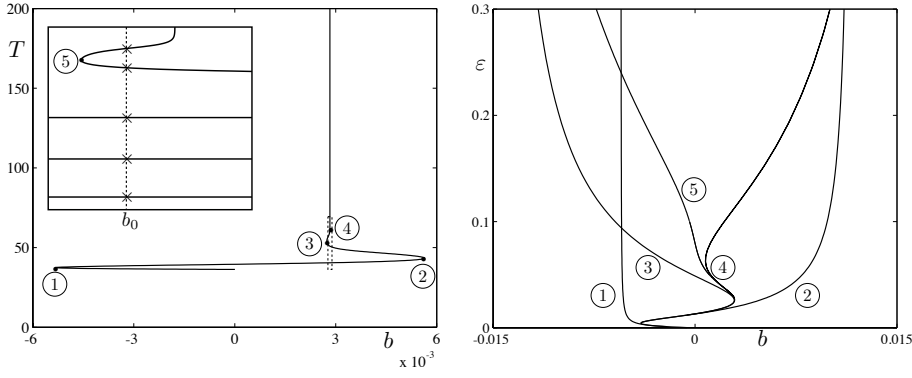


Figure 6: Left panel: The canard curve of (20), for  $\varepsilon = 0.03$ . The 5 folds correspond to the 5 zeros of the slow divergence integral. Right panel: the location of the folds in terms of  $\varepsilon$ .

Numerically, computing the periodic orbits is very difficult, since all orbits meet  $\{X = 0\}$  (either in positive or negative time) in an exponentially small wedge. To be able to distinguish whether an orbit through  $(0, Y_2)$  is periodic or not, we need a numerical precision of the order  $\min\{\exp(I_2^-/\varepsilon), \exp(I_2^+/\varepsilon)\}$ , where  $I_2^\pm$  are the one-sided slow divergence integrals at height  $Y_2$ . Even for reasonable values of  $\varepsilon$ , the required precision is often much too high for standard integration softwares.

Multiple periodic orbits can also be detected as solutions of  $b(Y_1) = b(Y_2)$ , where  $b = b(Y)$  is introduced in the previous subsection. When  $b$  is monotonous, there is only one periodic orbit. If on the other hand,  $b$  is oscillatory, we can have limit cycles at different heights  $Y$  corresponding to the same value of the parameter  $b$ . We then clearly have

**Theorem 2.1.2 ([40])** *Let  $b = b(Y)$  be the canard curve, defined for  $Y \in ]0, Y_{\max}[$ . If there is a  $b_0$  for which  $b(Y) = b_0$  has  $N$  solutions, then the system has  $N$  periodic orbits for this specific value of the parameter  $b$ .*

Note that detecting the oscillations in the canard curve is also not elementary since  $b(Y_2)$  and  $b(Y_1)$  are exponentially close to each other. We give examples in the next subsection; see already Fig. 6 for a typical canard curve  $b(Y)$ .

*Remark.* The canard curve in Theorem 2.1.2 should not be confused with a curve where the parameter  $b$  is expressed in terms of  $\varepsilon$ . In [40], the traditional curve where the control parameter is expressed in terms of  $\varepsilon$  is called a canard curve, in contrast with the curve where the control parameter is expressed in terms of the amplitude and which is called a *position curve*. Here, we focus on numerical properties of these position curves (and how they evolve for increasing values of  $\varepsilon$ ); one can find theoretical results and an explanation of the typical shape of a position curve in [40].

#### 2.1.2.4 Examples of “oscillatory” canard curves

An easy family of equations where the canard curve is oscillatory is given by

$$\begin{cases} \dot{x} &= y - (x^2 + \frac{1}{M}xH(x^2)) \\ \dot{y} &= \varepsilon(b - x). \end{cases}$$

For  $M$  large enough, the graph  $y = x^2 + \frac{1}{M}xH(x^2)$  is of parabolic type. We claim that each zero of the function  $H$  leads to a zero of the slow divergence integral. Indeed, let  $F(x) = x^2 + \frac{1}{M}xH(x^2)$ . When  $H(x_0) = 0$ , then  $F(x_0) = F(-x_0)$ , and it is an elementary exercise to verify that  $\int_{x_0}^{-x_0} \frac{F'(x)^2}{x} dx = 0$  (using symmetry properties of even and odd functions). (Note that there might be additional zeros of the slow divergence integral). In other words, when  $H(x_0) = 0$ , then  $I(Y_0) = 0$  where  $Y_0 = F(x_0)$ .

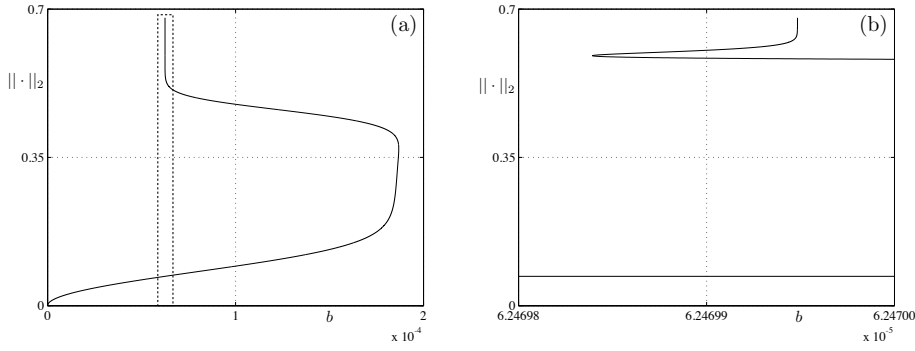


Figure 7: Three limit cycles were found using numerical continuation in the  $F^\#$ -system defined in [102] for  $\varepsilon = 0.003$ . (a) The curve  $b = b(Y)$  in terms of the AUTO  $L_2$ -norm of the solution. (b) Enlargement near the second fold bifurcation of limit cycles.

Consider now the following system

$$\begin{cases} \dot{x} = y - (0.5x^2 + 0.05 \sin(15x)x^2) \\ \dot{y} = \varepsilon(b - x), \end{cases} \quad (20)$$

and restrict the phase space to the region where the critical curve is of parabolic kind. In that region, the divergence integral has 5 simple zeros. If we fix a small value of  $\varepsilon$ , then the canard curve is shown in (20). It is clear that up to 6 limit cycles can be found. Let us now closely inspect the diagram shown on the right panel of Fig. 6, where the loci of folds in the canard curve are traced in the  $(b, \varepsilon)$ -plane, using a standard two-parameter continuation algorithm, for increasing values of  $\varepsilon$ . It is remarkable to see how these curves, which all lie in an exponentially small wedge near  $\varepsilon = 0$ , tend to behave really differently for increasing values of  $\varepsilon$ . Let us now focus on the curve (5), and choose a value of  $\varepsilon$  fixed, and let us add a vertical curve  $(b_0)$ :  $b = b_0$ . As long as the curves (4), (3), (2), (1) and  $(b_0)$  are located respectively to the right, to the left, to the right, to the left and to the right of the point on (5), the canard curve will attain a value of  $b$  nearby and to the right of the fold (5) exactly 6 times (as shown with a magnified view in the inset of the left panel of Fig. 6). It implies that the crossing of the curves (1) and (3) is not relevant, but the crossing of the curves (5) and (1) and the crossing of (5) and  $(b_0)$  are indeed relevant. Clearly, by inspecting Fig. 5, we can choose a value  $b_0$  for which there are 6 limit cycles, because the folds (5), (4), (3), (2), (1) are located alternatively to the right and to the left of  $(b_0)$ . For a slightly different value of  $\varepsilon$  however, we cannot choose  $b_0$  that way: in Fig. 6, there are still 5 folds corresponding to the five zeros of the slow divergence integral, but they are aligned in a less favorable way, allowing up to only 5 limit cycles to be present at the same time. We formulate these numerical observations in the following statement:

**NUMERICAL OBSERVATION.** *In the region where the critical curve of (20) is of parabolic shape, there can be up to 6 limit cycles in (20), for  $\varepsilon \in ]0, \varepsilon_1[ \cup ]\varepsilon_2, \varepsilon_3[$ , where  $\varepsilon_1 \approx 0.01$ ,  $\varepsilon_2 \approx 0.08$  and  $\varepsilon_3 \approx 0.25$ .*

#### 2.1.2.5 Multiple limit cycles in Liénard systems of degree 6

In Section 2.1.2.2, we have reviewed how one can analytically establish the presence of multiple limit cycles, by examining the slow divergence integral, and we have also explained how numerical continuation can be useful to actually determine the limit cycles near the singular limit  $\varepsilon = 0$ , and how the limit cycles evolve as  $\varepsilon$  is increased.

In this section, we repeat the method for a very specific system that deserves special attention, because it served as a counterexample to the conjecture of Lins, de Melo and Pugh on the number of limit cycles for classical polynomial Liénard equations of degree 6 (and higher). Therefore, we recall a theorem from [102]:

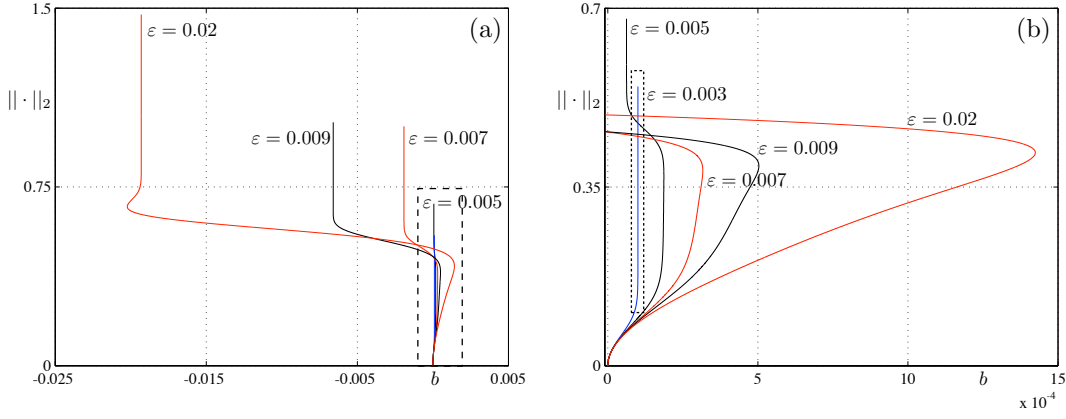


Figure 8: Branch of limit cycles in the  $F^\#$ -system for various values of  $\varepsilon$ . Panel (b) is a magnification of panel (a) near the region where one has three coexisting limit cycles for sufficiently small  $\varepsilon$ . A further magnification (dashed rectangle in panel (b)) leads to the situation described in Fig. 7

**Theorem 2.1.3** *Given the  $(\varepsilon, \delta, b)$ -family of polynomial Liénard equations of degree 6*

$$\begin{cases} \dot{x} &= y - \left(\frac{1}{2}x^2 + 5\delta x^3 - \frac{35}{46}x^4 - 12\delta x^5 + \frac{21}{46}x^6\right) \\ \dot{y} &= \varepsilon(b - x), \end{cases} \quad (21)$$

and given  $k \in \{1, 2, 3, 4\}$ , there exists a smooth curve

$$b = \varepsilon B_k(\varepsilon, \delta),$$

defined for  $\varepsilon \in [0, \varepsilon_0]$  and  $\delta \in [-\delta_0, \delta_0]$  (for some sufficiently small  $\varepsilon_0 > 0$  and  $\delta_0 > 0$ ), along which the vector field (21) has exactly  $k$  limit cycles when  $\delta \neq 0$  and  $\varepsilon \in ]0, \varepsilon_1(\delta)]$  for some  $\varepsilon_1: [-\delta_0, \delta_0] \rightarrow \mathbf{R}$  with  $\varepsilon_1(\delta) > 0$  for  $\delta \neq 0$ . All these limit cycles are hyperbolic, surrounding a hyperbolic focus (attracting when  $\delta < 0$  and repelling when  $\delta > 0$ ).

The proof is essentially an application of Theorem 2.1.1: the slow divergence integral  $I(Y, \delta)$ , depending on the parameter  $\delta$  here, clearly has the property  $I(Y, 0) \equiv 0$ . One shows that  $I(Y, \delta)$  perturbs to a nontrivial function when  $\delta \neq 0$ , having three simple zeros. We note that this theorem gives 4 limit cycles along  $b = \varepsilon B_4(\varepsilon, \delta)$ , for nonzero but small values of  $\delta$  and  $\varepsilon$ .

Besides numerical difficulties related to the slow-fast nature, one faces another numerical difficulty in tracing back the limit cycles: for  $\delta = 0$  and  $\varepsilon > 0$ , system (21) is a center. This means that the smaller  $\delta$ , the smaller the deviations in the first return map of the orbits; the larger  $\delta$ , the farther one deviates from the theoretical results.

*Numerical results for (21)*

We have been able to use numerical continuation to find 3 limit cycles. The way that this coexistence of limit cycle is seen, is by studying the canard curve  $b = b(Y)$ , as explained in Theorem 2.1.2. The appearance of 3 limit cycles is already a counterexample to the conjecture by Lins, de Melo and Pugh. For reasons that have been explained in detail in [102], it is better for the numerics to replace system (21) by the related system

$$\begin{cases} \dot{x} &= y - F^\#(x) \\ \dot{y} &= \varepsilon(b - x) \end{cases}, \quad (22)$$

with

$$F^\#(x) := 0.5x^2 - 0.1x^3 - 0.82337x^4 + 0.023x^5 + 0.4565x^6.$$

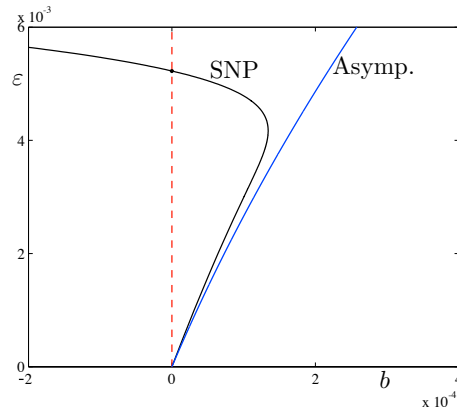


Figure 9: The locus of fold bifurcations of limit cycles (labeled SNP) in the two-parameter plane  $(b, \epsilon)$ . When this curve enters the half-plane  $b > 0$ , there exist a third limit cycle coexisting in the system for the associated  $b$ -value.

*Remark.* Theorem 2.1.3 not only gives information on (21): the theorem remains valid when we replace the  $\dot{x}$ -equation by an  $O(\epsilon)$ -perturbation of it. One can expect that among all those  $O(\epsilon)$ -perturbations, there are particular choices that optimize the way the numerics is predicted by Theorem 2.1.3. This is in fact the motivation of continuing with (22) instead of (21): having a fixed value of  $\epsilon$  in mind, one should consider (22) as such an  $O(\epsilon)$ -perturbation of (21) and hence one can expect similar results for this fixed value of  $\epsilon$ , provided it is taken small enough. For more details we refer to [102].

In Fig. 7, we show the results for  $b = b(Y)$  for  $\epsilon = 0.003$ . Panel (a) shows a large view of the bifurcation diagram of the system obtained when varying  $b$ , namely, the branch of limit cycles emanating from the Hopf bifurcation at  $b = 0$ . On the vertical axis, we use the  $L_2$ -norm as a measure of the solution. One can see from this computed branch that the Hopf bifurcation is subcritical and that the family of limit cycles undergoes a first fold bifurcation of limit cycles, which makes it change direction in  $b$  and allows for two limit cycles to coexist for a range of  $b$ -values. Soon after, the branch start increasing almost vertically. Panel (b) shows an enlargement of this region where we can see a second fold bifurcation of limit cycles. This allows for three limit cycles to coexist over a very small interval of  $b$ -values.

Experimenting with the value of  $\epsilon$ , we see that vertical branch showed in Fig. 7 (a) is shifted towards the right as  $\epsilon$  is increased. As soon as this vertical branch crosses the origin, we will only find 2 limit cycles instead of 3. On the other hand, as  $\epsilon$  is decreased, the numerics become more involved. It is therefore useful to see up to which value of  $\epsilon$  one can go in order for the vertical branch to be positive. The value of  $b$  at the vertical branch can be found by imposing a large limit cycle to exist. From Fig. 9, we derive that the maximum value for which 3 limit cycles are found in the given system lies around  $\epsilon_{\max} \approx 0.005$ . The curve of fold bifurcations in the  $(b, \epsilon)$ -plane could not be continued numerically for  $\epsilon < 0.003$ . Below that value, points on the curve were obtained individually, that is, using several one-parameter continuation runs instead of continuing the fold point in  $(b, \epsilon)$ ; the points computed individually were then interpolated to complete the fold curve. Close to the origin, it makes sense to compare the values of  $b$  with the curve obtained from the asymptotic expansion of the canard curve (only the first two terms have been computed); the curve obtained asymptotically is labeled Asymp. in Fig. 9, and is seen to correspond quite well to the curve computed numerically for  $\epsilon \approx 0$ .

To find the 4th limit cycle, we would need an extra enlargement of the curve in Fig. 7(b). With standard programs using double precision numerics, this can however not be achieved. Given the relation between the position of the folds and the zeros of the divergence integral (last zero with computed amplitude  $Y = 1.91 + O(\delta)$ ), it is not so hard to give an idea of the precision that is needed to distinguish orbits starting near a cycle of fixed amplitude (and comparing them close



to the contact point): it is  $\exp \frac{-7.14 + O(\delta)}{\varepsilon}$ , yielding about  $10^{-620}$  for  $(\delta, \varepsilon) = (0, 0.005)$ . From this heuristical argument, it is clear that there is no hope to find the third fold (and hence the fourth limit cycle).

## 2.2 CANARDS AND INFLECTION LINES

The inflection-line method was first introduced by Okuda under the name of *inflector* in the mid-1970s [116] for planar excitable systems such as the Bonhoeffer-Van der Pol model. More than a decade later, Peng *et al.* [119] re-introduced this idea in the more general context of canard-explosive systems [12, 113]. Later, Brøns and Bar-Eli [16, 17] further developed this idea and compared the asymptotic expansion in  $\varepsilon$  of some branches of the inflection sets with that of other dynamical objects used to characterise canard solutions, in particular repelling slow manifolds [91, 113]; see section 2.2.1 below. They showed that, for planar slow-fast systems with an S-shaped critical manifold (given by the graph of a cubic function in the simplest cases), the inflection set and the repelling slow manifold are  $O(\varepsilon^2)$ -close to one another in between both fold points of the fast nullcline; we will come back to this approximation in section 2.2.1.2. In the past few years, a similar approach has been used to derive implicit equations for slow manifolds away from non-hyperbolic regions [57]. Finally, the inflection line method has been very recently revisited in [23] from the viewpoint of the dependence of the zero curvature region on the time scale ratio  $\varepsilon$ . This dependence allows to establish an upper bound in  $\varepsilon$  for the canard solutions to be well defined; see Section 2.2.2. Whether we look at limit cycles of transients, trajectories where the inflection-line method will give insight are those containing canard segments.

The main idea behind the inflection-line method is to notice that some of these special periodic solutions, once represented in the phase plane, correspond to curves that enclose convex regions, while others enclose non-convex regions of  $\mathbb{R}^2$ . We must stress here that these families of periodic solutions depend on system's parameters, so they do not coexist in general (for instance in the cases that we will be looking at in this section). However, in multiple time scale systems where the inflection method is relevant, the passage from convex trajectories to non-convex ones, in the phase plane, corresponds to an exponentially small parameter variation (i.e. a canard explosion), which typically affects neither the topological shape of the inflection set nor its location. Therefore, using an abuse of language, one can say that virtually the same inflection set “separates” convex closed trajectories from non-convex ones, even though they exist for exponentially close yet different parameter values and they are limit cycles. Such regions of inflection can be easily computed as solutions of implicit algebraic equations obtained from the definition of the local curvature of a planar curve; see section 2.2.1. They “separate” locally the small-amplitude periodic solutions from the large-amplitude ones. Moreover, when considering trajectories emanating from nearby initial conditions and for fixed parameter values, one does not need to make this abuse of language anymore. The inflection set allows to separate trajectories that transiently do not escape the basin of attraction of a rest state from those which escape it, make a large excursion (corresponding to a large-amplitude oscillation) and come back to it after some time. In the neuronal context, this corresponds to separating trajectories that do not cross the *excitability threshold* from those which do cross it and spike before coming back to a rest state; see Section 2.2.3.

### 2.2.1 The inflection-line method and its formulation in terms of singularity theory

#### 2.2.1.1 The idea of the method

In the phase plane, canards without head correspond to curves enclosing a convex region whereas canards with head correspond to curves enclosing a non-convex region, and the transition from one family to the other involves an exponentially small parameter variation; see Fig. 16. As explained above, by an abuse of language, we will say that regions of zero curvature of the flow, namely the

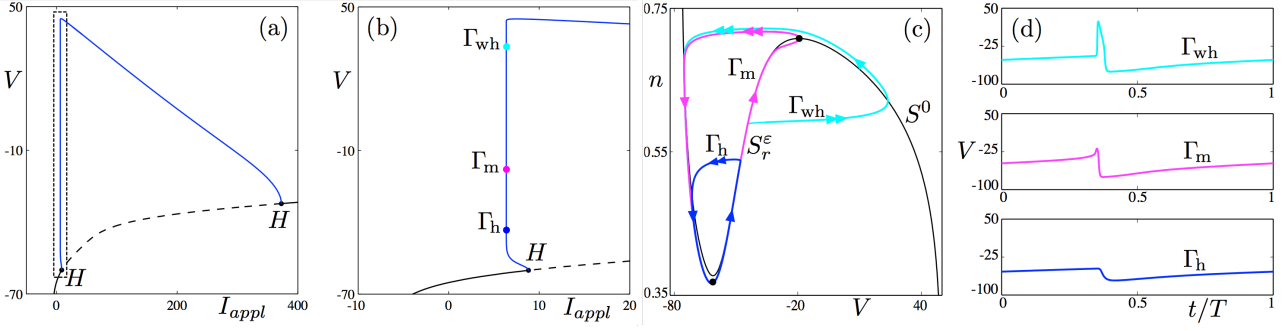


Figure 10: Canard explosion in the 2D Hodgkin-Huxley model. Panel (a) shows the bifurcation diagram of the model with respect to the applied current  $I$  and for the classical value of the Sodium conductance  $\bar{g}_{Na} = 120$ . The branch of steady states is shown in black; maximum  $V$ -values along the branch of limit cycle are shown in blue. One can observe two Hopf bifurcation points (labelled  $H$  and marked by a black dot). Panel (b) shows an enlargement of panel (a) in the vicinity of the canard explosion. Three solutions are highlighted on the quasi-vertical branch of the bifurcation diagram; they correspond to a canard without head ( $\Gamma_h$ ), the maximal canard ( $\Gamma_m$ ) and a canard with head ( $\Gamma_{wh}$ ), respectively. They are shown in the phase plane ( $V, n$ ) in panel (c) together with the critical manifold  $S^0$  and the repelling slow manifold  $S_r^\epsilon$ . Finally, their time traces for the variable  $V$  are displayed in panel (d).

inflection sets, can “separate” canards without head from canards with head. Strictly speaking, we can only fix a parameter value and say that in between a trajectory containing a “canard segment without head” (that is, a non-closed curve) and a trajectory containing a “canard segment with head”, there must be a region of zero curvature. For a planar vector field, these sets of inflection points of the flow can be computed by the local curvature. We recall that the local curvature of a planar curve  $y = y(x)$  [19], is given by

$$\kappa(x) = \frac{y''(x)}{(1 + y'(x)^2)^{\frac{3}{2}}}. \quad (23)$$

The general idea is to look at the curvature of the flow associated with a given planar dynamical system

$$X' = f(X, Y) \quad (24)$$

$$Y' = g(X, Y), \quad (25)$$

and to determine the regions of the phase plane where this curvature vanishes (i.e. regions referred to as *inflection sets*). Let us first recast system (24)–(25) as a planar slow-fast dynamical system by introducing a splitting between the time scale of  $X$  and that of  $Y$ , that is, we use the change of variable:  $(x, y) = (X, \varepsilon Y)$ . We then obtain the following two-dimensional singularly perturbed dynamical system

$$x' = f(x, y, \varepsilon) \quad (26)$$

$$y' = \varepsilon g(x, y, \varepsilon). \quad (27)$$

The equation for the trajectories associated with system (26)–(27) is obtained by eliminating time from the equations (26)–(27) and, hence, is given by  $dy/dx = \varepsilon g(x, y, \varepsilon)/f(x, y, \varepsilon)$ , more conveniently rewritten as

$$f(x, y, \varepsilon) \frac{dy}{dx} = \varepsilon g(x, y, \varepsilon). \quad (28)$$

Differentiating equation (28) with respect to  $x$ , and plugging in the condition for the local curvature to be 0, that is,  $\kappa(x) = 0$  — which reduces to  $y''(x) = 0$  by definition of  $\kappa(x)$  (see (23)) — yields, after simplification, the following equation for the inflection sets

$$f(f_x g - f g_x) + \varepsilon g(f_y g - f g_y) = 0. \quad (29)$$



See section 2.2.1.2 for details of this derivation. Equation (29), which relates the variables  $y$  and  $x$ , the singular parameter  $\varepsilon$  in addition to other parameters, defines the locus of inflection points.

### 2.2.1.2 Reformulation as a bifurcation problem with a distinguished parameter

We now proceed to understand the topological changes of the inflection sets upon parameter variations. To this end, singularity theory is employed. We consider the case where the system has a unique equilibrium. Starting from equations (26)–(27) and subsequently differentiating equation (28) with respect to  $x$  gives

$$f_x \frac{dy}{dx} + f_y \left( \frac{dy}{dx} \right)^2 + f \frac{d^2y}{dx^2} = \varepsilon \left( g_x + g_y \frac{dy}{dx} \right). \quad (30)$$

Recall that the inflection set is defined by the condition of curvature equal to 0, which is equivalent to the condition  $y''(x) = d^2y/dx^2 = 0$ . Setting  $y''(x) = d^2y/dx^2 = 0$  in (30) and using (28) we obtain the following equation

$$\varepsilon \left( \frac{f_x g}{f} - g_x \right) + \varepsilon^2 \left( f_y \frac{g^2}{f^2} - g_y \frac{g}{f} \right) = 0,$$

where, to facilitate the notation we have dropped the explicit dependence on  $(x, y, \varepsilon)$ . Subsequently, multiplying by  $f^2/\varepsilon$  gives

$$ff_x g - f^2 g_x + \varepsilon(f_y g^2 - f g_y g) = 0. \quad (31)$$

Equation (31) is a bifurcation equation defining the set of inflection points. Setting  $\varepsilon = 0$  we obtain

$$f(f_x g - f g_x) = 0, \quad (32)$$

or, equivalently,

$$f = 0 \quad \text{or} \quad f_x g - f g_x = 0, \quad (33)$$

In other words, the  $\varepsilon = 0$  inflection set is the union of the two curves  $f = 0$  and  $f_x g - f g_x = 0$ . The intersection points of the two sets are defined as the points on  $f = 0$  for which  $f_x = 0$  or  $g = 0$ , i.e. fold points or points where both  $f$  and  $g$  are 0. A particular and a general case for the form of  $f$  and  $g$  will be discussed in the following subsections.

### 2.2.1.3 Particular case for $f$ and $g$

Consider  $f(x, y) = -y + F(x)$  and  $g(x, y) = g(x)$  (i.e.  $g$  does not depend on  $y$ ). Additionally assume  $g'(x) > 0$ . Consequently, the equation for inflection points has the form

$$(-y + F(x)) \frac{dy}{dx} = \varepsilon g(x) \quad (34)$$

Repeating the procedure outlined in the previous section the following is obtained

$$g'(x)(-y + F(x))^2 - F'(x)g(x)(-y + F(x)) + \varepsilon(g(x))^2 = 0. \quad (35)$$

For  $\varepsilon = 0$ , equation (35) reduces to  $g'(x)(-y + F(x)) - F'(x)g(x) = 0$  or  $-y + F(x) = 0$ , compare with equation (33). To simplify, introduce a new variable  $z = -y + F(x)$ , divide both sides by  $g'(x)$  and introduce new functions  $\lambda(x) = F'(x)g(x)/g'(x)$  and  $\nu(x) = (g(x))^2/g'(x)$ . This results in the equation

$$z^2 - \lambda z + \varepsilon \nu = 0. \quad (36)$$

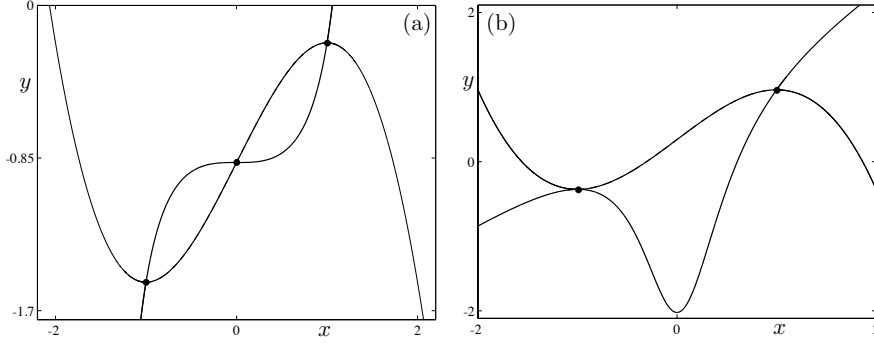


Figure 11: Inflection sets  $I_0$  for  $\varepsilon = 0$  computed in the FitzHugh-Nagumo system (71)-(72). They are formed by two components which correspond to  $\{f = 0\}$  (the critical manifold) and  $\{f_x g - f g_x = 0\}$ . Their intersection points are fold points of the critical manifold and the equilibrium point of the system, both labelled by dots. Panel (a) shows the regime away from a canard point. Panel (b) shows the regime at a canard point.

For  $\varepsilon = 0$  we have  $z = \lambda$  or  $z = 0$ , which corresponds to  $f_x g - f g_x = 0$  or  $f = 0$ ; compare with equation (33). Note that equation (36) fits in the framework of bifurcation problems with a distinguished parameter, in the sense of singularity theory, as described in Golubitsky and Schaeffer [58], with  $z$  being the state variable and  $\lambda$  the distinguished parameter. In fact  $z^2 - \lambda z = 0$  defines the bifurcation problem and the parameters, in this case,  $\varepsilon$  and the parameter controlling the canard explosion, serve to unfold it. Bifurcation points are defined by

$$z^2 - \lambda z = 0, \quad \frac{\partial(z^2 - \lambda z)}{\partial z} = 2z - \lambda = 0.$$

This gives the condition  $\lambda(x) = 0$ . Not surprisingly, bifurcation points correspond to the places where the two curves have a point in common. Moreover, since  $\lambda(x) = 0$  is equivalent to either  $F'(x) = 0$  or  $g(x) = 0$  the crossing points are either fold points or equilibria (intersections of the fast and the slow nullcline). To determine the nature of the bifurcation points we compute  $\lambda'(x)$  at fold points and points of intersection of the fast and slow nullcline

$$\begin{aligned} \lambda'(x) &= F'(x) && \text{if } g(x) = 0 \text{ and } F'(x) \neq 0 \\ \lambda'(x) &= \frac{F''(x)g(x)}{g'(x)} && \text{if } F'(x) = 0 \text{ and } g(x) \neq 0 \\ \lambda'(x) &= 0 && \text{if } F'(x) = 0 \text{ and } g(x) = 0 \end{aligned} \quad (37)$$

The first two equations of (37) correspond to a transverse crossing of the two curves. If the folds are non-degenerate then these two situations arise and the crossings of the two curves are transverse. Then the two components of the inflection set must be as shown in Fig. 11-a. The third equation in (37) corresponds to a canard point. The two inflection lines are tangent at the canard point, see Fig. 11-b. This is because in that case, the equilibrium is exactly at the fold in the singular limit  $\varepsilon = 0$ , which gives the condition for a canard point to occur; see [92] for more details.

We now consider the case of  $\varepsilon > 0$ . In the generic case (no canard point) we have three simple bifurcations (known also as transcritical bifurcations), see [58] page 205. To transform to the form of Golubitsky and Schaeffer we complete the square in (36), which yields

$$\tilde{z}^2 - \frac{\lambda^2}{4} + \varepsilon v = 0 \quad (38)$$

where  $\tilde{z} = z - \lambda/2$ . Note that case 1. of Golubitsky and Schaeffer cannot occur since  $\varepsilon v > 0$ . Indeed, the fact that  $\varepsilon v > 0$  implies that the perturbation of the transcritical bifurcation in the canard case gives two curves that are quadratic in  $x$  (case 2. of Golubitsky and Schaeffer) and not quadratic in  $y$  (case 1.). Interestingly, there are two cases to distinguish, near the folds, corresponding to the second equation in (37), and near the equilibrium point, corresponding to the first equation in (37).

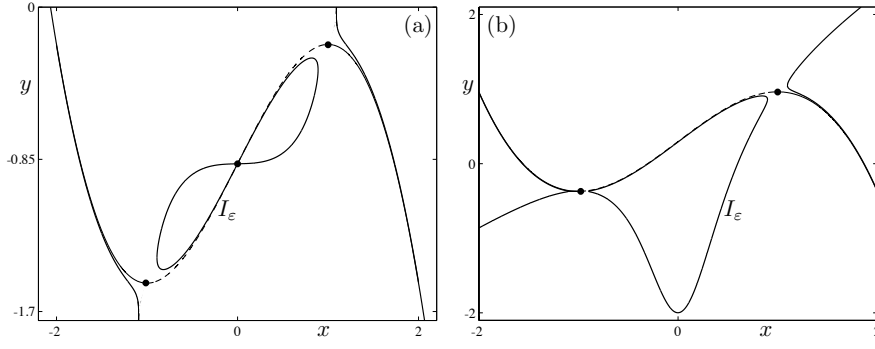


Figure 12: Inflection sets  $I_\varepsilon$  for  $\varepsilon > 0$ , computed in the FitzHugh-Nagumo system (71)-(72). Panel (a): away from a canard point. Panel (b): at a canard point (case 2 of Golubitsky and Schaeffer).

At a fold point  $(x_F, y_F)$  we have  $g(x_F) \neq 0$ , hence  $v = v_0 + O(x - x_F)$ , with  $v_0 > 0$ . Because of the constraint  $\varepsilon v > 0$  not all the cases of the full unfolding can be seen, however, when  $\varepsilon > 0$ , the transcritical bifurcation is perturbed to two saddle-node bifurcations. The inflection lines near the folds must then qualitatively have the form as shown in Fig. 12-a.

At an equilibrium  $(x_e, y_e)$  we have a  $g(x_e) = 0$ . Without loss of generality we assume that  $x_e = 0$ . It follows that  $\lambda^2(x) = Kx^2 + O(x^3)$ , where  $K > 0$  is a constant, and  $v(x) = O(x^2)$ . Equation (38) becomes

$$\tilde{z}^2 - (K + O(\varepsilon, x))x^2 = 0. \quad (39)$$

Hence, the transcritical bifurcation persists for  $\varepsilon > 0$ . The inflection lines near the equilibrium must then qualitatively have the form as shown in Fig. 12-a. Finally, we consider the case of a canard point, which we assume to be located at  $(x, y) = (0, 0)$  to simplify the analysis. However, note that the accompanying figures Figs. 11 and 12 will not reflect this translation to  $(0, 0)$ . We introduce a parameter  $\alpha$  that moves the nullcline  $g(x) = 0$ , i.e. unfolds the canard point. Specifically, we define  $\alpha$  to be the  $x$  coordinate of the equilibrium point. Hence the Taylor series of  $g$  has the following form:

$$g(x) = \sum_{j=1}^{\infty} g_j(x - \alpha)^j.$$

Without loss of generality assume that  $g_1 = 1$ . Hence (39) has the form

$$\tilde{z}^2 - \frac{Lx^2(x - \alpha)^2}{4} + \varepsilon(x - \alpha)^2 + R(x, \alpha, \varepsilon) = 0, \quad (40)$$

where  $L > 0$  is a constant and

$$R(x, \alpha, \varepsilon) = O(x^3(x - \alpha)^2) + O(x^2(x - \alpha)^3) + O(\varepsilon(x - \alpha)^3).$$

Without loss of generality assume  $L = 4$  (otherwise rescale the variables). We will first consider the truncated normal form

$$\tilde{z}^2 + (\varepsilon - x^2)(x - \alpha)^2 = 0, \quad (41)$$

and then argue that the bifurcation diagrams persist when the perturbation term  $R(x)$  is restored. First note that with  $\alpha = \varepsilon = 0$  (41) is the normal form 8- of [58], p. 208. This is a co-dimension three problem with a universal unfolding as shown in [58], p. 208. In (41) there are only two unfolding parameters,  $\varepsilon$  and  $\alpha$ . Moreover, a transcritical bifurcation occurs for (41) in a robust way (in an open set of  $(\alpha, \varepsilon)$ ) and is only present on the bifurcation variety for a versal unfolding. For completeness a sketch of the bifurcation analysis is provided subsequently; however detailed steps of the analysis can be found in [58].

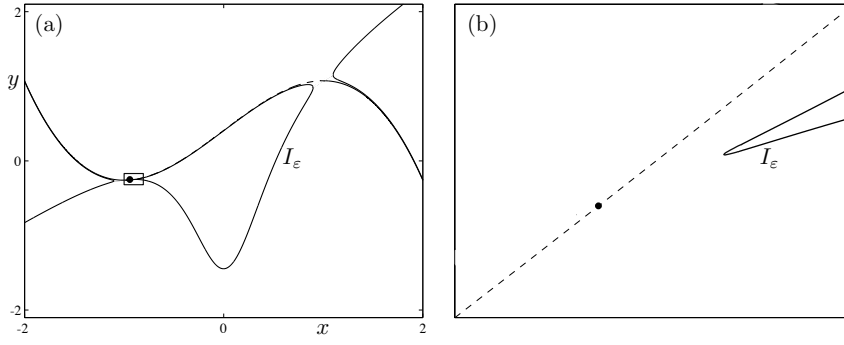


Figure 13: Inflection lines  $I_\varepsilon$  for  $\varepsilon > 0$  just before the transition focus-node:  $|\alpha| < \sqrt{\varepsilon}$ . Panel (b) is an enlargement of panel (a) in the vicinity of the equilibrium point (dot), which lies on the repelling branch of the critical manifold (dashed line).

**Case  $|\alpha| < \sqrt{\varepsilon}$ :** First determine the  $x$  intercepts. Setting  $\tilde{z} = 0$  we obtain  $x = \alpha$ ,  $x = \pm\sqrt{\varepsilon}$ . Note that  $(\alpha, 0)$  is an isolated point of the solution set, since for  $x \approx \alpha$  we have  $x^2 - \varepsilon < 0$ . At the points  $(-\sqrt{\varepsilon}, 0)$  and  $(\sqrt{\varepsilon}, 0)$  the solution curves have vertical tangents. For  $x > \sqrt{\varepsilon}$  there are two solution curves,  $z = \sqrt{x^2 - \varepsilon}(x - \alpha)$  and  $z = -\sqrt{x^2 - \varepsilon}(x - \alpha)$ . These two curves come together smoothly at  $(\sqrt{\varepsilon}, 0)$ . Similarly, for  $x < -\sqrt{\varepsilon}$  there are two solution curves,  $z = \sqrt{x^2 - \varepsilon}(x - \alpha)$  and  $z = -\sqrt{x^2 - \varepsilon}(x - \alpha)$ , which come together smoothly at  $(-\sqrt{\varepsilon}, 0)$ , see Fig. 13.

**Case  $|\alpha| > \sqrt{\varepsilon}$ :** The main change from the case  $|\alpha| < \sqrt{\varepsilon}$  is that the point  $(\alpha, 0)$  is not an isolated point of the solution set, but lies on both of the curves  $z = \sqrt{x^2 - \varepsilon}(x - \alpha)$  and  $z = -\sqrt{x^2 - \varepsilon}(x - \alpha)$ , which intersect at a non-zero angle. Hence  $(\alpha, 0)$  is a point of a transcritical bifurcation, see Fig. 15.

**Case  $|\alpha| = \sqrt{\varepsilon}$ :** We consider only  $\alpha = \sqrt{\varepsilon}$  as the case  $\alpha = -\sqrt{\varepsilon}$  is identical. There is only one  $x$  intercept, given by  $x = \sqrt{\varepsilon} = \alpha$ . For  $x > \sqrt{\varepsilon}$  there are two solution curves,  $z = \sqrt{x + \sqrt{\varepsilon}}(x - \sqrt{\varepsilon})^{3/2}$  and  $z = -\sqrt{x + \sqrt{\varepsilon}}(x - \sqrt{\varepsilon})^{3/2}$ . Hence  $(\sqrt{\varepsilon}, 0)$  is a cusp point. The other solution branch is the same as in the case  $\alpha > \sqrt{\varepsilon}$ . The solution set is shown in Fig. 14.

To see that the solution set of (40) is qualitatively the same as the solution set of (41) note that (40) can be rewritten in the form

$$\tilde{z}^2 + (\varepsilon(1 + O(x - \alpha)) - x^2(1 + O(x, x - \alpha)))(x - \alpha)^2 = 0, \quad (42)$$

The analysis carried out above can be applied to (42), with the same result. The only difference is that the transition point between the two generic cases would no longer be  $\alpha = \sqrt{\varepsilon}$  but would be the solution of an equation of the form  $\varepsilon = \alpha^2(1 + O(\alpha))$ .

#### 2.2.1.4 General case for $f$ and $g$

We now provide a brief explanation on how the previous analysis can be extended to more general planar systems. We still require that the fast equation is of the form  $\dot{x} = -y + F(x)$ , that is, it is locally given as a graph over  $x$ , and to preserve the S-shape form of the critical manifold. For the slow dynamics, the general case  $\dot{y} = \varepsilon g(x, y)$  is considered. Some non-degeneracy conditions will be provided below.

For this more general system, the inflection equation (35) reads

$$g_x z^2 + (\varepsilon g g_y - F'(x)g)z + \varepsilon g^2 = 0, \quad (43)$$

with, as before,  $z = -y + F(x)$ . In the regions of interest (i.e., near folds of  $S^0$  or near equilibria), we have  $z = -y + F(x) \sim 0$ . We can then expand  $g$  in powers of  $y$  with  $x$ -dependent coefficients, which yields

$$g = g_0(x) + g_1(x)y + g_2(x)y^2 + O(y^3), \quad (44)$$

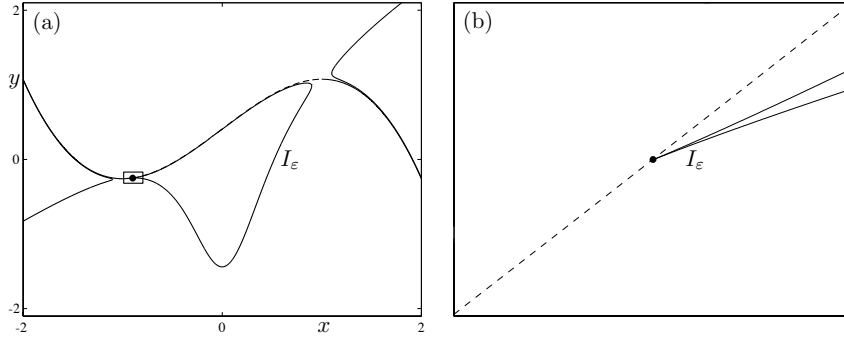


Figure 14: Inflection lines  $I_\varepsilon$  for  $\varepsilon > 0$  at the transition focus-node:  $|\alpha| = \sqrt{\varepsilon}$ . Panel (b) is an enlargement of panel (a) in the vicinity of the equilibrium point (dot), which lies on the repelling branch of the critical manifold (dashed line).

which can be rewritten as an expansion in  $z = -y + F(x)$ , giving

$$g = \widehat{g}_0(x) + \widehat{g}_1(x)z + \widehat{g}_2(x)z^2 + O(z^3), \quad (45)$$

where

$$\widehat{g}_0(x) = g_0(x) + g_1(x)F(x) + g_2(x)F(x)^2 + \cdots = g(x, F(x)), \quad (46)$$

$$\widehat{g}_1(x) = -g_1(x) - 2g_2(x)F(x) - 3g_3(x)F(x)^2 + \cdots = -\sum_{i=1}^{+\infty} ig_i(x)F(x)^{i-1} \quad (47)$$

Then, in the singular limit  $\varepsilon = 0$ , equation (43) becomes

$$g_x(x, z)z^2 - F'(x)g(x, z)z = 0. \quad (48)$$

Using (45), this reduces to

$$g_x(x, z)z^2 - F'(x)\widehat{g}_0(x)z - F'(x)\widehat{g}_1(x)z^2 + O(z^3) = 0, \quad (49)$$

that is,

$$-F'(x)g(x, F(x))z + (g_x - F'(x)\widehat{g}_1(x))z^2 + O(z^3) = 0. \quad (50)$$

However, by (45) and (46),

$$g(x, z) = g(x, F(x)) + O(z), \quad (51)$$

which implies

$$g_x(x, z) = g_x(x, F(x)) + O(z). \quad (52)$$

Now incorporating (47) and (52) into (50) gives

$$-F'(x)g(x, F(x))z + \left( g_x(x, F(x)) + \left( \sum_{i=1}^{+\infty} ig_i(x)F(x)^{i-1} \right) F'(x) \right) z^2 + O(z^3) = 0. \quad (53)$$

It is easy to see that

$$\sum_{i=1}^{+\infty} ig_i(x)F(x)^{i-1} = g_y(x, F(x)). \quad (54)$$

So equation (53) becomes

$$-F'(x)g(x, F(x))z + (g_x(x, F(x)) + g_y(x, F(x))F'(x))z^2 + O(z^3) = 0. \quad (55)$$

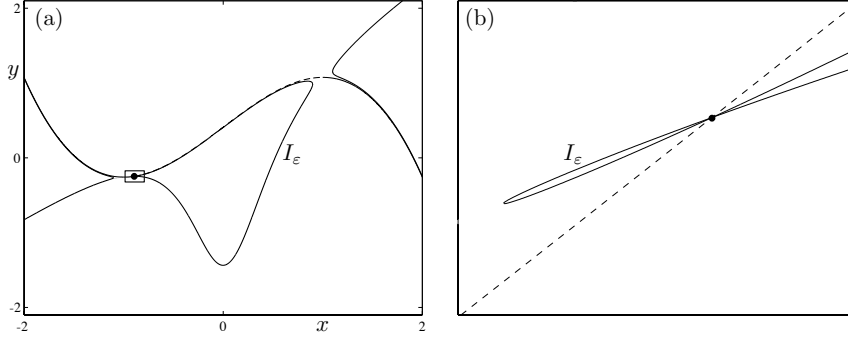


Figure 15: Inflection lines  $I_\varepsilon$  for  $\varepsilon > 0$  just after the transition focus-node:  $|\alpha| > \sqrt{\varepsilon}$ . Panel (b) is an enlargement of panel (a) in the vicinity of the equilibrium point (dot), which lies on the repelling branch of the critical manifold (dashed line).

Finally, the inflection equation for  $\varepsilon = 0$  has the form

$$-F'(x)g(x, F(x))z + \frac{d}{dx}g(x, F(x))z^2 + O(z^3) = 0. \quad (56)$$

Consequently, by taking the non-degeneracy condition  $\frac{d}{dx}g(x, F(x)) \neq 0$  and dropping terms of order greater than 3, the following bifurcation equation for the singular limit  $\varepsilon = 0$  is obtained

$$z^2 - \lambda z = 0, \quad (57)$$

with

$$\lambda = \frac{F'(x)g(x, F(x))}{\frac{d}{dx}g(x, F(x))}. \quad (58)$$

Therefore, we recover a similar equation as in the simpler case treated at the beginning of this section, that is, equation (36) for the singular limit  $\varepsilon = 0$ .

For  $\varepsilon > 0$ , equation (43) has the additional term

$$\varepsilon(gg_y + g^2).$$

Using equation (45) together with the fact that  $dz/dy = -1$ , results in

$$g_y = -\widehat{g}_1(x) - 2\widehat{g}_2(x)z - 3\widehat{g}_3(x)z^2 + O(z^3).$$

This allows to express the following

$$gg_y z = -\widehat{g}_0(x)\widehat{g}_1(x)z - (2\widehat{g}_0(x)\widehat{g}_2(x) + \widehat{g}_1(x)^2)z^2 + O(z^3), \quad (59)$$

$$g^2 = \widehat{g}_0(x)^2 + 2\widehat{g}_0(x)\widehat{g}_1(x)z + (2\widehat{g}_0(x)\widehat{g}_2(x) + \widehat{g}_1(x)^2)z^2 + O(z^3). \quad (60)$$

When adding equations (59) and (60), the terms in  $z^2$  cancel out. Consequently, the inflection equation (43) can be written as follows

$$z^2 - (\lambda + \varepsilon\widehat{\lambda})z + \varepsilon v = 0, \quad (61)$$

with

$$\widehat{\lambda} = \frac{\widehat{g}_1(x)g(x, F(x))}{\frac{d}{dx}g(x, F(x))}, \quad (62)$$

$$v = \frac{g(x, F(x))^2}{\frac{d}{dx}g(x, F(x))}. \quad (63)$$



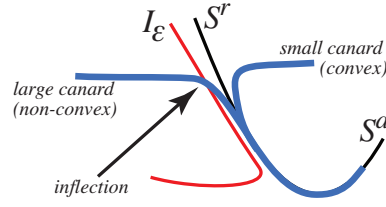


Figure 16: Curvature of a large canard cycle (with head) and small canard cycle (without head) near the repelling branch  $S^r$  of the critical manifold. A large canard cycle is characterised by the presence of an inflection point that makes it non-convex. Hence it crosses the inflection line  $I_\epsilon$  whereas the small canard does not.

and  $\lambda$  given by (58).

Completing the square in (61), transforms it to

$$\tilde{z}^2 - \frac{\lambda^2}{4} - \epsilon \frac{\lambda \hat{\lambda}}{2} - \epsilon^2 \frac{\hat{\lambda}^2}{4} + \epsilon \tilde{v} = 0. \quad (64)$$

Equation (64) can be rewritten in the Golubitsky-Schaeffer form

$$\tilde{z}^2 - \frac{\lambda^2}{4} + \epsilon \tilde{v} = 0, \quad (65)$$

where

$$\tilde{v} = \frac{g(x, F(x))^2}{\frac{d}{dx} g(x, F(x))} \left( 1 - \frac{1}{2} F'(x) \widehat{g_1}(x) - \frac{1}{4} \epsilon (\widehat{g_1}(x))^2 \right). \quad (66)$$

Note that (65) has the same form as (38) and the functions  $\lambda$  and  $\tilde{v}$  have the same structure as the terms  $\lambda$  and  $v$ , respectively, in (38). The analysis then follows in the same fashion as in Section 2.2.1.3 after equation (38).

Therefore, we have fully classified the geometry of inflection lines near and away from fold points (both jump points and canard points). We now turn to an interpretation of the dependence of inflection lines in  $\epsilon$ , in terms of existence of “well-defined” canard cycles, that is, where a transition between convex to non-convex cycles does occur. This can be seen as an attempt to characterise what “small enough” means for  $\epsilon$  in the context of planar slow-fast systems in the canard regime.

### 2.2.2 The “smallness” of $\epsilon$

Evidently, the appearance of canard cycles — convex when they are without head, non-convex when they are with head — is intimately related to the flow curvature. In two dimensions this can be understood by studying inflection points of the canard cycles. We now present a simple result that uses inflection lines to give a criterion to establish when canard cycles are possible. We can paraphrase this criterion as:

*A singularly perturbed system may contain canard cycles only if a locus of zero-curvature exists in the neighbourhood of the repelling sheet  $S^r$  of the critical manifold  $S_0 = S^a \cup S^r$ .*

We first derive this as a rigorous condition in the familiar context of the planar Van der Pol oscillator, before applying it to general Liénard systems, and finally to classical planar neuron models, namely, the FitzHugh-Nagumo model (in Section 2.2.3.1) and a reduction of the Hodgkin-Huxley model (in Section 2.2.3.2).

#### 2.2.2.1 Convexity of canard cycles in the Van der Pol system

Consider again the canard cycles of the Van der Pol oscillator. Hitherto we have distinguished canard types by whether, after traveling along the repelling branch  $S^r$  of the critical manifold, they

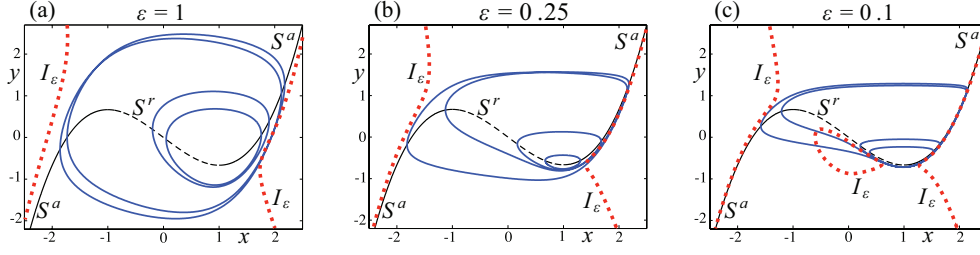


Figure 17: Comparison of four limit cycles of the Van der Pol system for: (a)  $\varepsilon = 1$ , (b)  $\varepsilon = \varepsilon_0 = 0.25$ , (c)  $\varepsilon = 0.1$ . Together with the orbits, the inflection curves  $I_\varepsilon$  now also shown (dotted). Notice that  $I_\varepsilon$  has a branch in the neighbourhood of  $S^r$  only in (c), when  $\varepsilon$  is small enough, and (b) is the marginal case where this branch vanishes.

curve away from  $S^r$  to form a small cycle (canard without head) or a large cycle (canard with head). An alternative is to express this difference in terms of local curvature along the canard cycles, specifically whether their curvature changes near the repelling branch  $S^r$  of the critical manifold, as depicted in Fig. 16. When the canard develops a head, its orbit in the Liénard plane undergoes a change in the sign of its curvature, which causes the canard with head to enclose a non-convex region of the plane. This non-convexity arises from competition between the slow time scale, which pulls the cycle along  $S^r$ , and the fast time scale, which pulls the cycle away from  $S^r$ .

Consider equation (29), which therefore corresponds to the zero set of the radius of convergence, i.e.,  $\kappa(x) = 0$ . Because a canard with head has a change in the sign of its local curvature near the repelling slow manifold, it should cross the set  $\kappa(x) = 0$ . As it does so it develops an inflection point, so the curves  $\kappa(x) = 0$  can be called inflection curves. If no inflection curves exist then all cycles in the plane must be convex, from which we infer that there is no significant separation of time scales, and hence there are no canards.

In the case of a slow-fast Liénard system, the inflection equation (29) becomes

$$g'(x)h^2 + f'(x)g(x)h - \varepsilon g(x)^2 = 0. \quad (67)$$

with  $h = y - f(x)$ . This quadratic equation depending on  $x$  has, for fixed  $\varepsilon$ , two solution branches  $h = h_\pm(x)$ , which in turn give two branches  $y = y_\pm(x)$  given by

$$y_\pm(x) = f(x) - \frac{g(x)}{2g'(x)} \left[ f'(x) \pm \sqrt{f'(x)^2 + 4\varepsilon g'(x)} \right]. \quad (68)$$

The inflection curve exists only if the solutions of (68) are real, hence

$$y_\pm(x) \in \mathbb{R} \Rightarrow (f'(x))^2 + 4\varepsilon g'(x) > 0. \quad (69)$$

Notice that this condition depends on  $\varepsilon$ . Clearly the condition is trivially satisfied if  $g'(x) > 0$  for all  $x$ .

In the case of the Van der Pol oscillator with  $f(x) = x^3/3 - x$  and  $g(x) = q - x$ , (69) implies  $(x^2 - 1)^2 - (2\sqrt{\varepsilon})^2 > 0$ . From this we find that for an inflection curve to exist we must have

$$\text{either} \quad f'(x) > +2\sqrt{\varepsilon} \iff x^2 > 1 + 2\sqrt{\varepsilon}, \quad (70a)$$

$$\text{or} \quad f'(x) < -2\sqrt{\varepsilon} \iff x^2 < 1 - 2\sqrt{\varepsilon}. \quad (70b)$$

Condition (70a) always has real solutions, but gives inflection curves in the regions  $|x| > \sqrt{1 + 2\sqrt{\varepsilon}}$ . These lie outside the folds of the critical manifold  $y = f(x)$  in the Van der Pol system (at  $x = \pm 1$ ), and therefore not in the neighbourhood of the repelling critical manifold  $S^r$ . We are therefore interested only in condition (70b), which gives inflection curves in the region  $|x| < \sqrt{1 - 2\sqrt{\varepsilon}}$ , which does contain the repelling slow manifold, and these have real solutions only if  $1 - 2\sqrt{\varepsilon} > 0$ . Thus we expect canards consisting of both large non-convex and small convex cycles in the Van der Pol oscillator, only if

$$\varepsilon < \varepsilon_0 := \frac{1}{4}.$$

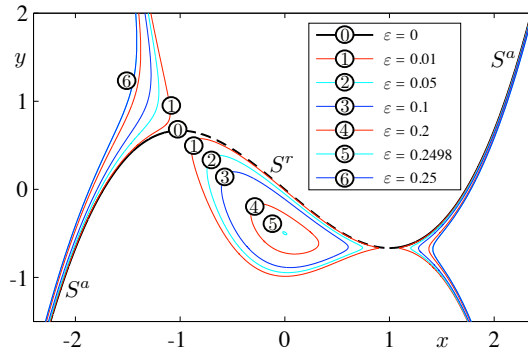


Figure 18: Comparison of the zero-curvature curves for the Van der Pol system for five different values of  $\varepsilon$  ranging from 0.01 to 0.25, respectively, as indicated in the legend.

We illustrate this criterion in Fig. 17, showing the inflection curves for three different values of  $\varepsilon$ : 0.1, 0.25, 1. For  $\varepsilon > \frac{1}{4}$  in Fig. 17(a), limit cycles appear almost circular, and the inflection curve exists only for  $|x| > 1$ . For the marginal case  $\varepsilon = \frac{1}{4}$  in Fig. 17(b), the inflection curves still exist only for  $|x| > 1$  but are noticeably deformed, and the cycle is developing an inflection. For  $\varepsilon < \frac{1}{4}$  in Fig. 17(c), a closed inflection curve has appeared in the region  $|x| < 1$  close to  $S^r$ , the cycle becomes non-convex where it crosses the curve, and is recognisably a canard. Thus the inflection condition  $\varepsilon < \frac{1}{4}$  clearly captures the characteristic canard shape, whereas the convex cycles for  $\varepsilon > \frac{1}{4}$  more closely resemble moderate distortions of circular cycles. Of course these are qualitative observations, but the requirement that an inflection curve exists in the neighbourhood of the repelling slow manifold solidifies them into a quantitative condition. The inflection curves for several different values of  $\varepsilon$  are plotted in Fig. 18. For the singular value  $\varepsilon = 0$  the inflection curve coincides with the critical manifold  $S_0$ . For finite  $\varepsilon$  it splits into three branches: two open curves in the regions  $|x| > 1$ , and a closed loop in the neighbourhood  $|x| < 1$  of the repelling critical manifold  $S^r$ . As  $\varepsilon$  increases this closed loop shrinks, until it vanishes at  $\varepsilon = \frac{1}{4}$ .

We therefore propose this upper bound in  $\varepsilon$ , which is obviously system-dependent, as a test for the existence of a well-defined canard explosion. If the parameter  $\varepsilon$  is too large, then the sharp change of local curvature, which is one of the most prominent characteristics of the planar canard phenomenon, disappears.

### 2.2.3 Application to neuronal excitability

In the context of neuronal models, the inflection set allows to discern between sub-threshold and spiking electrical activity. This transition can arise through a Hopf bifurcation, via a canard explosion, and this is typical for a large class of planar neuronal models (FitzHugh-Nagumo, reduced Hodgkin-Huxley), namely, type II neurons (*resonators*). This transition can also correspond to the crossing of the stable manifold of a saddle equilibrium, in the case of type I neurons (*integrators*). We compute inflection sets and study how well they approximate the excitability threshold of these neuron models, that is, both in the canard and in the non-canard regime, using tools from invariant manifold theory and singularity theory. With the latter, we investigate the topological changes that inflection sets undergo upon parameter variation. Finally, we show that the concept of inflection set gives a good approximation of the threshold in both the so-called *resonator* and *integrator* neuronal cases.

The concept of *excitability threshold*, in particular for neuronal models, is not well defined. This concept arises in an *ad hoc* manner as the transition between two observable states of excitable systems. In the case of neurons, the observed quantity is the electrical activity across the cellular membrane, and the associated states correspond to *inactive phases* (rest or weakly nonlinear oscillations) and *active phases* (large-amplitude oscillations denoted as *spikes* or *action potentials*). Defining unambiguously this transition is still an open problem both at the experimental and the theoretical level.

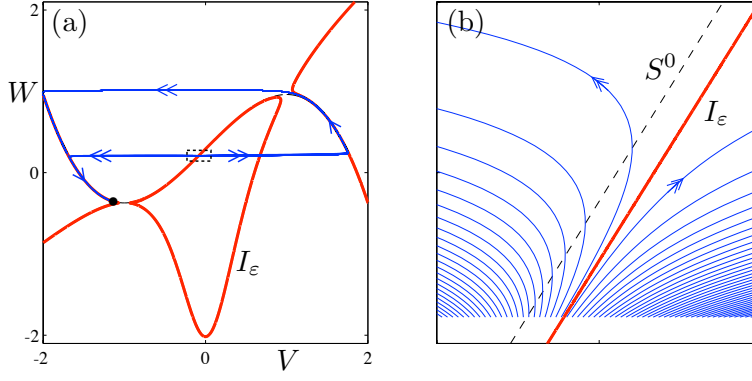


Figure 19: Inflection curves in the classical FitzHugh-Nagumo equations. Panel (a) shows a large view of the cubic critical manifold together with the three connected components of the solution set  $I_\epsilon$  for the inflection equation  $d^2V/dW^2 = 0$ ; also shown are 300 orbit segments obtained by forward simulation from a line of initial conditions, moving from one side of the middle component of the inflection equation to the other. Panel (b) shows an enlarged view of panel (a) close to the middle component of the inflection set (dashed box).

At the experimental level, the idea is to find by inspection the value of the voltage  $V$ , possibly depending on time, beyond which a rapid increase occurs that can be recognized as an action potential; recent studies include [125, 126, 138]. Several techniques have been considered, for example characterising the threshold in time as a solution of a differential equation [125]. On the theoretical side, different approaches have been proposed, depending on the particular family of models considered. Namely, the two main classes of neuronal models are *integrators* (type I neurons) and *resonators* (type II neurons) [78]. In the case of integrators, the excitability threshold is appropriately defined as an invariant manifold. However, it is ill-defined for resonators; refer to section 2.2.3.3. Alternatively, the excitability threshold has been approximated using the differential geometry of the voltage trace as a planar curve (local curvature, inflection points). Such ideas have been looked at from theoretical perspective [132] and also experimentally tested [138, 151, 150].

In this section, we propose to study the excitability threshold via identifying inflection lines of the flow in phase plane. The novelty of this approach consists in better characterising the excitability threshold using inflection lines in both the integrator and the resonator model classes.

### 2.2.3.1 The FitzHugh-Nagumo model

This classic phenomenological model is a polynomial two-dimensional reduction of the Hodgkin-Huxley that was independently developed by R. FitzHugh [54] and J. Nagumo [114]. The model equations read

$$\dot{V} = V - V^3/3 - W + I_{\text{appl}}, \quad (71)$$

$$\dot{W} = \epsilon(V + a - bW), \quad (72)$$

where we choose  $a = 0.7$ ,  $b = 0.8$ ,  $\epsilon = 0.01$  and vary the applied current  $I_{\text{appl}}$  as a bifurcation parameter. We place ourselves in the regime where the system has a unique equilibrium (type II neurons). The alternative where the system has more than one equilibrium (type I neurons) will be discussed in section 2.2.3.3, in particular Fig. 21 is an equivalent (in an enlarged view) of figures 19 and 20 for the type I case. System (71)–(72) possesses a cubic one-dimensional critical manifold. Varying  $I_{\text{appl}}$ , results in the appearance of two Hopf bifurcation points at the vicinity of each fold point (knee) of the critical cubic manifold  $\{(V, W); V - V^3/3 - W + I_{\text{appl}} = 0\}$ , seen in  $(V, W)$  variable space. The branches of limit cycles emerging from the Hopf points, feature canard explosions. Spiking solutions correspond to relaxation oscillations, which exist, in terms of parameter variation, once the canard

transitions have taken place. To distinguish between sub-threshold from super-threshold dynamics, the inflection set (29) for this system is computed via the following explicit expression

$$W_{\pm} = F(V) - \frac{1}{2(1-bF'(V))} \left[ (F'(V) - \varepsilon b)(V + a - bF(V)) \pm \sqrt{\Delta} \right] \quad (73)$$

with

$$\Delta = (V + a - bF(V))^2 ((F'(V) + \varepsilon b)^2 - 4\varepsilon), \quad F(V) = V - \frac{V^3}{3} + I_{\text{appl}}.$$

We will denote the inflection set as  $I_{\varepsilon}$ , which corresponds to the solutions of equations  $W_{\pm}$ . In this particular case, the real part of  $I_{\varepsilon}$  possesses three connected components as depicted in Fig. 19(a) (red curves). The “middle” component of  $I_{\varepsilon}$ , which lies in the region in-between the two folds of the critical manifold, disappears when  $W_{\pm}$  takes complex values, that is, as soon as  $(F'(V) + \varepsilon b)^2 - 4\varepsilon < 0$ . With the particular cubic function  $F$  corresponding to the FitzHugh-Nagumo system (71)–(72), this condition, together with the additional constraint that  $V$  must lie in between the two folds of the cubic nullcline ( $|V| < 1$ ), provides an upper bound in  $\varepsilon$  for the canard explosion to be well defined

$$\varepsilon < \varepsilon_{\text{crit}} = \left( \frac{1 - \sqrt{1-b}}{b} \right)^2. \quad (74)$$

Condition (74) is derived by noticing from equation (73) that the values of  $V$  bounding the intervals where the inflection equation has complex conjugated solutions are given by

$$V_{1\pm} = \pm \sqrt{1 + \varepsilon b + 2\sqrt{\varepsilon}} \quad (75)$$

$$V_{2\pm} = \pm \sqrt{1 + \varepsilon b - 2\sqrt{\varepsilon}} \quad (76)$$

In fact,  $V_{2\pm}$  are the abscissas of the fold point of the middle component of the inflection set (see Fig. 19). Now it becomes clear that the very existence of this middle component of the inflection set relies on the fact that  $V_{2+} \neq V_{2-}$ , which reduces to  $V_{2\pm} \neq 0$ . When  $V_{2\pm} = 0$ , the (real part of the) middle component of the inflection set shrink to a point, and that corresponds to  $\varepsilon = \varepsilon_{\text{crit}}$ . Further increasing  $\varepsilon$  does not give any component for the inflection set near the repelling branch of the critical manifold. This provides a second example (and first neuronal model) to the idea developed in Section 2.2.2.

The “middle” component of  $I_{\varepsilon}$ , explicitly given by (73), separates trajectories of small-amplitude from large-amplitude oscillations. Indeed, the trajectories with initial conditions taken on the left of  $I_{\varepsilon}$  (middle component) stay there for any future time whereas the trajectories with initial conditions taken on its right visit the three branches of the critical manifold; see Fig. 19(a). In other words, initial conditions to the left of the inflection curve converge to the stable equilibrium (black dot) following a short path whereas initial conditions taken on the right of this curve converge to the equilibrium after completing a spike. This shows that  $I_{\varepsilon}$  gives a good approximation of the threshold manifold.

### 2.2.3.2 Two-dimensional reduction of the Hodgkin-Huxley equations

The ground breaking work by Hodgkin and Huxley [73], which earned them the Nobel prize in 1963, produced the leading model for explaining the action potential generation. The Hodgkin Huxley model is formed by four nonlinear differential equations for the voltage  $V$ , the potassium current  $n$ , the sodium current  $m$  and the leak current  $h$ , respectively. See appendix 2.2.3.6 for a presentation of the original model with associated parameters. A two-dimensional reduction of the Hodgkin-Huxley model was derived in [113], building upon the work of [82, 129]. In this reduction, the  $m$  dynamics is assumed to be faster than  $h$  and  $n$ . That is,  $m$  is assumed to be slaved to  $V$  at all times. Moreover, the following linear equation between  $h$  and  $n$  is assumed to hold true:

$$n(t) + h(t) \approx 0.8.$$

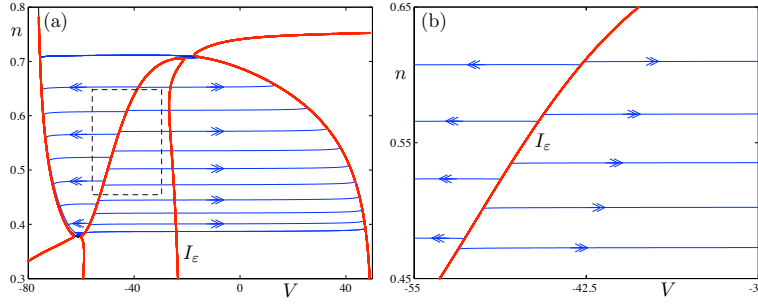


Figure 20: Inflection lines of the 2D Hodgkin-Huxley model together with canard cycles, for  $\bar{g}_{Na} = 120$ . Panel (b) is an enlargement of panel (a) in the region close to the repelling branch of the critical manifold (dashed box).

Consequently, a two-dimensional reduced model can be derived, which still reproduces the major features of the action potential generation. The following model equations represent the reduced dynamics of the transmembrane voltage and ionic currents:

$$C\dot{V} = I_{app} - \bar{g}_{Na} m_{\infty}(V)^3 (0.8 - n)(V - V_{Na}) - \bar{g}_K n^4 (V - V_K) - g_L (V - V_L), \quad (77)$$

$$\dot{n} = \alpha_n(V)(1 - n) - \beta_n(V)n, \quad (78)$$

with

$$m_{\infty}(V) = \frac{\alpha_m(V)}{\alpha_m(V) + \beta_m(V)}.$$

Similarly to the previous example, action potentials arise via a canard explosion in the two-dimensional reduction of the Hodgkin-Huxley model (77)–(78). As shown in Fig. 10, the voltage nullcline has a cubic shape (or S shape) with a Hopf bifurcation point in the vicinity of the lower fold point of the cubic curve. Then the action potential is generated through a canard explosion which gives rise to large-amplitude oscillations. A continuous variation of parameter  $I_{app}$  first induces canards without head (sub-threshold oscillations), followed by canards with head (first spiking orbits). The transition orbit passes tangentially through the upper fold of the critical manifold and is referred to as the maximal canard. Finally, relaxation cycles are observed. Note that for system (77)–(78), the Hopf bifurcation is subcritical, which means that there are unstable as well as stable canards without head [44, 91]. We also determine an accurate approximation of the threshold as a subset of the inflection set. In this particular case, the inflection set corresponds to a polynomial equation of degree 9 (see Appendix 2.2.3.6), which cannot be solved by radicals; thus we resort to the software MAPLE to solve it. In Fig. 20 a comparison between the inflection sets against the limit cycles computed via numerical continuation is performed. Observe that, as in the case of the FitzHugh-Nagumo model, the component of the inflection set located in between the two fold points of the critical manifold gives a good approximation of the voltage threshold manifold, which loosely speaking represents the curve in phase space separating initial conditions that lead to sub-threshold oscillations from initial conditions leading to a spike. Contrary to the FitzHugh-Nagumo model, which is polynomial and only reproduces the observed behaviour qualitatively, the Hodgkin-Huxley model contains variables and parameters of biophysical relevance. Hence, it makes sense to look at the dependence of the inflection set on parameter variation and to determine how it can affect the spiking activity of the model.

### 2.2.3.3 Threshold approximation via inflection set for integrators and resonators

A neuron is said to be excitable (non-spiking) when small fluctuation of the electrical activity does not cause the cell to spike; only a “large enough” perturbation from the rest state causes the cell to spike. This suggests that a well defined threshold will determine how much depolarisation the neuron membrane can sustain without producing a spike. However, the threshold will generically depend on the type of excitability (i.e. the dynamical mechanism that triggers spiking) of



the cell, which correspond to different bifurcation scenarios. Broadly speaking, in two-dimensional neuronal models there are two classes of excitability, which the neuroscience literature denotes as *Integrators* (or *type I neurons*) and *Resonators* (or *type II neurons*) [78]. In type I neurons, spiking solutions arise, upon variation of the applied current, via a Saddle-Node bifurcation on Invariant Circle (SNIC), that is, the creation of a limit cycle in place of a double connection between a saddle and a sink that coalesce and disappear in a saddle-node bifurcation; see [78] for more details. On the other hand, spiking solutions in type II neurons arise via a Hopf bifurcation. In the most simple case, both classes of models can be represented by the FitzHugh-Nagumo equations (71)–(72), which we recall here

$$\begin{aligned}\dot{V} &= V - V^3/3 - W + I_{\text{appl}}, \\ \dot{W} &= \varepsilon(V + a - bW).\end{aligned}$$

In type I neurons, there exists a saddle type equilibrium on the middle branch of the critical manifold for values of the bifurcation parameter before the SNIC bifurcation. Consequently, in the case of models of the form (71)–(72) the slow nullcline must be such that it intersects the S-shaped critical manifold three times. In contrast, in Type II neurons, the associated dynamical system has a unique equilibrium for all parameter values. In the (simple) case of the FitzHugh-Nagumo model, one can obtain a resonator or an integrator according to the chosen values of parameters  $a$  and  $b$ .

#### 2.2.3.4 Type I neurons

The SNIC bifurcation gives rise to a family of periodic orbits through an infinite period bifurcation. Consequently, the so-called current-frequency (I-f) curve is continuous through the bifurcation. Furthermore, in the context of two-dimensional integrator models, the *threshold manifold* is rigorously defined by the stable manifold of the saddle equilibrium. The saddle point must be on the repelling slow manifold. This follows from the fact that the repelling slow manifold is exponentially repelling for any initial conditions that are not on it, yet the equilibrium remains  $O(\varepsilon)$  close to it. Moreover, note that the dynamics reduced to the repelling slow manifold is an exponential contraction to the equilibrium. Hence the repelling slow manifold coincides in this case with the unique stable manifold of the saddle point and is then unique (see [55, 64] for basic material on stable manifolds). The two manifolds agree, up to a vicinity of the upper or the lower fold point of the critical manifold, and they can be extended beyond these points. Additionally, we show in this section that the inflection set, which also passes through the saddle equilibrium, is tangent at this point to both the repelling slow manifold and the stable manifold of this equilibrium. Since the inflection set and the repelling slow manifold are  $O(\varepsilon^2)$  close in this region (shown in section 2.2.3.5), the inflection set is also  $O(\varepsilon^2)$  close to the stable manifold of the saddle, that is, to the threshold, outside an  $\varepsilon$ -neighbourhood of the upper fold point of the critical manifold.

We now show that a subset of the inflection set is good approximation of the threshold. We perform the calculations in the general framework already considered in section 2.2.1.4, that is, the framework of Liénard type slow-fast systems. For simplicity, we will only assume a linear dynamics on the slow variable; the prototype system we are considering is the FitzHugh-Nagumo system (71)–(72), this is why we keep  $V$  and  $W$  for the variable names in what follows.

We then study a system of the form

$$\dot{V} = F(V) - W \tag{79}$$

$$\dot{W} = \varepsilon(V + a - bW). \tag{80}$$

In the particular case of system (71)–(72), we have  $F(V) = V - V^3/3 + I_{\text{appl}}$ . Let us assume that the system (71)–(72) has an equilibrium with real eigenvalues of opposite sign, that is, a saddle equilibrium, on the repelling branch of the critical manifold. This equilibrium has the form  $(V_{\text{eq}}, F(V_{\text{eq}}))$  where  $V_{\text{eq}}$  is the abscissa of one intersection point between the nonlinear nullcline  $\{W = F(V)\}$  and

the linear nullcline  $\{W = \frac{V+a}{b}\}$ . The inflection equation associated with system (79)-(80) can be written in the form

$$\left(\frac{dW}{dV}\right)^2 - (F'(V + \varepsilon b)) \frac{dW}{dV} + \varepsilon = 0, \quad (81)$$

and its solution gives the slope of the inflection set, in particular at the equilibrium point  $(V_{eq}, F(V_{eq}))$ , which by definition belongs to the inflection set. So we have

$$\left.\frac{dW}{dV}\right|_{\pm, (V_{eq}, F(V_{eq}))} = \frac{1}{2} \left( F'(V_{eq}) + \varepsilon b \pm \sqrt{(F'(V_{eq}) + \varepsilon b)^2 - 4\varepsilon} \right). \quad (82)$$

On the other hand, the Jacobian matrix  $J$  of system (71)-(72) at the equilibrium  $(V_{eq}, F(V_{eq}))$  is given by

$$J = \begin{pmatrix} F'(V_{eq}) & -1 \\ \varepsilon & -\varepsilon b \end{pmatrix}, \quad (83)$$

so its eigenvalues  $\lambda_{\pm}$  are

$$\lambda_{\pm} = \frac{1}{2} \left( F'(V_{eq}) - \varepsilon b \pm \sqrt{(F'(V_{eq}) + \varepsilon b)^2 - 4\varepsilon} \right), \quad (84)$$

and the associated eigenvectors  $v_{\pm} = (v_{1\pm}, v_{2\pm})$  satisfy

$$\frac{v_{1\pm}}{v_{2\pm}} = \frac{\lambda_{\pm} + \varepsilon b}{\varepsilon} = \frac{1}{2\varepsilon} \left( F'(V_{eq}) + \varepsilon b \pm \sqrt{(F'(V_{eq}) + \varepsilon b)^2 - 4\varepsilon} \right). \quad (85)$$

Consequently, the expressions (82) and (85) are identical and this demonstrates that each branch of the inflection set, evaluated at the equilibrium point, is tangent to an invariant manifold of this point (stable or unstable, depending on the branch). Note that from equation (84), we have a saddle equilibrium provided  $F'(V_{eq}) > \frac{1}{b}$ ; this is because one can rewrite the terms under the square root as  $(F'(V_{eq}) - \varepsilon b)^2 + 4\varepsilon(bF'(V_{eq}) - 1)$ . Furthermore, the right-hand side of equation (82) indicates that

$$\lim_{\varepsilon \rightarrow 0} \frac{v_{2+}}{v_{1+}} = 0. \quad (86)$$

On the other hand, doing a Taylor expansion about  $\varepsilon = 0$  of the right-hand side of equation (85) gives

$$\frac{v_{2-}}{v_{1-}} = F'(V_{eq})(1 + O(\varepsilon)). \quad (87)$$

Equations (86) and (87) tell us that the unstable manifold of the saddle equilibrium has a quasi-horizontal tangent at the equilibrium, and the stable manifold of the saddle equilibrium has the same slope as the critical manifold at the equilibrium, respectively. This confirms what can be observed in Fig. 12(a).

The above calculations prove that the threshold approximation by the inflection set holds for integrator type neurons. This shows that when the threshold is exactly given by the stable manifold of a saddle equilibrium, one recovers this approximation by considering the inflection line, which is easier to compute. An illustration of this point is given in Fig. 21 (a). The computation is made for system (71)-(72) with  $a = 0.7$ ,  $b = 1.5$  and  $I_{appl} = 0.465$ ; in particular the repelling slow manifold is computed by direct backward simulation using a stiff solver. It can be noticed in this figure that the threshold, given here by the stable manifold (blue curve) of the saddle equilibrium  $Eq = (V_{eq}, W_{eq})$  is very well approximated by one component of the inflection line. Note that the unstable manifold (green curve) of  $Eq$  is tangent to the inflection set at the equilibrium point, which comes from (82) and (85) as well.

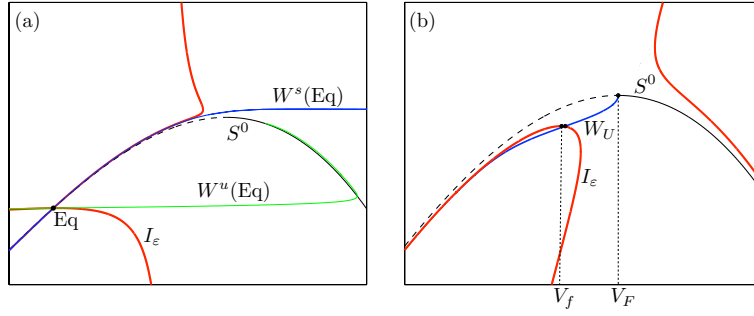


Figure 21: Approximation of the excitability threshold by the inflection line in both the integrator case (a) and the resonator case (b). Panel (a) gives an illustration of the closeness between the inflection line and the stable manifold  $W^s(Eq)$  of the saddle equilibrium  $Eq$  in the integrator case. For the resonator case, panel (b) provides an illustration of the distance between the upper fold point  $(V_F, W_F)$  of the critical manifold  $S^0$ , the upper horizontal fold point  $(V_f, W_f)$  of the inflection line  $I_\epsilon$  and the right-most point where the repelling slow manifold  $y_U$  meets the inflection line.

### 2.2.3.5 Type II neurons

Unlike the first case, *Type II neurons* admit sub-threshold oscillations. The transition from sub-threshold to spiking solutions occurs via a Hopf bifurcation for which the emanating branch of periodic solutions features a rapid transition through a canard explosion. This canard explosion starts with sub-threshold oscillatory (periodic) solutions (canard without head), followed by the first spiking solutions (canards with head) — which exist for a very small range of parameters — and then relaxation oscillations (full spiking dynamics) that persists for a wide parameter range. Note that, in this case there is no saddle equilibrium on the repelling branch of the critical manifold. Thus the threshold is more delicate to compute, however it is well approximated by the trajectory containing the maximal canard segment, that is, the repelling slow manifold [78].

It was proven in [17] that the upper part of the middle component of the inflection line is  $O(\epsilon^2)$ -close to the repelling slow manifold, for Liénard type systems of the form

$$\dot{V} = F(V) - W \quad (88)$$

$$\dot{W} = \epsilon(V - c), \quad (89)$$

(i.e.  $a = -c$ , and  $b = 0$  system (71)-(72)). More specifically, one has the following asymptotic expansions

$$W_U(V) = F(V) + \frac{c-V}{F'(V)}\epsilon + \left( \frac{c-V}{F'(V)^3} + \frac{(c-V)^2 F''(V)}{F'(V)^4} \right) \epsilon^2 + O(\epsilon^3) \quad (90)$$

$$W_i(V) = F(V) + \frac{c-V}{F'(V)}\epsilon + \frac{c-V}{F'(V)^3}\epsilon^2 + O(\epsilon^3), \quad (91)$$

where  $W_U$  denotes the repelling slow manifold and  $W_i$  the upper branch of the middle component of the inflection set  $I_\epsilon$ . The derivation of (90) essentially relies on formally expanding  $W_U$  in powers of  $\epsilon$  and then using the trajectory equation  $(F(V) - W) \frac{dW}{dV} = \epsilon(V - c)$ , plugging in the expansion for  $W_U$  in and equating the terms of same degree in  $\epsilon$ ; the derivation of (91) is obtained by simply taking a Taylor expansion of the square-root term in the solution to the inflection equation (81) about  $\epsilon = 0$ . Both calculations are explained in detail in [17].

By applying equation (29) to such a Liénard system, one can easily solve explicitly the quadratic inflection equation and show that these expansions are valid as long as  $F'(V)^2 - 4\epsilon > 0$  (see equation (35) in section 2.2.1.2), that is, outside a neighbourhood of size  $O(\epsilon)$  of the fold points of the critical manifold. Here again, only the middle component of the inflection set  $I_\epsilon$  can serve as an approximation of the threshold.

The above calculations prove that the repelling slow manifold — which in the case of type II neurons gives the best definition of the threshold — is  $O(\epsilon^2)$ -close to the inflection set, more specifically to the upper solution branch in the middle component of the inflection set, away from an

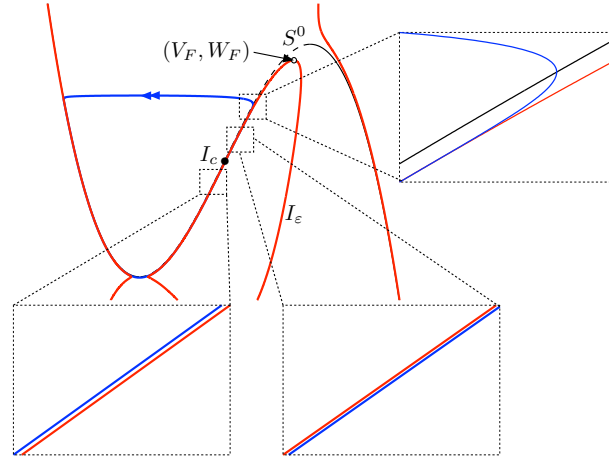


Figure 22: Example of limit cycle of the FitzHugh-Nagumo system that crosses the inflection line  $I_\varepsilon$  (see side panels) and do not spike. Also shown is the upper fold point  $(V_F, W_F)$  of  $I_\varepsilon$ , the critical manifold  $S^0$  and its inflection point  $I_c$ .

$\varepsilon$ -neighbourhood of the fold points; see Fig. 21(b) where the inflection set (in red) and the repelling slow manifold (in blue) start diverging from one another when approaching the upper fold point  $(V_F, W_F)$  of the critical manifold. It is then legitimate to try to delimit the portion of the inflection set that truly provides the best approximation to the threshold.

In order to identify the region where the inflection line gives a good approximation to the threshold, one can consider the upper horizontal fold point  $(V_f, W_f)$  of the middle component of  $I_\varepsilon$ . This point satisfies  $W'_i(V_f) = 0$ , where the  $\varepsilon$  expansion for  $W'_i$  is given by

$$W'_i(V) = F'(V) - \frac{1}{F'(V)^2} \left( (c - V)F''(V) \left( 1 + \frac{4}{F'(V)^2} \right) \right) \varepsilon + \quad (92a)$$

$$\frac{(c - V)F''(V) - F'(V)}{F'(V)^4} \varepsilon^2 + O(\varepsilon^3). \quad (92b)$$

An explicit  $\varepsilon$ -expansion of the abscissa  $V_f$  of this point is accessible once  $F$  is known explicitly.

The existence of this point  $(V_f, W_f)$  is guaranteed by the results obtained in Section 2.2.1.2 for the case  $\varepsilon > 0$  (as a perturbation of the situation at  $\varepsilon = 0$ ) at a canard point; see Fig. 12(b). Moreover, the maximal canard segment corresponds to the repelling slow manifold and, hence, the best approximation to the threshold in this case; it can be represented by an expansion in  $\varepsilon$  given by  $W = W_u$ . Besides, locally near  $(V_f, W_f)$ , both the maximal canard segment and the (upper branch of the middle component of the) inflection set are graphs of functions over  $V$ . It is then clear that the distance between both objects increases past the intersection point between these two objects, which we conjecture is at an distance of order  $\varepsilon^2$  from  $(V_f, W_f)$ . This is because the maximal canard segment goes up to the right fold of the critical manifold and the inflection set starts going down past its fold point. Therefore, one can consider that the inflection set gives a good approximation of the maximal canard segment and, hence, of the threshold, up to  $(V_f, W_f)$ , and we choose this point rather than the intersection point between the maximal canard segment and the inflection set, given that it is easier to compute and that they both converge to the upper fold  $(V_F, W_F)$  of the critical manifold as  $\varepsilon$  tends to zero. An illustration of this point is depicted in Fig. 21 (b), where the computations of the inflection line  $I_\varepsilon$  and the repelling slow manifold have been made in system (71)–(72) for  $a = 0.7$ ,  $b = 0.8$  and  $I = 0.29572$ .

### 2.2.3.6 Inflection sets as weak threshold boundaries for resonators

As discussed in the previous section, the inflection line provides a reasonable approximation to the excitability threshold, which can be quantified as a function of  $\varepsilon$ . However, in the case of resonator models, this approximation is weaker and the definition of threshold has to be extended. Following

Fig. 22, note there are trajectories that do traverse the inflection set without spiking, precisely, canards without head, whose “height” (with respect to the  $y$ -coordinate) is higher than the inflection point ( $I_c$ ) of the critical manifold  $S^0$ . That is, since the critical manifold has itself an inflection point, then for small enough  $\varepsilon$ , half of the family of canards without head do have an inflection point. In fact, these cycles traverse  $I_\varepsilon$  twice and this is illustrated in Fig. 22, in a case where one such cycle and  $I_\varepsilon$  exchange their positions (observe the zoomed side panels). Consequently, the inflection line should not be seen as providing a hard boundary for excitability threshold. It still gives an  $O(\varepsilon^2)$  approximation to the threshold, analytically tractable and easily computable, the best approximation remaining the maximal canard segment. A few trajectories do cross the inflection set without crossing the threshold and spiking, but they lie in phase space within an exponentially small region.

#### THE FULL HODGKIN-HUXLEY EQUATIONS

We recall here the four-dimensional Hodgkin-Huxley model from [73] together with the original parameter values. The equations read

$$\dot{V} = (I - \bar{g}_{Na} m^3 h (V - V_{Na}) - \bar{g}_K n^4 (V - V_K) - g_L (V - V_L)) / C, \quad (93)$$

$$\dot{n} = \alpha_n(V)(1 - n) - \beta_n(V)n, \quad (94)$$

$$\dot{m} = \alpha_m(V)(1 - m) - \beta_m(V)m, \quad (95)$$

$$\dot{h} = \alpha_h(V)(1 - h) - \beta_h(V)h, \quad (96)$$

where

$$\begin{aligned} \alpha_n(V) &= \frac{0.01(V + 55)}{1 - \exp(-0.1(V + 55))}, & \beta_n(V) &= 0.125 \exp(-(V + 65)/80), \\ \alpha_m(V) &= \frac{0.1(V + 40)}{1 - \exp(-0.1(V + 40))}, & \beta_m(V) &= 4 \exp(-(V + 65)/18), \\ \alpha_h(V) &= 0.07 \exp(-0.05(V + 65)), & \beta_h(V) &= \frac{1}{1 + \exp(-0.1(V + 35))}. \end{aligned}$$

The original parameter values for the Hodgkin-Huxley equation are given in the table below

Ionic conductances (mmho/cm <sup>2</sup> )			Reversal potentials (mV)			Membrane capacitance (μF/cm <sup>2</sup> )
$\bar{g}_{Na}$	$\bar{g}_K$	$g_L$	$V_{Na}$	$V_K$	$V_L$	$C$
120	36	0.3	50	-77	-54.4	1

Elements of the material presented in this chapter have been published in [28]. Our main contribution to the work presented in this chapter concerns the numerical computation of slow manifolds and canards near a folded-node singularity as well as the computation of branches of such canards, in the context of both minimal folded-node systems and more general MMO slow-fast systems. We first recall the main results about canards near a folded node, as well as a couple of other mechanisms that can generate MMO dynamics. Then, we explain the numerical method (based on the continuation of BVPs) in detail; the method to compute folded-node canards is illustrated, in particular, on a three-dimensional reduction of the Hodgkin-Huxley model. Finally, in the last section, we give preliminary results that aim to extend the singularity theory approach for inflection lines developed in Chapter 2 (Section 2.2.1.2) to the case of “two slow/one fast” systems near a folded node.

Oscillations with clearly separated amplitudes have been observed in several application areas, notably in chemical reaction dynamics [74, 6, 157]. Within each period, pairs of small-amplitude oscillations (SAOs) alternate with pairs of large-amplitude oscillations (LAOs). The result is an example of a *mixed-mode oscillation*, or MMO, displaying cycles of (at least) two distinct amplitudes. There is no accepted criterion for this distinction between amplitudes. The pattern of consecutive large and small oscillations in an MMO is an aspect that draws immediate attention. Customarily, the notation  $L_1^{s_1} L_2^{s_2} \dots$  is used to label series that begin with  $L_1$  large amplitude oscillations, followed by  $s_1$  small-amplitude oscillations,  $L_2$  large-amplitude oscillations,  $s_2$  small-amplitude oscillations, and so on. We will call  $L_1^{s_1} L_2^{s_2} \dots$  the *MMO signature*; it may be periodic or aperiodic. Signatures of periodic orbits are abbreviated by giving the signature of one period. Additionally, MMOs have been observed in laser systems and in neurons. We present an example with a three-dimensional reduction of the famous Hodgkin-Huxley model for Action Potential generation [73, 135, 136].

Mixed-mode oscillations may be periodic orbits, but we then ask questions that go beyond those typically examined by standard/classical dynamical systems theory. Specifically, we seek to dissect the MMOs into their epochs of small- and large-amplitude oscillations, identify each of these epochs with geometric objects in the state space of the system, and determine how transitions are made between these. When the transitions between epochs are much faster than the oscillations within the epochs, we are led to seek models for MMOs with multiple time scales.

Early studies of MMOs in model systems typically limited their investigations to cataloging the patterns of MMO signatures found as a parameter is varied. Barkley [5] is an exception: he assessed the capability of multiple-time-scale models for MMOs to produce the behavior observed by Hudson, Hart and Marinko [74]. He compared the MMOs from these experiments and from a seven-dimensional model for the BZ reaction proposed by Showalter, Noyes and Bar-Eli [141] with three-dimensional multiple-time-scale models. Barkley was unable to produce a three-dimensional model with the qualitative characteristics of the MMOs in the larger model, but such models with many of the desired properties were subsequently found. In this section, our central focus is upon MMOs whose SAOs are a byproduct of local phenomena occurring in generic multiple-time-scale systems. Analogous to the role of normal forms in bifurcation theory, understanding the multiple-time-scale dynamics of MMOs in their simplest manifestations leads to insights into the properties of MMOs in more complex systems.



## 3.1 SLOW-FAST MECHANISMS FOR MMOS; APPLICATION TO NEURONAL DYNAMICS

## 3.1.1 Three main slow-fast scenarios

## 3.1.1.1 The folded node scenario

Folded nodes are only defined for the singular limit (4) of system (1) on the slow time scale. However, they are directly relevant to MMOs because for  $\varepsilon > 0$  small enough, trajectories of (1) that flow through a region where the reduced system has a folded node, undergo small oscillations. Benoît [8, 9, 10] first recognized these oscillations. Wechselberger and collaborators [18, 144, 156] gave a detailed analysis of folded nodes while Guckenheimer and Haiduc [63] and Guckenheimer [61] computed intersections of slow manifolds near a folded node and flow maps along trajectories passing through these regions. From Theorem 1.1.2 we know that the eigenvalue ratio  $0 < \mu < 1$  at the folded node is a crucial quantity that determines the dynamics in a neighborhood of the folded node. In particular,  $\mu$  controls the maximal number of oscillations. The studies mentioned above use normal forms to describe the dynamics of oscillations near a folded node. Two equivalent versions of these normal forms are

$$\begin{cases} \varepsilon \dot{x} &= y - x^2, \\ \dot{y} &= z - x, \\ \dot{z} &= -v, \end{cases} \quad (97)$$

and

$$\begin{cases} \varepsilon \dot{x} &= y - x^2, \\ \dot{y} &= -(\mu + 1)x - z, \\ \dot{z} &= \frac{1}{2}\mu. \end{cases} \quad (98)$$

Note that  $\mu$  is the eigenvalue ratio of system (98) and that  $v \neq 0$  and  $\mu \neq 0$  imply that no equilibria exist in (97) and (98). If we replace  $(x, y, z)$  in system (97) by  $(u, v, w)$  and call the time variable  $\tau_1$ , then we obtain system (98) via the coordinate change

$$x = (1 + \mu)^{1/2} u, \quad y = (1 + \mu) v, \quad z = -(1 + \mu)^{3/2} w,$$

and the rescaling of time  $\tau = \tau_1 / \sqrt{1 + \mu}$ , which gives

$$v = \frac{\mu}{2(1 + \mu)^2} \quad \text{or} \quad \mu = \frac{-1 + \sqrt{1 - 8v}}{-1 - \sqrt{1 - 8v}}. \quad (99)$$

Therefore, in system (97) the number of secondary canards changes with the parameter  $v$ : when  $v$  is small,  $\mu \approx 2v$ . If the “standard” scaling [144]  $x = \varepsilon^{1/2} \bar{x}$ ,  $y = \varepsilon \bar{y}$ ,  $z = \varepsilon^{1/2} \bar{z}$ , and  $t = \varepsilon^{1/2} \bar{t}$ , is applied to system (97), we obtain

$$\begin{cases} \bar{x}' &= \bar{y} - \bar{x}^2, \\ \bar{y}' &= \bar{z} - \bar{x}, \\ \bar{z}' &= -v. \end{cases} \quad (100)$$

Hence, the phase portraits of system (97) for different values of  $\varepsilon$  are topologically equivalent via linear maps. The normal form (100) describes the dynamics in the neighborhood of a folded node, which is at the origin here, with eigenvalue ratio  $\mu$  as given in (99). Trajectories that come from  $y = \infty$  with  $x > 0$  and pass through the folded-node region make a number of oscillations in the process, before going off to  $y = \infty$  with  $x < 0$ . There are no returns to the folded-node region in this system.

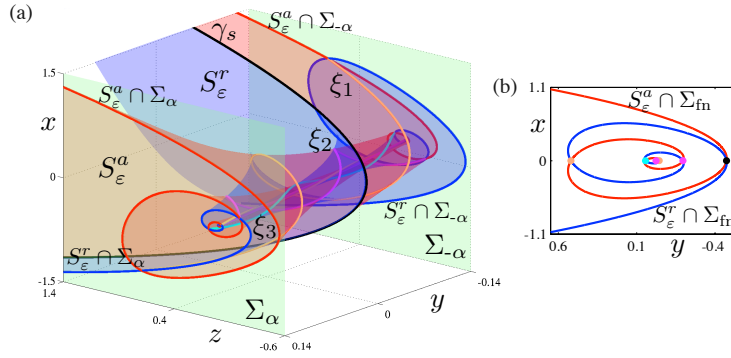


Figure 23: Invariant slow manifolds of system (100) with  $\nu = 0.025$  in a neighborhood of the folded node. Both the attracting slow manifold  $S_\varepsilon^a$  (red) and the repelling slow manifold  $S_\varepsilon^r$  (blue) are extensions of Fenichel manifolds. The primary strong canard  $\gamma_s$  (black curve) and three secondary canards  $\xi_1$  (orange),  $\xi_2$  (magenta) and  $\xi_3$  (cyan) are the first four intersection curves of  $S_\varepsilon^a$  and  $S_\varepsilon^r$ ; the inset shows how these objects intersect a cross-section orthogonal to the fold curve  $\{x = 0, y = 0\}$ .

Let us first focus on the number of small oscillations. If  $2k + 1 < \mu^{-1} < 2k + 3$ , for some  $k \in \mathbb{N}$ , and  $\mu^{-1} \neq 2(k + 1)$  then the primary strong canard  $\gamma_s$  twists once and the  $i$ -th secondary canard  $\xi_i$ ,  $1 \leq i \leq k$ , twists  $2i + 1$  times around the primary weak canard  $\gamma_w$  in an  $O(1)$  neighborhood of the folded-node singularity in system (100), which corresponds to an  $O(\sqrt{\varepsilon})$  neighborhood in systems (97) and (98) [144, 156]. (A twist corresponds to a half rotation.) We illustrate this in Fig. 23 for system (100) with  $\nu = 0.025$ . Note that  $\nu = 0.025$  corresponds to  $\mu \approx 0.0557$ . Hence,  $2k + 1 < \mu^{-1} \approx 17.953 < 2k + 3$  for  $k = 8$ , so Theorem 1.1.2 states that there exist eight secondary canards  $\xi_i$ ,  $1 \leq i \leq 8$ , along with the strong and weak canards  $\gamma_{s/w}$ . Figure 23 shows the attracting slow manifold  $S_\varepsilon^a$  and the repelling slow manifold  $S_\varepsilon^r$  of (100) in a three-dimensional region bounded by the planes  $\{z = \pm\alpha\}$ , denoted  $\Sigma_\alpha$  and  $\Sigma_{-\alpha}$ , with  $\alpha = 0.14$ ; see Section 3.2 for details on how these computations were done. Even though the rescaled normal form (100) does not depend on  $\varepsilon$  anymore, we still indicate the  $\varepsilon$ -dependence of the slow manifolds to distinguish them from the attracting and repelling sheets of the critical manifold; furthermore,  $S_\varepsilon^a$  and  $S_\varepsilon^r$  can be thought of as the slow manifolds of (97) or (98). Both manifolds are extensions of Fenichel manifolds and illustrate how the slow manifolds intersect near the fold curve of the critical manifold; the fold curve is the  $z$ -axis. Due to the symmetry

$$(\bar{x}, \bar{y}, \bar{z}, \bar{t}) \mapsto (-\bar{x}, \bar{y}, -\bar{z}, -\bar{t})$$

of the normal form (100), the two slow manifolds  $S_\varepsilon^a$  and  $S_\varepsilon^r$  are each other's image under rotation by  $\pi$  about the  $y$ -axis. The intersection curves in Fig. 23(a) are the canard orbits; labeled are the primary strong canard  $\gamma_s$  (black) and the first three secondary canards  $\xi_1$  (orange),  $\xi_2$  (magenta) and  $\xi_3$  (cyan). The inset panel (b) shows the intersection curves of  $S_\varepsilon^a$  and  $S_\varepsilon^r$  with the plane  $\Sigma_{fn} := \{z = 0\}$  that contains the folded node at the origin. Canard orbits are identified in  $\Sigma_{fn}$  as intersection points; only  $\xi_1$ – $\xi_3$  are labeled but notice that there are further canards (including the weak canard  $\gamma_w$ ) very close together in the center of the figure.

A trajectory entering the fold region becomes trapped in a region bounded by strips of  $S_\varepsilon^a$  and  $S_\varepsilon^r$  and two of their intersection curves. The intersection curves are maximal canards, and the trajectory is forced to follow the oscillations of these two bounding canard orbits. In order to illustrate how many canards there are and precisely how many oscillations they make, we show in Figure 24(a) the flow map of (100) with  $\nu = 0.025$ . Due to the strong contraction along  $S_\varepsilon^a$ , the flow map through the fold region is strongly contracting in one direction for trajectories that do not extend along  $S_\varepsilon^r$ . Hence, the flow map will be almost one dimensional and can be approximated by following trajectories starting on the critical manifold far away from the fold curve. The flow map shown in Figure 24(a) was obtained by integrating 500 equally-spaced initial values on the line segment  $\{x = 20, y = x^2 = 400, -3.25 \leq z \leq -0.75\}$  until they reach the plane  $x = -10$ ; plotted are the

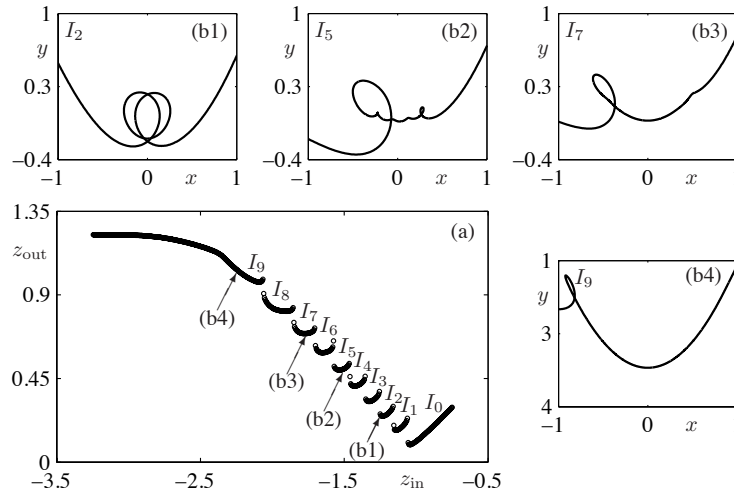


Figure 24: Numerical study of the number of rotational sectors for system (100) with  $\nu = 0.025$ . Panel (a) illustrates the flow map through the folded node by plotting the  $z$ -coordinates  $z_{\text{out}}$  of the first return to a cross-section  $x = -10$  of 500 trajectories with equally-spaced initial values  $(x, y, z) = (20, 400, z_{\text{in}})$ , where  $-3.25 \leq z_{\text{in}} \leq -0.75$ . Panels (b1)–(b4) show four trajectories projected onto the  $(x, y)$ -plane that correspond to the points labeled in panel (c), where  $z_{\text{in}} = -1.25$  in panel (b1),  $z_{\text{in}} = -1.5$  in panel (b2),  $z_{\text{in}} = -2$  in panel (b3), and  $z_{\text{in}} = -2.25$  in panel (b4).

$z$ -coordinates of the final values versus the initial values. One can see ten segments in this flow map that are separated by discontinuities. These discontinuities mark sectors on the line segment  $\{x = 20, y = x^2 = 400, -3.25 \leq z \leq -0.75\}$  that correspond to an increasing number of SAOs; in fact, each segment corresponds to a two-dimensional sector  $I_i$ ,  $0 \leq i \leq 9$ , on the attracting sheet  $S_\varepsilon^a$  of the slow manifold. The outer sector  $I_0$  on the right in Fig. 24(a) is bounded on the left by the primary strong canard  $\gamma_s$ ; sector  $I_1$  is bounded by  $\gamma_s$  and the first maximal secondary canard  $\xi_1$ ; sectors  $I_i$ ,  $i = 2, \dots, 8$ , are bounded by maximal secondary canard orbits  $\xi_{i-1}$  and  $\xi_i$ ; and the last (left outer) sector  $I_9$  is bounded on the right by  $\xi_8$ . On one side of the primary strong canard  $\gamma_s$  and each maximal secondary canard  $\xi_i$ ,  $1 \leq i \leq 8$ , trajectories follow the repelling slow manifold  $S_\varepsilon^r$  and then jump with decreasing values of  $x$ . On the other side of  $\gamma_s$  and  $\xi_i$ , trajectories jump back to the attracting slow manifold and make one more oscillation through the folded-node region before flowing toward  $y = \infty$ . The four panels (b1)–(b4) in Fig. 24 show portions of four trajectories projected onto the  $(x, y)$ -plane; their initial values are  $(x, y, z) = (20, 400, z_{\text{in}})$  with  $z_{\text{in}}$  as marked in panel (a), that is,  $z_{\text{in}} = -1.25$ ,  $z_{\text{in}} = -1.5$ ,  $z_{\text{in}} = -2$  and  $z_{\text{in}} = -2.25$  for (b1)–(b4), respectively. The trajectory in panel (b1) was chosen from the sector  $I_2$ , bounded by  $\xi_1$  and  $\xi_2$ ; this trajectory makes two oscillations. The trajectory in panel (b2) comes from  $I_5$  and, indeed, it makes five oscillations. The other two trajectories, in panel (b3) and (b4), make seven and nine oscillations, respectively, but some of these oscillations are too small to be visible.

The actual widths of the rotational sectors in Fig. 24 are very similar due to the  $\varepsilon$ -dependent rescaling used to obtain (100). When the equations depend on  $\varepsilon$  as in (97) and (98), however, the widths of the sectors depend on  $\varepsilon$ . In fact, all sectors are very small except for the sector corresponding to maximal rotation, which is bounded by  $\xi_k$  and the fold curve. For an asymptotic analysis of the widths of the rotational sectors that organize the oscillations, system (98) is more convenient, because the eigenvalues of the desingularized slow flow are  $-\mu$  and  $-1$ . Bröns, Krupa and Wechselberger [18] found the following.

**Theorem 3.1.1** *Consider system (12) and assume it has a folded-node singularity. At an  $O(1)$ -distance from the fold curve, all secondary canards are in an  $O(\varepsilon^{(1-\mu)/2})$ -neighborhood of the primary strong canard. Hence, the widths of the rotational sectors  $I_i$ ,  $1 \leq i \leq k$ , is  $O(\varepsilon^{(1-\mu)/2})$  and the width of sector  $I_{k+1}$  is  $O(1)$ .*

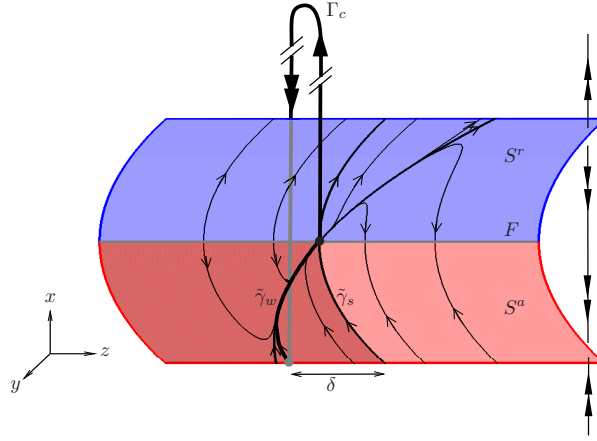


Figure 25: Schematic diagram of the candidate periodic orbit  $\Gamma_c$  that gives rise to MMOs with SAOs produced by a folded-node singularity. The candidate  $\Gamma_c$  approaches the folded node along the attracting sheet  $S^a$  (red) of the critical manifold (red) in the sector of maximal rotation associated with the weak singular canard  $\tilde{\gamma}_w$ . The distance to the strong singular canard  $\tilde{\gamma}_s$  is labeled  $\delta$ . When the trajectory reaches the folded node (black dot) it jumps along a layer and proceeds to make a global return.

Note that, as  $\mu \rightarrow 0$  (the folded saddle-node limit), the number of rotational sectors increases indefinitely, and the upper bounds on their widths decrease to  $O(\varepsilon^{1/2})$ .

**FOLDED NODE WITH A GLOBAL RETURN MECHANISM.** A global return mechanism may re-inject trajectories to the folded-node funnel to create an MMO. In this situation, we create a candidate trajectory as is illustrated in Fig. 25. Starting from the folded node we follow the fast flow until it returns to the funnel and then flows back to the folded node. Let us denote by  $\delta$  the distance from the singular strong canard  $\tilde{\gamma}_s$ , measured on a cross-section at a distance  $O(1)$  away from the fold, at which the candidate trajectory returns to the funnel. Provided that certain technical conditions are satisfied, one can show that this candidate gives rise to an MMO periodic orbit with signature  $1^s$ , where the number  $s$  of SAOs is as predicted by Theorem 3.1.1; this theorem also implies that the candidate is most likely to pass through the sector  $I_{k+1}$  of maximal rotation, where  $k$  is determined by the eigenvalue ratio  $\mu$ . Overall, we have the following result.

**Theorem 3.1.2 (Generic  $1^{k+1}$  MMOs [18])** Consider system (12) with the following assumptions:

- (A0) Assume that  $0 < \varepsilon \ll 1$  is sufficiently small,  $\varepsilon^{1/2} \ll \mu$  and  $k \in \mathbb{N}$  is such that  $2k+1 < \mu^{-1} < 2k+3$ .
- (A1) The critical manifold  $S$  is (locally) a folded surface.
- (A2) The corresponding reduced problem possesses a folded-node singularity.
- (A3) There exists a candidate periodic orbit (as constructed in Fig. 25), which consists of fast fibers of the layer problem, a global return segment, and a segment on  $S^a$  within the funnel that starts at distance  $\delta$  from  $\tilde{\gamma}_s$  (as measured at a distance  $O(1)$  away from the fold  $F$ ).
- (A4) An appropriate transversality hypothesis is satisfied.

Then there exists a stable MMO with signature  $1^{k+1}$ .

The transversality hypothesis of (A4) is cumbersome to formulate in a general setting. In the context of an S-shaped manifold, it concerns the projection of the two fold curves onto the opposite sheets of the attracting slow manifold and the flow along these sheets; see [18].

Theorem 3.1.2 not only requires sufficiently small  $0 < \varepsilon \ll 1$  but also  $\mu \gg \varepsilon^{1/2}$  (while  $0 < \mu < 1$ ). However,  $\varepsilon$  is usually of the order  $O(10^{-2})$  in applications, so that  $\mu$  must be close to 1 in order for the theorem to apply. Therefore, such maximal MMO signatures are seldom seen in applications. Furthermore, the SAOs for an MMO with signature  $1^{k+1}$  tend to be too small to be readily visible.

Figure 24 illustrates that the amplitudes of the SAOs are much larger for trajectories that approach the folded node close to the strong canard and lie in one of the sectors  $I_i$  with  $i \leq k$  rather than  $I_{k+1}$ . We know from Theorem 3.1.1 that the maximal width of a sector  $I_i$  with  $i \leq k$  is bounded from above by  $O(\varepsilon^{(1-\mu)/2})$  with  $\mu < 1/3$ . When  $\delta$  is  $O(\varepsilon^{(1-\mu)/2})$  one may actually find stable MMOs with  $i \leq k$  SAOs, which is the following result [18].

**Theorem 3.1.3** *Suppose system (12) satisfies assumptions (Ao)–(A3) of Theorem 3.1.2 and additionally:*

(A5) *For  $\delta = 0$ , the global return point is on the singular strong canard  $\tilde{\gamma}_s$  and as  $\delta$  passes through zero the return point crosses  $\tilde{\gamma}_s$  with nonzero speed.*

*Suppose now that  $\delta = O(\varepsilon^{(1-\mu)/2}) > 0$ . Then, for sufficiently small  $0 < \varepsilon \ll 1$  and  $k \in \mathbb{N}$  such that  $2k + 1 < \mu^{-1} < 2k + 3$  the following holds. For each  $i$ ,  $1 \leq i \leq k$ , there exist subsectors  $\tilde{I}_i \subset I_i$  with corresponding distance intervals  $(\delta_i^-, \delta_i^+)$  of widths  $O(\varepsilon^{(1-\mu)/2})$ , which have the property that if  $\delta \in (\delta_i^-, \delta_i^+)$  then there exists a stable MMO with signature  $1^i$ .*

Theorem 3.1.3 says that we should observe a succession of stable  $1^i$  MMOs with increasingly more SAOs as  $\delta$  increases (assuming that  $\mu$  remains fixed in such a parameter variation). In the transition from a  $1^i$  to a  $1^{i+1}$  MMO signature, that is, in the regions in between intervals  $(\delta_i^-, \delta_i^+)$  and  $(\delta_{i+1}^-, \delta_{i+1}^+)$  we expect to find more complicated signatures, which are usually a mix of  $1^i$  and  $1^{i+1}$ . Geometrically, different stable MMOs are selected as one moves the flow map in Fig. 24(a) up or down; since the rotational sector  $I_{k+1}$  for general  $\varepsilon$ -dependent systems has much larger width than the other sectors, one should expect that the transitions through  $I_i$  with  $i \leq k$  happen rather quickly during a parameter-induced variation of  $\delta$ .

If  $\mu = O(\varepsilon^{1/2})$ , that is, assumption (Ao) does not hold, then we may still expect stable MMO signatures of type  $1^{k+1}$ , as soon as the global returns falls inside the funnel region and  $\delta = O(1)$  [93]; note that  $k = O(1/\varepsilon^{1/2})$  and the amplitudes of the SAOs for such an MMO will again be tiny. If  $\mu = O(\varepsilon^{1/2})$  and  $\delta = O(\varepsilon^{1/2})$  as well, the mixed MMO signatures with larger-amplitude SAOs are more likely to occur. Here, global returns come very close to the secondary maximal canard  $\xi_2$ , first slightly to the left (hence, into the rotational sector  $I_2$  with two SAOs) and then slightly to the right (hence, into the rotational sector  $I_3$  with three SAOs), creating this MMO signature.

The theory described so far does not capture all of the possible dynamics near a folded node. If higher-order terms are included in the normal forms (97)–(98), then equilibria may appear in an  $O(\varepsilon^{1/2})$  neighborhood of the folded node as soon as  $\mu = O(\varepsilon^{1/2})$  or smaller. This observation motivates the study done, in particular, in [62], of the singular Hopf bifurcation in three dimensions.

### 3.1.1.2 The singular Hopf bifurcation scenario

Equilibria of a slow-fast system (1) always satisfy  $f(x, y, \lambda, \varepsilon) = 0$ ; generically, they are located in regions where the associated critical manifold  $S$  is normally hyperbolic. However, in generic one-parameter families of slow-fast systems, the equilibrium may cross a fold of  $S$ . When this happens the folded singularity at which the equilibrium crosses the fold curve is an actual equilibrium of the slow-fast system. In generic vector fields with two slow variables the folded singularity thus created is a folded saddle-node, which exists exactly at the specific parameter value at which the equilibrium crosses the fold curve; one speaks of a *folded saddle-node of type II* [108]. This is distinguished from the *folded saddle-node of type I* [144, 93], which refers to a saddle-node bifurcation of the reduced flow only, meaning that it does *not* involve a true equilibrium of the full system. This distinction stems from the fact that — as we have seen with the examples of the folded saddle and the folded node — a singularity of the reduced system need not be the projection of an equilibrium of the full slow-fast system. However, a folded saddle-node of type II is an actual equilibrium of the full system. Importantly, this implies that, when  $\varepsilon > 0$ , the system has a singular Hopf bifurcation, which occurs generically at a distance  $O(\varepsilon)$  in parameter space from the folded saddle-node bifurcation of type II [62].



### 3.1.1.3 Three-time-scale systems

When the coefficients  $\nu$ ,  $a$ ,  $b$  and  $c$  in the normal forms of the singular Hopf bifurcation [61, 62] are of order  $O(\varepsilon)$  or smaller, then  $z$  evolves slowly relative to  $y$  and the system actually has three time scales: fast, slow and super slow. Krupa et al. [94] studied this regime with geometric methods and asymptotic expansions for the case  $a = c = 0$ . They observed MMOs for which the amplitudes of the SAOs remain relatively large. Their analysis is based upon rescaling the system such that it has two fast variables and one slow variable. We will not develop further the case of three-time-scale systems in this manuscript; see [62, 94, 28] for more details.

### 3.1.2 MMOs in a reduced Hodgkin–Huxley system

We now develop a case study that illustrates these different local mechanisms for MMOs in the three-dimensional reduced Hodgkin–Huxley model, which features a folded node, but has a subcritical singular Hopf bifurcation; see [82, 135] for the derivation and also [27], where the same example was used. The reduced model only describes the dynamics for voltage ( $V$ ), the activation of the potassium channels ( $n$ ) and the inactivation of the sodium channels ( $h$ ); the activation of the sodium channels ( $m$ ) is very fast and it reaches its equilibrium state  $m = m_\infty(V)$  (almost) instantaneously which can be justified mathematically by a center-manifold reduction [135]. The evolution of the gates  $n$  and  $h$  is considered slow while the evolution of the voltage  $V$  is considered fast. To justify this time-scale separation, we nondimensionalize the Hodgkin–Huxley equations by introducing a dimensionless voltage variable  $v = V/k_v$  and a dimensionless time  $\tau = t/k_t$  where  $k_v = 100$  mV is a reference voltage scale and  $k_t = 1$  ms is a fast reference time scale; this gives

$$\begin{cases} \varepsilon \dot{v} = f(v, h, n) & := \bar{I} - m_\infty^3(v) h (v - \bar{E}_{Na}) \\ & \quad - \bar{g}_K n^4 (v - \bar{E}_K) - \bar{g}_L (v - \bar{E}_L), \\ \dot{h} = g_1(v, h) & := \frac{k_t}{\tau_h} \frac{(h_\infty(v) - h)}{t_h(v)}, \\ \dot{n} = g_2(v, n) & := \frac{k_t}{\tau_n} \frac{(n_\infty(v) - n)}{t_n(v)}, \end{cases} \quad (101)$$

with dimensionless parameters  $\bar{E}_x = E_x/k_v$ ,  $\bar{g}_x = g_x/g_{Na}$ , with  $x \in \{m, n, h\}$ ,  $\bar{I} = I/(k_v g_{Na})$  and  $\varepsilon = C/(k_t g_{Na}) =: \tau_v/k_t$ . The original Hodgkin–Huxley parameter values are given at the end of Chapter 2; we further assume:  $\tau_h = \tau_n = 1$ . Thus,  $\varepsilon = \frac{1}{120} \approx 0.01 \ll 1$  and system (101) represents a singularly perturbed system with  $v$  as a fast variable and  $(n, h)$  as slow variables. The functions  $x_\infty(v)$  and  $t_x(v)$ , with  $x \in \{m, n, h\}$ , describe the (dimensionless) steady-state values and time constants of the gating variables, respectively; they are given by

$$x_\infty(v) = \frac{\alpha_x(v)}{\alpha_x(v) + \beta_x(v)} \quad \text{and} \quad t_x(v) = \frac{1}{\alpha_x(v) + \beta_x(v)},$$

with

$$\begin{aligned} \alpha_m(v) &= \frac{(k_v v + 40)/10}{1 - \exp(-(k_v v + 40)/10)}, & \beta_m(v) &= 4 \exp(-(k_v v + 65)/18), \\ \alpha_h(v) &= 0.07 \exp(-(k_v v + 65)/20), & \beta_h(v) &= \frac{1}{1 + \exp(-(k_v v + 35)/10)}, \\ \alpha_n(v) &= \frac{(k_v v + 55)/100}{1 - \exp(-(k_v v + 55)/10)}, & \beta_n(v) &= 0.125 \exp(-(k_v v + 65)/80). \end{aligned}$$

The original Hodgkin–Huxley equations with scaling parameters  $\tau_h = \tau_n = \tau_m = 1$  shows no MMOs [73], but if  $\tau_h > \tau_{h,e} > 1$  or  $\tau_n > \tau_{n,e} > 1$  are beyond certain threshold values then MMOs are observed [27, 135, 136]. Here, we focus on a specific case with  $\tau_h = 6.0$ ,  $\tau_n = 1.0$  and  $C = 1.2$

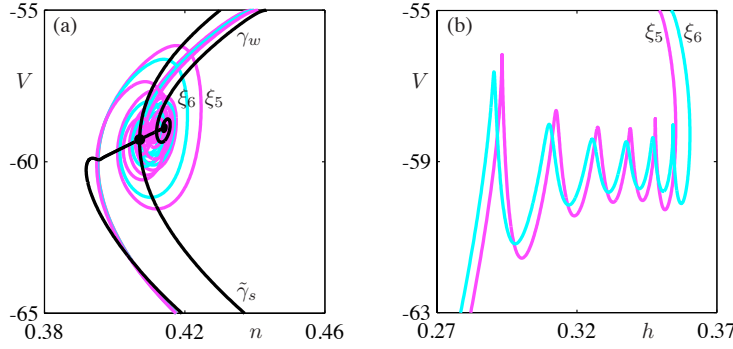


Figure 26: Maximal secondary canard orbits  $\xi_5$  and  $\xi_6$  of the three-dimensional reduced Hodgkin–Huxley equations (101) with  $\tau_h = 6.0$ ,  $\tau_n = 1.0$ ,  $C = 1.2$  and  $I = 12$ . Panel (a) shows the two canard orbits in projection onto the  $(n, V)$ -plane; also shown are the strong singular canard  $\tilde{\gamma}_s$  and the weak primary canard  $\gamma_w$ . The projection of  $\xi_5$  and  $\xi_6$  onto the  $(h, V)$ -plane in panel (b) shows that they make five and six oscillations, respectively.

(so that  $\varepsilon = 0.01$ ). We use the applied current  $I$  (in units of  $\mu\text{A}/\text{cm}^2$ ) of the original Hodgkin–Huxley equations, that is, the rescaled  $\bar{I}$  in (101), as the only free parameter. Furthermore, in order to facilitate comparison with other studies, we represent output in terms of the non-rescaled voltage  $V = 100v$ , which is in units of mV.

From a mathematical point of view, the MMOs are generated due to the presence of a (subcritical) singular Hopf bifurcation at  $I = I_H \approx 8.359$  and a folded node in the singular limit  $\varepsilon = 0$ . The critical manifold of (101) is defined by,

$$n^4(v, h) = \frac{\bar{I} - m_\infty(v)^3 h (v - \bar{E}_{\text{Na}}) - \bar{g}_L (v - \bar{E}_L)}{\bar{g}_K (v - \bar{E}_K)},$$

which is a cubic-shaped surface  $S = S^{a,-} \cup F_- \cup S^r \cup F_+ \cup S^{a,+}$  for physiologically relevant values of  $I$ . The outer sheets  $S^{a,\pm}$  are stable, the middle sheet  $S^r$  is unstable, and  $F_\pm$  denote fold curves [135]. The desingularized reduced system on this manifold is given by

$$\begin{cases} \dot{v} = \left(\frac{\partial}{\partial h} f\right) g_1 + \left(\frac{\partial}{\partial n} f\right) g_2, \\ \dot{h} = -\left(\frac{\partial}{\partial v} f\right) g_1. \end{cases}$$

A phase-plane analysis of the desingularized reduced flow in the physiologically relevant range shows that there exists a folded-node singularity on  $F_-$  for  $I > I_{\text{FSN}} \approx 4.83$ . Furthermore, it can be shown that the global-return mechanism projects into the funnel region for  $I < I_r \approx 15.6$ ; see [135, 136]. Hence, the folded-node theory predicts the existence of stable MMOs for a range of  $I$ -values that converges to  $I_{\text{FSN}} < I < I_r$  in the singular limit as  $\varepsilon \rightarrow 0$ .

Figure 26(a) shows the folded-node singularity for  $I = 12$ , where it lies approximately at  $(v, h, n) = (-0.593, 0.298, 0.407)$ , in projection onto the  $(n, V)$ -plane. The two black curves are the strong singular canard  $\tilde{\gamma}_s$  and the primary weak canard  $\gamma_w$  that pass through the folded node. The other two curves are maximal secondary canards  $\xi_5$  and  $\xi_6$  that were found as intersections of extended slow manifolds computed near the folded node; see also Section 3.2 and [27, Fig. 6]. Their projections onto the  $(h, V)$ -plane, which illustrate the oscillating nature of  $\xi_5$  and  $\xi_6$ , are shown in Fig. 26(b). Notice that the final oscillations of the primary weak canard  $\gamma_w$  in Fig. 26(a) show the distinct characteristics of saddle-focus-induced SAOs. Indeed, a saddle-focus equilibrium  $q \approx (-0.589, 0.379, 0.414)$  exists relatively close to the folded node, due to the singular Hopf bifurcation at  $I_H \approx 8.359$ . Decreasing  $I$  from  $I = 12$  toward  $I = I_H$  causes  $q$  to move closer to the folded node and the mix of folded node induced SAOs and saddle-focus induced SAOs will be more pronounced.

The equilibrium  $q$  for  $I = 12$  persists when  $I$  is varied. A partial bifurcation diagram is shown in Fig. 27(a), where we plot the maximum of  $V$  versus  $I$ . Similar to the analysis in [27], a unique



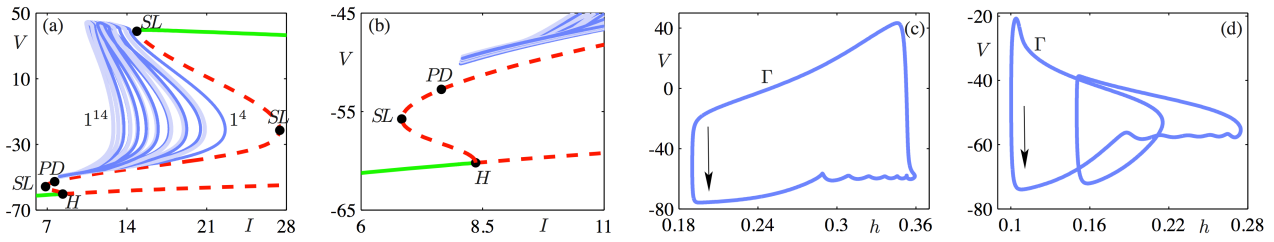


Figure 27: MMO periodic orbits of the three-dimensional reduced Hodgkin-Huxley equations (101) with  $\tau_h = 6.0$ ,  $\tau_n = 1.0$  and  $C = 1.2$ . Panel (a) shows a bifurcation diagram where the maximal  $V$ -value is plotted versus the applied current  $I$ . Isolals of MMO periodic orbits exist over a range of  $I$  bounded by a period-doubling bifurcation PD and a saddle-node of limit cycle bifurcation SL. The isolals are colored in alternating light and dark blue. Panel (b) shows an enlargement near the Hopf bifurcation. All isolals shown have a fold bifurcation for  $I_{SL} \approx 8.087$ . The periodic orbit  $\Gamma$  shown in panel (c) is the stable MMO for  $I = 12$ ; panel (d) shows  $\Gamma$  when it has a maximal  $V$ -value of  $-20$  mV.

equilibrium exists for all  $I$  and it is stable for  $I < I_H$  and, approximately,  $I > 270.772$ . The (singular) Hopf bifurcation (labeled H) at  $I_H$  gives rise to a family of saddle-type periodic orbits. This family of periodic orbits undergoes three fold bifurcations (SL) at  $I \approx 6.839$ ,  $I \approx 27.417$  and  $I = I_{SL} \approx 14.860$ , after which both non-trivial Floquet multipliers are less than 1 in modulus and the associated stable periodic orbits correspond to what is known in the field as tonic spiking. Figure 27(a) shows that the first SL is quickly followed by a period-doubling bifurcation (PD) at  $I \approx 7.651$ , where one of the Floquet multipliers, which are both unstable after this first SL, passes through  $-1$ . Hence, the periodic orbits after PD are non-orientable and of saddle type. Note that a second PD (not shown in Fig. 27(a)) must take place before the second SL.

MMOs exist as isolated families of periodic orbits for a range of  $I$ ; Fig. 27(a) shows eleven of these isolals colored in alternating light and dark blue. All periodic orbits on a single isola have the same number of oscillations. Each isola contains a short plateau with large maximal  $V$  near  $V = 40$  mV where the associated MMOs are stable and have signatures  $1^s$ . For our specific choice  $\varepsilon = 0.01$ , we found that the stable MMO interval appears to be bounded by  $I_H$  on the left and by  $I_{SL}$  on the right, that is,  $8.359 < I < 14.860$ . Recall that the theory based on the singular limit as  $\varepsilon \rightarrow 0$  predicts the existence of stable MMO periodic orbits with signatures  $1^s$  for  $4.83 \approx I_{FSN} < I < I_r \approx 15.6$ ; the match is surprisingly good, even though  $\varepsilon$  is relatively large. As  $I \downarrow I_H$ , the number  $s$  in the stable  $1^s$  MMO signatures approaches infinity, since a homoclinic orbit through the Hopf singularity is formed; see also [27]. Furthermore, there exist stable MMO signatures with more complicated signatures  $1^{s_1} 1^{s_2} \dots$ ; see [136]. The MMO periodic orbits go through several bifurcations along the isolals (mostly period-doubling and/or saddle-node of limit cycle bifurcations). The maximal  $V$ -value indicates the amplitude of the largest of the oscillations of the respective MMO periodic orbit. Note the folded structure of the isolals for  $V = V_{F_+} \approx -20$  mV which is approximately the repolarization threshold value for action potentials. This value also corresponds to the  $V$ -value of the upper fold curve  $F_+$ , at which a trajectory jumps back. For MMOs on a plateau, the LAOs correspond to a full action potential, while the  $s$  SAOs that follow are sub-threshold oscillations.

Figure 27(b) shows an enlargement of how the isolals of MMO periodic orbits accumulate near the Hopf bifurcation, which is the region where theory predicts a signature  $1^s$ , that is, an MMO with one large excursions and  $s$  SAOs. This is organized by how the global-return mechanism projects onto the critical manifold  $S$  as  $I$  varies. If the return projects onto a secondary canard then part of the periodic orbit follows the secondary canards onto the unstable branch  $S_{r,\varepsilon}$  of the slow manifold. However, only canard periodic orbits that reach the region of the upper fold curve  $F_+$  are maximal secondary canards. Hence, the corresponding family of secondary canards can be split into two groups: we call the secondary canards with maximum  $V < V_{F_+}$  *jump-back* canards and those with maximum  $V > V_{F_+}$  *jump-away* canards. This is an important distinction in this application, because the jump-away canards will create action potentials, the jump-back canards will not.

We illustrate the canards along one of the isolas shown in figures 27(a) and (b). The stable MMO periodic orbit  $\Gamma$  that exists on the plateau for  $I = 12$  is shown in Fig. 27(c); its signature is  $1^6$  and it lies on the isola that corresponds to periodic orbits with a total of seven oscillations. Note that the large excursion of  $\Gamma$  is above threshold. The six SAOs of  $\Gamma$  are due to the fact that the global return lands on the rotational sector bounded by the maximal secondary canards  $\xi_5$  and  $\xi_6$  for  $I = 12$  (not shown); compare Fig. 26(b). When the periodic orbit  $\Gamma$  is continued in the direction of increasing  $I$ , the maximal  $V$ -value decreases and the LAO changes from an action potential to a sub-threshold oscillation. Figure 27(d) shows  $\Gamma$  (which is now unstable) when its maximal  $V$ -value is approximately  $-20$  mV. Observe that  $\Gamma$  still has a total of seven oscillations, but now two of them have a fast segment. These fast segments are jump-back canards. More precisely, the periodic orbit  $\Gamma$  consists of a segment of a jump-back canard of the  $\xi_6$  canard family that connects to a segment of a jump-back canard of the strong canard family, which in turn connects to the former segment, hence, closing the loop. One could classify  $\Gamma$  in Fig. 27(d) as an MMO with signature  $2^5$ , because only five of its oscillations have really small amplitude due to the passage near the folded node, while there are two clearly distinguishable larger oscillations with fast segments due to jump-back canards. However, none of these larger canard oscillations of  $\Gamma$  are full action potentials, meaning that all oscillations are classified as SAOs in this application context.

### 3.2 COMPUTING SLOW MANIFOLDS AND CANARDS IN MMO SYSTEMS

This section discusses the numerical strategy that we used to compute the two-dimensional slow manifolds shown in many of the figures of this chapter. The slow manifold computations use numerical integration and boundary value methods to compute *orbit segments* that lie along the slow manifolds. An orbit segment is simply a finite piece of a trajectory of the vector field; as such, it has two endpoints and an associated integration time. In the context of computing slow manifolds, each such orbit segment is chosen to have one endpoint on the critical manifold away from its folds, where the critical manifold is a good approximation of the slow manifold one wishes to compute. Indeed, Fenichel's Theorem implies that the distance between the critical manifold and the slow manifold is  $O(\varepsilon)$ , and that trajectories flow from the critical manifold to an attracting or repelling slow manifold at an exponential rate in the appropriate time direction; see Theorem 1.1.1. Consequently, the computed orbit segments are expected to be as close to the slow manifold as the order of the numerical method allows, except for short  $O(\varepsilon)$  segments at one end where there is a fast transition from the critical manifold to the slow manifold in question. For stable or unstable manifolds of equilibria, orbit segments are chosen to lie in the linear eigenspace associated with the stable or unstable eigenvalues, respectively. The computational error associated with this approximation also decays quickly as one moves away from the endpoint; see [25, 87] for analysis of these approximation errors.

A simple and effective method for computing invariant manifolds as families of orbit segments is to use initial value solvers as the basic algorithm with initial conditions chosen on a mesh of points transverse to the flow in the invariant manifold; we call this the “sweeping” method. Despite its simplicity, this sweeping method fails to produce satisfactory results in some cases. In particular, strong convergence or divergence of trajectories toward one another makes the choice of the initial mesh problematic and can produce very non-uniform “coverage” of the desired manifold; see [45, 46]. In multiple-time-scale systems, the fast exponential instability of Fenichel manifolds that are not attracting makes initial value solvers incapable of tracking these manifolds by forward integration. These issues prompt the use of boundary value methods combined with continuation as an alternate strategy for computing invariant manifolds [88, 89]. We have used both strategies here. This section presents more details of the techniques used to compute attracting and repelling slow manifolds of systems with one fast and two slow variables, as well as the continuation of canard orbits when a parameter is varied.

### 3.2.1 A Boundary-Value Problem approach

#### 3.2.1.1 Sweeping invariant manifolds

The Fenichel manifolds of systems with a single fast variable are either attracting or repelling. As a result, forward trajectories with initial conditions on the critical manifold will converge quickly to an attracting Fenichel manifold and backward trajectories with initial conditions on the critical manifold will converge quickly to a repelling Fenichel manifold. Thus, one way to compute two-dimensional attracting and repelling Fenichel manifolds of a three-dimensional flow is to apply an initial value solver in the appropriate time direction to a mesh of initial conditions along a curve of the critical manifold transverse to the slow flow. We used this sweeping method to compute  $S_\varepsilon^+$  in Fig. 23; see also [109] for an early use of this method to compute two-dimensional invariant manifolds and Wechselberger [156] and Guckenheimer and Haiduc [63] for an example involving folded nodes.

When incorporated into a continuation framework, the sweeping method can also be used if the critical manifold is not known in closed form and the mesh of initial conditions cannot be selected beforehand. Continuation methods [35] provide well-established algorithms that augment equation solvers like Newton's method with strategies for choosing new starting points when solving under-determined systems of equations. More precisely, suppose  $F : \mathbb{R}^{m+n} \rightarrow \mathbb{R}^m$  is a smooth function given by  $m$  equations of  $m+n$  variables. The implicit function theorem states that the zeros of  $F$  form a smooth  $n$ -dimensional manifold  $M$  near points where the matrix  $DF$  of partial derivatives has full rank  $m$ . Moreover, the theorem gives a formula for the tangent space of  $M$ . Most continuation methods treat the case  $n = 1$  where the set of solutions is a curve; see [69] for the case  $n > 1$ . In general, the methods are based on a predictor-corrector procedure: given a point on  $M$ , tangent (or higher-order) information is used to choose a new seed for the solver to find a new point on  $M$ . The sweeping method described above selects the continuation step size based on equal increments of a specific coordinate or direction, but more sophisticated step size adaptations can be used as well.

#### 3.2.1.2 Continuation of orbit segments with boundary value solvers

The core algorithms of AUTO [38] are a boundary value problem solver and the numerical continuation of solutions of implicitly defined equations. The BVP solver of AUTO uses a collocation scheme, where solution segments are represented by piecewise polynomials (of a user-specified degree, usually between 3 and 5) that are defined on the mesh intervals of a user-specified mesh. Solving the ODEs at the collocation points gives a large system of equations for the coefficients of the polynomials that is solved by Newton's method. AUTO uses what is known as *pseudo-arclength* continuation to follow or continue solutions of such equations in a chosen parameter, where the step-size is adapted automatically; see [35] for details. The combination of a BVP solver and numerical continuation allows us to find and then continue one-parameter families of orbit segments that form (parts of) invariant manifolds of interest. The sweeping method described in the previous section can also be implemented in AUTO [38], so that the initial value problems are solved by collocation. The techniques described in this section impose boundary conditions on both end points of the orbit segments, which makes the method more versatile and suitable in a wider context; see also [88]. We describe here how to formulate two-point boundary value problems (BVP) in order to compute slow manifolds and associated canard orbits.

We consider two-point boundary value problems of the scaled form

$$\begin{cases} \dot{\mathbf{u}} &= T\mathbf{g}(\mathbf{u}, \lambda), \\ \mathbf{u}(0) &\in L, \\ \mathbf{u}(1) &\in \Sigma, \end{cases} \quad (102)$$

where  $\mathbf{g} : \mathbb{R}^n \times \mathbb{R}^p \rightarrow \mathbb{R}^n$  is sufficiently smooth,  $T \in \mathbb{R}$ ,  $\lambda \in \mathbb{R}^p$  are parameters and  $L$  and  $\Sigma$  are submanifolds of  $\mathbb{R}^n$ . The parameter  $T$  rescales time so that the orbit segments always correspond to

trajectories in the time interval  $[0, 1]$ . Hence, the boundary conditions at the two end points always apply to  $\mathbf{u}(0)$  and  $\mathbf{u}(1)$ , and  $T$  is the associated (unscaled) total integration time. In order to have a well-posed problem with isolated solutions, the number of boundary conditions should equal the number of equations ( $n$ , because  $(\mathbf{u}) \in \mathbb{R}^n$ ) plus the number of free parameters (at most  $p + 1$  for the parameter  $\lambda$  and the total integration time  $T$ ). We are interested in one-parameter families of solutions of (102), which means that we allow one fewer boundary condition (or one additional free parameter). Note that the total integration time  $T$  is typically unknown and may be viewed as the extra free parameter.

Let us first consider the computation of two-dimensional attracting and repelling slow manifolds  $S_\varepsilon^a$  and  $S_\varepsilon^r$ . To simplify the explanation, we assume that we have a three-dimensional slow-fast system with two slow variables and a folded node. In this context, the parameter  $\lambda$  remains fixed, and we obtain a one-parameter family of orbit segments (with unknown total integration times  $T$ ) by imposing a total of three boundary conditions. This means that the dimensions of  $L$  and  $\Sigma$  in (102) sum up to  $n = 3$ . Our approach is to choose  $L$  as a curve (e.g., a straight line) on the critical manifold, which requires two boundary conditions, and  $\Sigma$  as a surface (e.g., a plane), which requires one boundary condition, such that the associated one-parameter family of orbit segments covers the desired portion of the slow manifold. For example, in order for  $S_\varepsilon^a$  to come into the folded-node region, we let  $L$  be a curve on the attracting sheet of the critical manifold transverse to the slow flow and  $\Sigma$  be a surface orthogonal to the fold curve  $F$  at the folded node. The same approach works for  $S_\varepsilon^r$ , where we choose  $L$  on the repelling sheet of the critical manifold; note that  $T < 0$  for such a family of orbit segments. We remark that these choices can also be used with the sweeping method and an initial value solver that detects a “stopping condition” defined by the level set of a function. The slow manifolds can be extended by choosing cross-sections  $\Sigma$  orthogonal to  $F$  at points that lie beyond the folded node. Figures 23 (a) and 28 (c) give examples of such visualizations; see also [24, 25, 27].

As with all continuation, an important issue is to find a first solution. When continuing solutions of a boundary value problem, explicit solutions may be known from which such a first solution may be constructed; see [25] for an example. However, in general no explicit solution is known and a first solution must be found in a different way. We use a homotopy method to generate an initial orbit segment; the main idea is to continue intermediate orbit segments via two auxiliary BVPs — the first to obtain an orbit segment from a point on the fold curve  $F$  to the section, and the second to move the end point on  $F$  along the critical manifold to a suitable distance from  $F$ ; see [24] for details. We now illustrate this method with the Koper model [85], which is a particular version of the Bonhoeffer-Van der Pol system. The equations of the Koper model are

$$\begin{cases} \varepsilon_1 \dot{x} &= k y - x^3 + 3x - \lambda, \\ \dot{y} &= x - 2y + z, \\ \dot{z} &= \varepsilon_2 (y - z), \end{cases} \quad (103)$$

where  $\lambda$  and  $k$  are parameters. Koper studied this three-dimensional idealized model of chemical reactions with MMOs. We use the parameters  $(\varepsilon_1, \varepsilon_2, \lambda, k) = (0.1, 1, 7, -10)$ ; note that  $\lambda > 0$  as in [85]. There is a folded node in this model, which organizes the SAOs in some of the observed MMOs; in original coordinates it is at

$$\mathbf{p}_{\text{fn}} = \left( -1, \frac{2 + \lambda}{k}, \frac{2\lambda + 4 + k}{k} \right) = (-1, -0.9, -0.8). \quad (104)$$

We compute  $S_{\varepsilon_1}^a$  and  $S_{\varepsilon_1}^r$  as solutions to the BVPs given by (102), where  $\mathbf{g}$  is defined as the right-hand side of the Koper model. As boundary conditions, we use the same section  $\Sigma$  for both  $S_{\varepsilon_1}^a$  and  $S_{\varepsilon_1}^r$  with respective lines  $L = L^a$  and  $L = L^r$  as follows

$$\Sigma_{\text{fn}} := \{(x, y, z) \in \mathbb{R}^3 \mid z = -0.8\}, \quad (105)$$

$$L^a := S \cap \{x = -1.5\}, \quad (106)$$

$$L^r := S \cap \{x = -0.2\}. \quad (107)$$

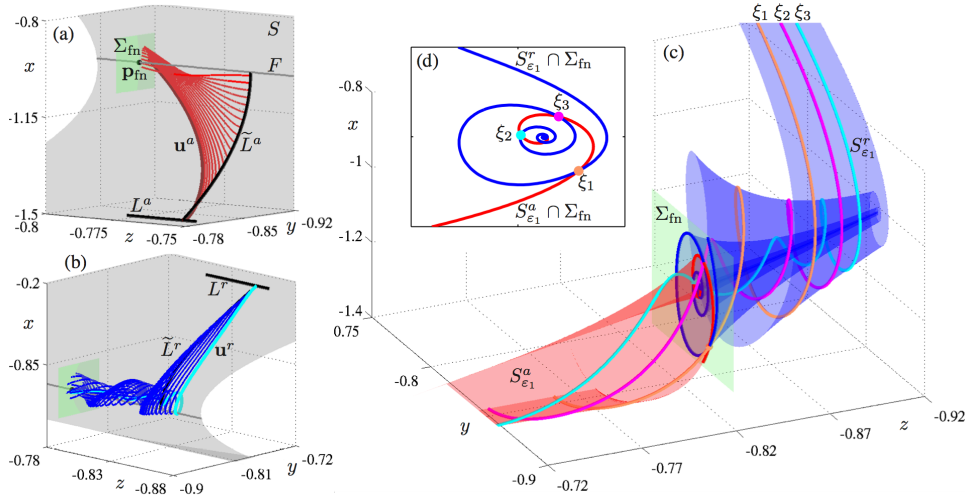


Figure 28: Computation of the slow manifolds  $S_{\varepsilon_1}^a$  and  $S_{\varepsilon_1}^r$  of the Koper model (103) with  $(\varepsilon_1, \varepsilon_2, \lambda, k) = (0.1, 1, 7, -10)$ . Panel (a) shows a homotopy family of red orbit segments that connect the section  $\Sigma_{\text{fn}}$  with the critical manifold  $S$  (grey). The first (upper-most) curve in the family was computed by a separate homotopy that found an orbit segment ending along  $F$  at some suitable distance from  $\mathbf{p}_{\text{fn}}$ . The second homotopy step swept out the family of red curves, terminating with the last (lowest, darker red) orbit segment whose endpoint lies on the curve  $L^a$ . Panel (b) shows a similar homotopy family of orbit segments (blue) connecting  $\Sigma_{\text{fn}}$  with the repelling sheet of the critical manifold. The final (right-most, cyan) orbit segment starts at  $L^r$ . Panel (c) shows  $S_{\varepsilon_1}^a$  and  $S_{\varepsilon_1}^r$  together with three secondary canards  $\xi_1$ ,  $\xi_2$  and  $\xi_3$ . Panel (d) shows the intersection curves of  $S_{\varepsilon_1}^a$  and  $S_{\varepsilon_1}^r$  in  $\Sigma_{\text{fn}}$  that are used to detect canard orbits.

Figure 28 shows the result of the computations. We find a first orbit segment on  $S_{\varepsilon_1}^a$  using two homotopy steps; this is illustrated in Fig. 28(a). Starting from the trivial solution  $\mathbf{u} = \{\mathbf{p}_{\text{fn}} \mid 0 \leq t \leq 1\}$ , with total integration time  $T = 0$ , we continue the family of orbit segments that solves (103) subject to  $\mathbf{u}(1) \in \Sigma_{\text{fn}}$  and  $\mathbf{u}(0) \in F$ . We stopped the computation, detected by a user-defined function in AUTO, as soon as

$$\mathbf{u}(0) \in \tilde{\Sigma}^a := \{(x, y, z) \in \mathbb{R}^3 \mid z = -0.76\}.$$

The orbit segment with its end point on  $F$  in Fig. 28(a) is this last computed solution of the family. The second step of the homotopy moves  $\mathbf{u}(0) \in S$  away from  $F$  (approximately) parallel to  $\Sigma$ , that is, we next continue the family of orbit segments that solves (103) subject to  $\mathbf{u}(1) \in \Sigma_{\text{fn}}$  and  $\mathbf{u}(0) \in \tilde{L}^a = S \cap \tilde{\Sigma}^a$ . The continuation stops when  $L^a$  is reached, which is again detected by a user-defined function in AUTO. A selection of orbit segments in this family are shown in Fig. 28(a) (red curves); only the last orbit segment  $\mathbf{u}^a$  (lowest, dark red) lies on  $S_{\varepsilon_1}^a$  to good approximation; it is the one from which the manifold computation is started. A similar computation was done to obtain a first orbit segment on  $S_{\varepsilon_1}^r$ , where we use the intermediate section  $\tilde{\Sigma}^r := \{z = -0.87\}$ ; this is illustrated in Fig. 28(b), where the orbit segment  $\mathbf{u}^r$  (cyan) serves as a first solution on  $S_{\varepsilon_1}^r$ .

Once the first orbit segments  $\mathbf{u}^a$  and  $\mathbf{u}^r$  have been found we start the continuation of (102) with (105) and (106) for the attracting slow manifold  $S_{\varepsilon_1}^a$  and with (105) and (107) for the repelling slow manifold  $S_{\varepsilon_1}^r$ . The result is presented in Fig. 28(c), and the intersection curves of  $S_{\varepsilon_1}^a$  and  $S_{\varepsilon_1}^r$  with  $\Sigma_{\text{fn}}$  are shown in Fig. 28(d). The transverse intersection points of  $S_{\varepsilon_1}^a \cap \Sigma_{\text{fn}}$  and  $S_{\varepsilon_1}^r \cap \Sigma_{\text{fn}}$  in panel (d) correspond to secondary canard orbits; the three-dimensional view in panel (c) shows three of these, labeled  $\xi_1$ ,  $\xi_2$  and  $\xi_3$ .

### 3.2.2 Finding and following canard orbits

Maximal canards near a folded node are transverse intersection curves of the two-dimensional attracting and repelling slow manifolds  $S_{\varepsilon}^a$  and  $S_{\varepsilon}^r$ . We briefly discuss here how to detect the canard



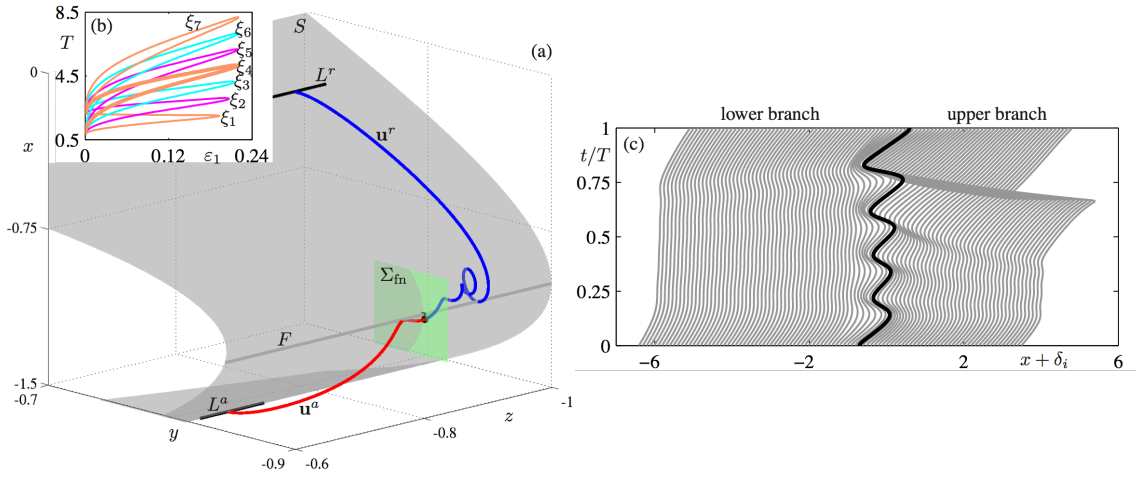


Figure 29: Continuation of secondary canards of the Koper model (103) with  $(\varepsilon_2, \lambda, k) = (1, 7, -10)$  starting from  $\varepsilon_1 = 0.1$ . Panel (a) shows the canard orbit  $\xi_4$  represented by the concatenation  $\mathbf{u}^c$  of two orbit segments  $\mathbf{u}^a$  and  $\mathbf{u}^r$  that match up in  $\Sigma_{\text{fn}}$ . Panel (b) shows the continuation of the canard orbits  $\xi_1$ – $\xi_7$  in  $\varepsilon_1$ ; plotted as total integration time  $T$  versus  $\varepsilon_1$ . Panel (c) shows a two-dimensional “waterfall diagram” of the time profiles of the fast variable  $x$  (subject to an offset  $\delta_i$ ) of computed orbit segments along the branch  $\xi_4$ . The bold black curve in panel (c) is the canard orbit  $\xi_4$  at the fold point of the (boldfaced) branch in panel (b).

orbits and subsequently continue them in a system parameter; see also [24, 25, 27]. To represent a maximal canard we must compute  $S_\varepsilon^a$  and  $S_\varepsilon^r$  using a common cross-section  $\Sigma$  of the fold curve at or near the folded node. The common cross-section allows us to obtain a representation of the canard orbit as the concatenation  $\mathbf{u}^c$  of an orbit segment  $\mathbf{u}^a \subset S_\varepsilon^a$  (with associated total integration time  $T^a$ ) with an orbit segment  $\mathbf{u}^r \subset S_\varepsilon^r$  (with associated total integration time  $T^r$ ), where  $\mathbf{u}^a$  and  $\mathbf{u}^r$  are chosen such that  $\mathbf{u}^a \cap \Sigma = \mathbf{u}^r \cap \Sigma$ . The concatenated orbit  $\mathbf{u}^c$  located with this method can be continued in a system parameter without the need to recompute the slow manifolds at each step. Recall that AUTO always scales boundary value problems to the time interval  $[0, 1]$ , so we rescale time on  $\mathbf{u}^c$  appropriately and set  $T = T^a + T^r$  in (102). We can then start the continuation (in a system parameter) subject to the boundary conditions

$$\mathbf{u}^c(0) \in L^a, \quad (108)$$

$$\mathbf{u}^c(1) \in L^r, \quad (109)$$

which determine  $\mathbf{u}^c$  as an isolated solution. In fact, such a continuation typically starts already provided that  $\mathbf{u}^a \cap \Sigma \approx \mathbf{u}^r \cap \Sigma$ ; any small gap in  $\Sigma$  is forced to close by the first Newton step. These two boundary conditions (108) and (109) force the orbit segment  $\mathbf{u}^c$  to stay very close to the attracting sheet of the critical manifold  $S$  until near the fold curve  $F$ , and then stay close to the repelling sheet of  $S$  up to  $L^r$ .

Figure 29 illustrates canard continuation with the Koper model (103), where we used  $\varepsilon_1$  as the second free parameter (together with  $T$ ) and kept  $(\varepsilon_2, \lambda, k) = (1, 7, -10)$  fixed. Figure 29(a) shows the two orbit segments  $\mathbf{u}^a$  and  $\mathbf{u}^r$  with (almost) equal end points in the section  $\Sigma = \Sigma_{\text{fn}}$ ; they have been detected as a good approximation of the maximal secondary canard orbit  $\xi_4$ , which is then represented by the concatenated orbit  $\mathbf{u}^c$ . We continued  $\xi_4$ , along with six other maximal secondary canards, for increasing and decreasing  $\varepsilon_1$ ; see also Fig. 28. Figure 29(b) shows these seven branches, labeled  $\xi_1$ – $\xi_7$ ; here, the vertical axis shows the total integration time  $T$  because it clearly distinguishes the branches. When  $\xi_1$ – $\xi_7$  are continued in the direction of increasing  $\varepsilon_1$ , a fold in  $\varepsilon_1$  is detected for each branch; we have already seen this in Section 3.1.2 and it has also been observed in other systems [27]. Figure 29(c) is a “waterfall diagram” that shows how the maximal secondary canard orbit  $\xi_4$  evolves along the branch as  $\varepsilon_1$  is varied; specifically, the time profile of the fast variable  $x$  of consecutively computed orbit segments along the branch  $\xi_4$  are plotted with a suitable off-set  $\delta_i$ . The orbit segment that corresponds to the fold of  $\xi_4$  is highlighted in bold black. Observe

that the orbit segments to the left of the fold have four SAOs, whereas past the fold there are only three SAOs followed by a fast segment. Hence the canard orbits past the fold are no longer maximal canards; see also Section 3.1.2.

### 3.3 EXTENDING THE INFLECTION-LINE METHOD TO FOLDED-NODE SYSTEMS

#### 3.3.0.1 The minimal folded node system as a planar non-autonomous system

Here we propose a first attempt towards extending the inflection-line method revisited using singularity theory (as exposed in Section 2.2.1.2), a minimal three-dimensional system displaying a folded node. We consider the minimal folded node type system

$$x' = -y + x^2 - x^3 \quad (110)$$

$$y' = \varepsilon(z + x) \quad (111)$$

$$z' = \varepsilon\mu, \quad (112)$$

with  $0 < \varepsilon, \mu \ll 1$ . System (110)–(112) is actually of dimension “two and a half” in the sense that it can be written as a planar *non-autonomous* system as below

$$x' = -y + x^2 - x^3 \quad (113)$$

$$y' = \varepsilon(\varepsilon\mu t + z_0) \quad (114)$$

Now we can try to apply the inflection line method to the non-autonomous planar system (113)–(114). We first write the trajectory equation

$$\frac{dy}{dx} = \frac{\varepsilon(\varepsilon\mu t + z_0 + x)}{-y + x^2 - x^3}, \quad (115)$$

which we can re-write in the form

$$(-y + x^2 - x^3) \frac{dy}{dx} - \varepsilon(\varepsilon\mu t + z_0) - \varepsilon x = 0. \quad (116)$$

Equation (116) can be differentiated with respect to  $x$  with the inflection condition  $y''(x) = 0$  being plugged in; the difference with the usual case is the presence of  $t$  which must then also be differentiated with respect to  $x$ , giving

$$-\left(\frac{dy}{dx}\right)^2 + (2x - 3x^2) \frac{dy}{dx} - \varepsilon^2 \mu \frac{dt}{dx} - \varepsilon = 0, \quad (117)$$

with  $\frac{dy}{dx} = \frac{\varepsilon(\varepsilon\mu t + z_0 + x)}{h}$  and  $\frac{dt}{dx} = \frac{1}{h}$ , and with  $h = -y + x^2 - x^3$ . Therefore, equation (117) becomes

$$-\frac{\varepsilon^2(\varepsilon\mu t + z_0 + x)^2}{h^2} + (2x - 3x^2) \frac{\varepsilon(\varepsilon\mu t + z_0 + x)}{h} - \varepsilon^2 \mu \frac{1}{h} - \varepsilon = 0. \quad (118)$$

Rearranging and simplifying gives, we finally obtain the  $t$ -dependent quadratic inflection equation

$$h^2 + (\varepsilon\mu - (2x - 3x^2)(\varepsilon\mu t + z_0 + x)) h + \varepsilon(\varepsilon\mu t + z_0 + x)^2 = 0. \quad (119)$$

The general solution of equation (119) is given by

$$h_{\pm}(x) = \frac{1}{2} \left( -\varepsilon\mu + (2x - 3x^2)(\varepsilon\mu t + z_0 + x) \pm \sqrt{\Delta} \right), \quad (120)$$

with

$$\Delta = [\varepsilon\mu - (2x - 3x^2)(\varepsilon\mu t + z_0 + x)]^2 - 4\varepsilon(\varepsilon\mu t + z_0 + x)^2. \quad (121)$$



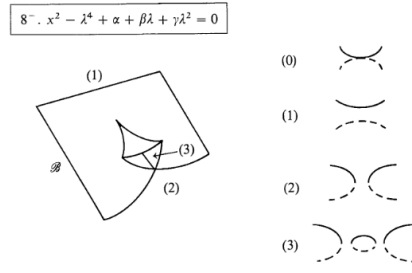


Figure 30: Figure extracted from Golubitsky and Schaeffer [58], page 208.

### 3.3.0.2 Extracting information about $\varepsilon$ and $\mu$ from the inflection line

In Section 2.2.1.2, we could characterise their topological shapes by rewriting the inflection equation as a *bifurcation problem with a distinguished parameter* and using the classification provided in [58]. One can use the same idea for the inflection equation associated with folded node systems. To get more information about the relationship between inflection sets and the dynamics near a folded node, it is useful to evaluate the inflection equation close to the folded node and for a “time frame” corresponding to it, that is, for  $|x - 2/3| < \varepsilon$  and for  $\varepsilon\mu t + z_0 = z_{\text{fn}} = -2/3$ , where  $z_{\text{fn}}$  is the  $z$ -coordinate of the folded node. In these conditions, the inflection equation (119) gets the following simplified form

$$h^2 + \left[ \varepsilon\mu - (2x - 3x^2) \left( -\frac{2}{3} + x \right) \right] h + \varepsilon \left( -\frac{2}{3} + x \right)^2 = 0. \quad (122)$$

Then, completing the square in (122) yields

$$\bar{h}^2 - \frac{1}{4} \left[ \varepsilon\mu - (2x - 3x^2) \left( -\frac{2}{3} + x \right) \right]^2 + \varepsilon \left( -\frac{2}{3} + x \right)^2 = 0, \quad (123)$$

with

$$\bar{h} = h + \frac{1}{2} \left[ \varepsilon\mu - (2x - 3x^2) \left( -\frac{2}{3} + x \right) \right]. \quad (124)$$

This can be conveniently rewritten in the following way

$$\begin{aligned} \bar{h}^2 - \left( \sqrt{\frac{\varepsilon\mu}{2}} \right)^4 + \left( \left( -\frac{2}{3} + x \right) \left( \varepsilon - \frac{1}{4}(2x - 3x^2)^2 \right) \right. \\ \left. + \left( \sqrt{\frac{\varepsilon\mu}{2}} \right)^2 (2x - 3x^2) \left( -\frac{2}{3} + x \right) \right) = 0. \end{aligned} \quad (125)$$

Now equation (125) can be recasted as a bifurcation problem with a distinguished parameter, and it can be written in the form of case  $8^-$  on page 208 [58], that is

$$X^2 - \lambda^4 + \alpha + \beta\lambda + \gamma\lambda^2, \quad (126)$$

with

$$X = \bar{h}, \quad (127)$$

$$\lambda = \sqrt{\frac{\varepsilon\mu}{2}}, \quad (128)$$

$$\alpha = \left( \left( -\frac{2}{3} + x \right) \left( \varepsilon - \frac{1}{4}(2x - 3x^2)^2 \right) \right), \quad (129)$$

$$\beta = 0, \quad (130)$$

$$\gamma = (2x - 3x^2) \left( -\frac{2}{3} + x \right). \quad (131)$$

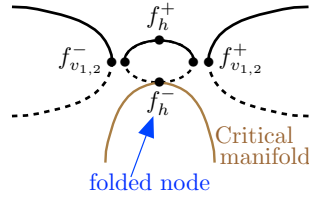


Figure 31: Configuration of the inflection set for the folded node minimal system (110)–(112), evaluated at the time frame that corresponds to the folded node, that is, for  $\mu > 0$ . The coordinates of the fold points  $f_{v,h}^\pm$  can be estimated using basic expansions in  $\mu$ .

The shape of the solution to equation (126) is shown on Fig. 30. This shows that when  $\mu > 0$ , that is, in the folded node case, an additional closed component of the inflection line exists, contrary to the planar case where only one point of this “bubble” exists (the equilibrium point). We can now show, using simple asymptotic expansions in  $\mu$  of the solutions to the equation  $\Delta = 0$ , where  $\Delta$  is the discriminant of the (quadratic) inflection equation, that the maximal diameter of this small ellipse is of order  $\sqrt{\varepsilon}\mu$ .

Indeed, the fold points of the inflection set with respect to the vertical axis correspond to zeroes of the discriminant of the inflection equation, that is, the solutions to equation (121). In the time frame corresponding to the folded node, the equation  $\Delta = 0$  reduces to

$$(2x - 3x^2) \left( -\frac{2}{3} + x \right) - \varepsilon\mu = \pm 2\sqrt{\varepsilon} \left( -\frac{2}{3} + x \right). \quad (132)$$

Expanding the solution to first order in  $\mu$ , that is, writing  $x = x_0 + x_1\mu + o(\mu^2)$ , gives

$$\begin{aligned} & (2x_0 - 3x_0^2) \left( -\frac{2}{3} + x_0 \right) \\ & + x_1 \left( 2 \left( -\frac{2}{3} + x_0 \right) + 3(2x_0 - 3x_0^2) \right) \mu - \varepsilon\mu + o(\mu^2) \\ & = \pm 2\sqrt{\varepsilon} \left( -\frac{2}{3} + x_0 + x_1\mu \right) + o(\mu^2). \end{aligned} \quad (133)$$

Now collecting the terms of same order in  $\mu$  on both sides of equation (133) provides the following expressions for  $x_0$  and  $x_1$  in terms of  $\varepsilon$

$$(2x_0 - 3x_0^2) \left( -\frac{2}{3} + x_0 \right) = \pm 2\sqrt{\varepsilon} \left( -\frac{2}{3} + x_0 \right), \quad (134)$$

$$x_1 \left( 2 \left( -\frac{2}{3} + x_0 \right) + 3(2x_0 - 3x_0^2) \right) - \varepsilon = \pm 2\sqrt{\varepsilon}x_1. \quad (135)$$

Equation (134) is the unperturbed equation, that is, for  $\mu = 0$ , and its solutions are

$$x_0 = \frac{2}{3}, \quad x_0 = \frac{1}{3} \left( 1 \pm \sqrt{1 \mp 6\sqrt{\varepsilon}} \right). \quad (136)$$

Evaluating equation (135) for these values of  $x_0$  gives

$$x_1 = \pm \frac{\sqrt{\varepsilon}}{2}. \quad (137)$$

Finally, the solutions to the equation  $\Delta = 0$  evaluated at the time-frame corresponding to the folded node are

$$x = x_0 \pm \frac{\sqrt{\varepsilon}}{2}\mu + o(\mu^2), \quad (138)$$

where  $x_0$  is given by the formulas (136). This gives the coordinates of the vertical fold points,  $f_v^\pm$ , of the small ellipse component of the inflection set; see Fig. 31. From the above analysis we can deduce that the  $x$ -coordinates of the vertical fold points  $f_v^\pm$  are given by

$$f_{v,x}^\pm = \frac{2}{3} \pm \frac{\sqrt{\varepsilon}}{2} \mu + o(\mu^2). \quad (139)$$

Furthermore, the horizontal fold points  $f_h^\pm$  have an  $x$ -coordinate equal to  $2/3$  and their  $y$ -coordinates are given by  $4/27 + \varepsilon\mu$  and  $4/27$ , respectively. This is easily obtained by evaluating the inflection equation corresponding the folded node time frame at  $x = 2/3$ , which reduces to

$$h^2 + \varepsilon\mu h = 0, \quad (140)$$

whose solutions are  $h = 0$  — that is, the upper fold point of the critical manifold  $C^0$ , see Fig. 31 below — and  $h = -\varepsilon\mu$ . Consequently, we have

$$f_h^- = \left( \frac{2}{3}, \frac{4}{27} \right), \quad (141)$$

$$f_h^+ = \left( \frac{2}{3}, \frac{4}{27} + \varepsilon\mu \right). \quad (142)$$

This analysis reveals that one can extract information about  $\mu$  and  $\varepsilon$  by the sole knowledge of the inflection set; moreover, both of these key parameters can be independently. Indeed, although the above formulas contain the factor  $\varepsilon\mu$  as a block, one can recover  $\varepsilon$  from the distance between the fold points of the inflection set near the lower fold of the critical manifold, which falls out of the analysis already done in the planar (canard explosion) case.

Elements of the material presented in this chapter have been published in [20, 29]. Our contribution concerns the re-interpretation of canard-induced spike-adding transitions in square-wave bursters in terms of classical canard explosions; this work is presented in Section 4.2, just after a brief recall of bursting oscillations in a general context in the first section. The last section of this chapter is devoted to torus canard solutions, which have been only recently discovered in “one slow / two fast” systems and are still far from understood from a theoretical viewpoint. We have analysed numerically the bifurcation structure of a number of neuronal models featuring bursting oscillations and given evidence that they undergo torus canard transitions when passing, upon parameter variation, from the bursting to the spiking regime; this work is presented in the last section, where we only focus on one such example, namely, the Hindmarsh-Rose model.

#### 4.1 INTRODUCTION TO BURSTING

When going from two to three dimensions in slow-fast vector fields, one may add a second fast variable instead of a second slow variable. In that case, the fast dynamics can now sustain periodic dynamics and this can give rise, in the full three-dimensional system, to complex oscillations referred to as *bursting oscillations*. They are characterised by an alternation between slow phases referred to as silent or quiescent, and fast oscillatory phases or burst. Such systems are then called *bursters*. Bursters have long been studied using a slow-fast dynamics formalism and then classified by a number of different means, including the bifurcations of the fast subsystem in which the burst events are initiated and terminated [130, 76] and by an unfolding theory approach to singularities in the fast subsystem [13, 59]. This phenomenon has been studied in particular to understand complex electrophysiological data. Indeed, bursting is one of the most commonly observed behaviour in cellular electrical and secretory activity, where bursts correspond to groups of spike; see e.g. [21, 86, 14].

Among the many known bursters are three main classes introduced by J. Rinzel [131]. First, *square-wave bursting*, where the burst phase is initiated by a saddle-node bifurcation of equilibria and ends in a homoclinic bifurcation. It is a “two fast/one slow” system for which the critical manifold is a cubic curve. The Hindmarsh-Rose (HR) system [70, 71] is one of the simplest square-wave bursters since it corresponds to a (smooth) polynomial vector field (equations (146)–(148) below). In this model, bursting solutions arise through a supercritical Hopf bifurcation followed by a canard explosion; then a canard-mediated spike-adding transition is responsible for bursting orbits with more and more fast oscillations in the burst. This spike-adding phenomenon is well-known and has been investigated, for instance, in the Morris-Lecar-Terman model [65, 146] and in the Hindmarsh-Rose model [118]; see Section 4.2 below. The main characteristic features of time series of square-wave neuronal bursters are a low-voltage quiescent phase and the frequency of spikes decreasing at the end of the burst.

The second class is that of *elliptic bursters*, where the burst initiates through a subcritical Hopf bifurcation in the fast subsystem and terminates because of a saddle-node bifurcation of limit cycles. Examples of neuronal elliptic bursters include the FitzHugh-Rinzel model; for more details, see e.g. [75, 77]. Elliptic bursting time series are characterised by small oscillations during quiescence and the elliptic-shaped envelop of fast oscillations (although not always observed).

Finally, *parabolic bursting* is the third class introduced by Rinzel. It stands alone by the necessity of two slow processes, hence theoretically requiring (at least) two slow and two fast variables; Sec-

tion 5.2 is dedicated to this class of burster and the role of canards in organising the number of spikes per burst in such systems.

One of the main theoretical tools of slow-fast analysis of bursters, which will also be employed herein, is the dissection method, introduced by Rinzel in [130]. The idea is to freeze the dynamics of the slow variables  $\mathbf{y}$  by setting  $\varepsilon = 0$  in the following “fast-time” parametrisation of a generic slow-fast system (with explicit timescale separation):

$$\begin{aligned}\mathbf{x}' &= \mathbf{f}(\mathbf{x}, \mathbf{y}), \\ \mathbf{y}' &= \varepsilon \mathbf{g}(\mathbf{x}, \mathbf{y}),\end{aligned}\tag{143}$$

where  $(\mathbf{x}, \mathbf{y}) \in \mathbb{R}^2 \times \mathbb{R}$  for square-wave and elliptic bursters, whereas  $\mathbf{y} \in \mathbb{R}^2$  in the case of parabolic bursters. The slow variables are therefore considered as parameters entering the remaining differential equations for the fast variables  $\mathbf{x}$ ; the limiting problem is the fast subsystem. In this setting, the bifurcation diagram of the fast subsystem with respect to the original slow variables (seen as parameters), reveals the dynamical transitions between slow and fast phases of activity in the full (three or four-dimensional) system. Specifically, these transitions are between the quiescent phase, where the system tracks quasi-statically a branch of stable equilibria of the fast subsystem, and the burst (or active) phase, where the system follows a family of stable limit cycles of the fast subsystem. A very powerful graphical way to represent the slow-fast dissection method is to trace in the same phase-space projection a solution of the full system and the various bifurcation branches of the fast subsystem; see already Figs. 33 and 34 for an example in a square-wave burster, and Fig. 42 for an example in a parabolic burster. This technique is straightforward for bursters with only one slow variable (for instance, square-wave or elliptic bursters) and it is used as a standard tool for the study of such systems. However, the applicability of the method is non-trivial for parabolic bursters since it has two slow variables. A possible strategy to deal with the two slow variables is to first vary one of them (seen as a parameter), compute the associated bifurcation diagram, and then compute curves of codimension-one bifurcation points (saddle-node, Hopf, homoclinic) of this diagram when both variables are allowed to vary. In other words, in the case of parabolic bursters, the branches of attractors (steady-states, limit cycles) of the fast subsystem are two-dimensional (parametrised by the two slow variables), therefore one can compute these surfaces as one-parameter families of curves obtained when varying only one of the two variables as a parameter; see Section 5.2.

## 4.2 SPIKE-ADDING CANARD EXPLOSION IN SQUARE-WAVE BURSTERS

In this section, we examine the transition from a stable equilibrium (quiescence) to stable square-wave bursting in the Hindmarsh-Rose system (1)-(3) for a sequence of fixed values of the parameter  $I$ . This transition occurs via the well-known mechanism of spike-adding, see [65, 115, 118, 149], first analyzed in the Morris-Lecar-Terman model, see [146]. For each  $N = 0, 1, 2, \dots$ , there is an exponentially narrow interval of parameter values  $I$  over which the system exhibits a continuous transition from periodic solutions with  $N$  spikes to periodic solutions with  $N + 1$  spikes. Each periodic solution in the transition sequence is referred to as a canard of limit cycle type, or limit cycle canard, since each periodic orbit has alternating segments near attracting and repelling branches of fixed points interspersed with fast jumps from the latter to the former that reinitiate the cycle. Each transition sequence is referred to as a canard explosion, and the transitions for  $N = 0$  and  $N = 1$  are illustrated in Figs. 33 and 34, respectively.

A detailed description of the transition for  $N = 0$  from quiescence to a limit cycle with one large-amplitude spike is as follows. At  $I \approx 1.413$ , there is a Hopf bifurcation of the full system (146)–(148). This Hopf bifurcation induces the canard explosion, in exact analogy to that in the planar van der Pol and FitzHugh-Nagumo equations. For  $I = 1.3278138093$ , the HR system (146)–(148) exhibits a small-amplitude limit cycle canard without any spike, also known as a headless canard, see Fig. 33(a). As  $I$  is decreased, see Fig. 33(b), the limit cycle grows in amplitude until, at  $I = 1.3278138026$ , it reaches the far right fold near  $z = 2.328$ , see Fig. 33(c). This is the maximal headless canard, and as in the

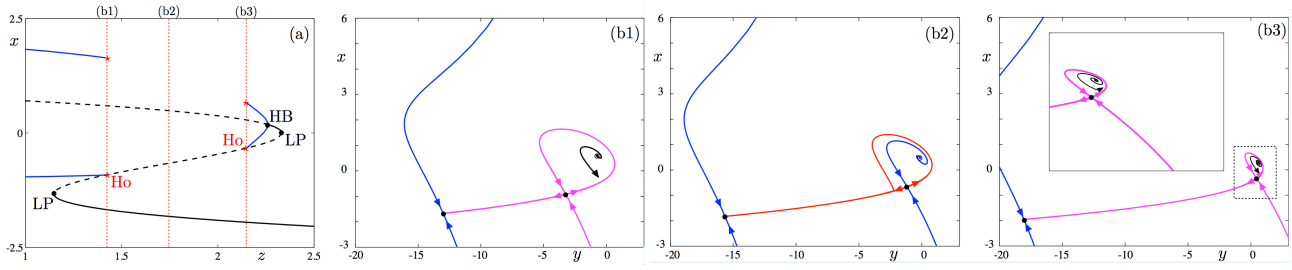


Figure 32: Panel (a) shows the bifurcation diagram of the fast subsystem of the Hindmarsh-Rose burster i.e. equations (146)–(147), with  $z$  acting as a parameter. All parameter values are taken to be the classical ones (from [71]) and  $I$  is fixed at the value corresponding to the canard explosion taking place in the full system and displayed in Fig. 33, that is,  $I = 1.3278138$ . Panels (b1)–(b3) show snapshots of the phase portrait of the fast system for three different values of  $z$ , namely  $z = 1.449$  (lower homoclinic),  $z = 1.75$  and  $z = 2.180$  (upper homoclinic). For each value of  $z$  in between the lower and upper homoclinics, the unstable manifold of the saddle returns to a neighbourhood of the saddle and gives the leading-order location of the spike in the full system.

canonical planar systems with canards, such as the van der Pol and FitzHugh-Nagumo equations, it occurs precisely when the persistent attracting and repelling slow manifolds near the branches of equilibria coincide. Although slow manifolds are in general not unique, there are unique analytic slow manifolds near the attracting branches of the critical manifold<sup>1</sup>. Besides, one can choose a repelling slow manifold that starts  $O(\sqrt{\epsilon})$  near the canard point and continues to  $O(\epsilon^{1/3})$  close to the jump point following the repelling branch; the power of  $\epsilon$  is dictated by the choice of the blow-up transformation needed to analyse the underlying singularity: canard point or fold point. Therefore, one can study the intersection between the attracting and the repelling slow manifolds; see [92] for details.

Further along the branch, the limit cycle continues to have long segments near both the attracting and the repelling branches of the critical manifold, but now at the end of the segment near the repelling branch there is a brief segment of small oscillations, see Figs. 33(d) and 33(e), since the orbit now jumps from the critical manifold up to the branch of attracting periodic orbits, instead of back down to the branch of the critical manifold corresponding to attracting fixed points of the fast system. The attracting slow manifold now lies above the repelling slow manifold so that solutions must jump up to the branch of attracting periodic orbits. Even further along the branch, the up-jump occurs near the homoclinic orbit near  $z = 2.180$ , and the oscillations disappear, see Fig. 33(f). There is a long segment near the branch of repelling fixed points again, so that the canard cycles in this range have two canard segments, with the spike in between them.

The second canard segment disappears as we move yet further along the branch, see Fig. 33(g). Then, toward the end of the canard explosion, the location of the spike shifts downward in  $z$ , see Fig. 5(h), until the spike occurs near the lower homoclinic ( $z = 1.449$ ). This completes the description of how the first large-amplitude spike is created in a continuous manner as the parameter  $I$  is changed, so that continuous dependence of solutions on parameters is respected, and it completes the description of the first cycle of spike-adding, for  $N = 0$ .

The continuous transition for  $N = 1$ , from a limit cycle canard with one spike to a limit cycle canard with two spikes, occurs in a completely analogous fashion, see Fig. 34. During this second canard explosion, the first spike remains near  $z = 1.449$ . The sequence in which the second spike is created is precisely the same as that in which the first spike was created in Fig. 33 above. Moreover, we refer to this as the knitting mechanism. One creates loops in knitting in a similar manner, by hooking

<sup>1</sup> These attracting branches stretch to infinity (while remaining strongly normally hyperbolic). This means that a typical technique of proving the existence of an invariant manifold (e.g. graph transform) can be applied without modifying the original vector field, by using test functions that stretch out to infinity. The slow manifolds obtained in this manner are analytic.

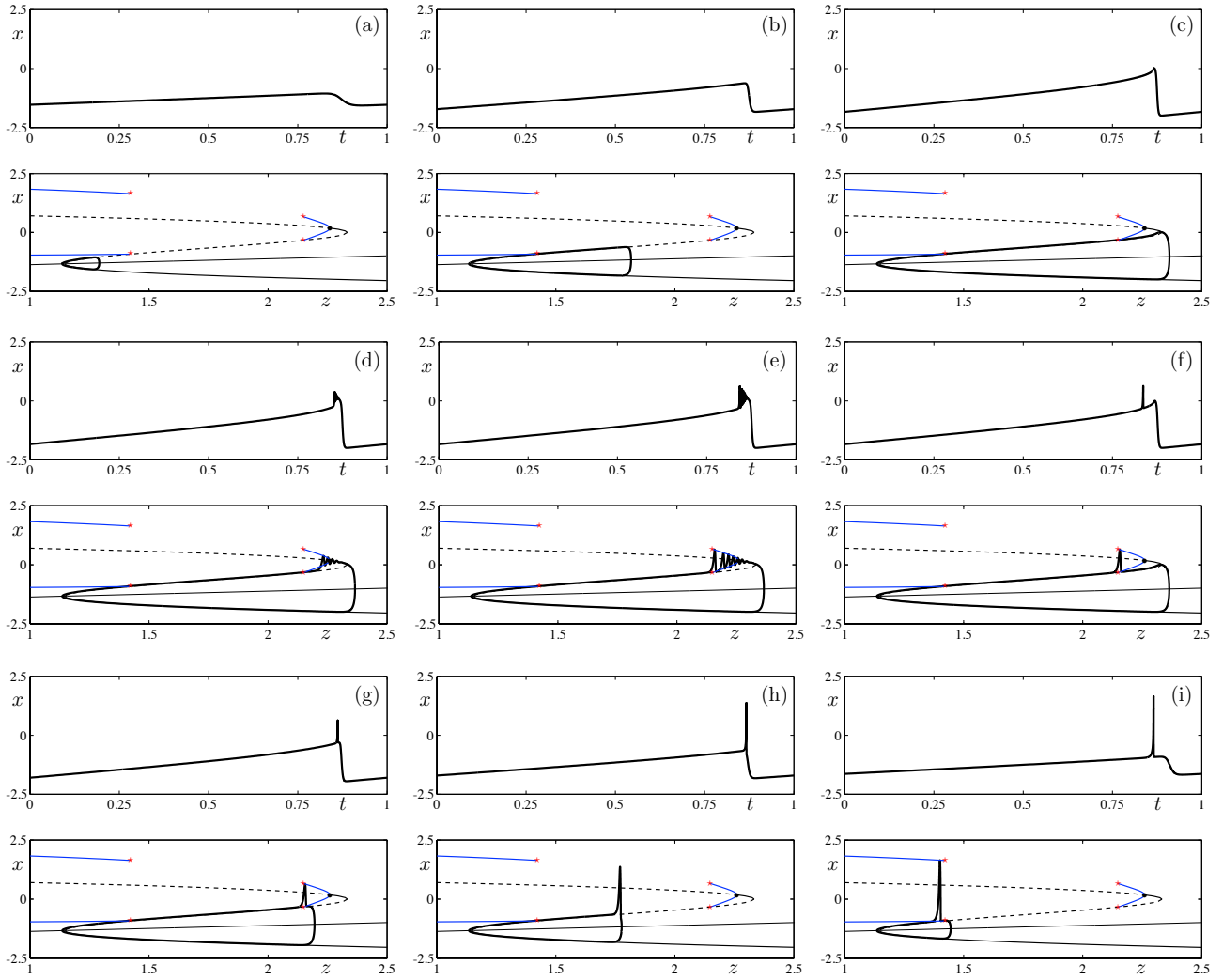


Figure 33: Spike-adding phenomenon: time series and phase portraits for the sequence of limit cycle canards observed in the transition from 0 to 1 spike in the Hindmarsh-Rose system (146)–(148). Parameter values are those given below equations (146)–(148), with  $\varepsilon = 5 \times 10^{-4}$  and  $I$  varying by an exponentially small amount around the value 1.3278138026. The top plot in each panel (a) to (i) shows the time series of the  $x$ -variable, with the period normalised to 1. The bottom plot shows the limit cycle canard in the phase plane  $(x, z)$ . In each frame, the behaviour of the trajectory at the end of the canard segment can be understood by looking at the phase portrait of the fast system (146)–(147) shown in Fig. 32.

the yarn over the tip of the needle (here the far right fold point) and then pulling it back along the needle.

It is worth observing also that, not only are the intervals of parameter values  $I$  in which each of these canard explosions for  $N = 0, 1, 2, \dots$  occur exponentially small in the limit as  $\varepsilon \rightarrow 0$ , but the critical values of  $I$ , at which the maximal headless ducks with  $N$  spikes occur, also approach each other as  $\varepsilon \rightarrow 0$ . Hence, the entire sequence of canard explosions occurs in an exponentially small interval of  $I$  values.

The dynamics of the canard limit cycles during each of these canard explosions is richer than that observed in planar systems such as the van der Pol and the FitzHugh-Nagumo equations because the repelling slow manifold is of saddle type here with two-dimensional stable and unstable manifolds. Indeed, according to the position of the orbit with respect to these manifolds, it will either follow the slow manifold along a canard segment or escape from it along a fast fiber; see [65] for details. The transition can be understood by invoking the *Exchange Lemma* [81].



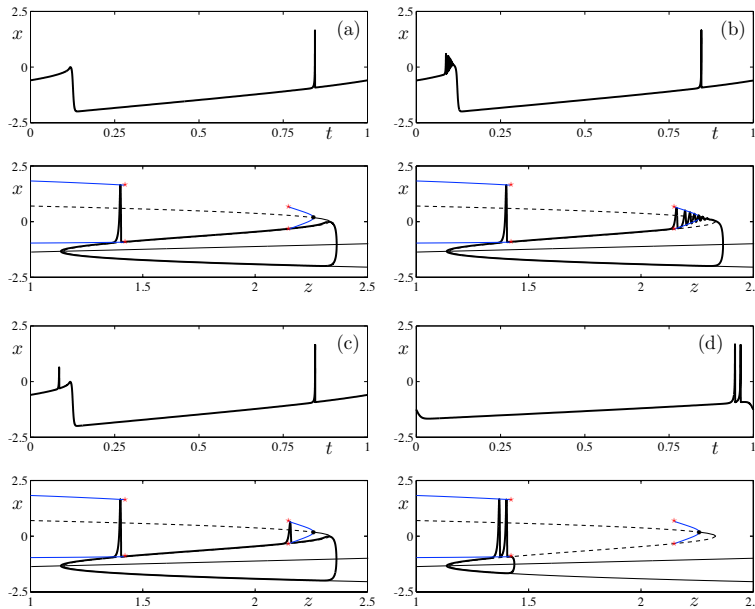


Figure 34: Spike-adding phenomenon: time series and phase plane projections for limit cycles along the transition from 1 spike to 2 spikes. The first spike, created during the previous spike-adding transition, remains in essentially the same place during the transition in which the second spike is generated. Along the explosion that leads to the addition of a second spike, the parameter  $I$  varies by an exponentially amount around the value 1.3317831217.

For parameter values of  $I$  when the spike is first created, see Figs. 33(f) and 34(c), the spike lies close to the (upper) homoclinic of the fast system. Then, further along the branch, the limit cycle canard still exhibits a spike, however there is no homoclinic orbit of the fast system nearby, see Fig. 32(b2). Nevertheless, in the full third-order system the one-dimensional repelling slow manifold has two-dimensional stable and unstable manifolds whose relative positions are responsible for the creation of the spike. These positions are given to leading order by the stable and unstable manifolds of the saddle repelling fixed point in the fast system, as shown in Fig. 32(b2).

Finally, to give further perspective on these results, we describe the classical square wave burster, as analyzed by Terman [146]. In general position, such a solution behaves as a relaxation oscillator near the lower fold and jumps to an attracting manifold corresponding to fast oscillations. Subsequently, the solution follows the manifold of stable fast oscillations until it terminates near the homoclinic orbit of the fast system, whereupon the solution jumps down to the stable branch of the slow manifold. As explained in [146], the number of fast oscillations is unbounded as  $\varepsilon \rightarrow 0$ . Although we are sure that this is folklore information, we have not found an asymptotic estimate of the number of such oscillations. We have derived such an estimate and included in the appendix of this Section. Our calculation implies that the number of such oscillations is  $O(1/\varepsilon)$ . It follows that changes of  $I$  by  $O(\varepsilon)$  may result in spike-adding transitions of the same kind as the latter part of our spike-adding canard explosion as well as the spike-adding transitions described by Terman [146] or Guckenheimer and Kuehn [65]. Such spike-adding transitions do not contain classical canard cycles but they contain canard segments corresponding to passage near the middle part of the critical manifold (see figure 3(b) of [146]) and they occur in exponentially small intervals of  $I$ . As pointed out by Terman [146] and further elaborated on by Guckenheimer and Kuehn [65], such transitions do not have to be monotonic in  $I$  and may lead to chaotic dynamics. Due to the computational complexity (a large number of spikes) we do not show an AUTO plot of such a transition.

**Remark:** Spike-adding canard explosions also occur at the level of homoclinic connections; see [97] for details.

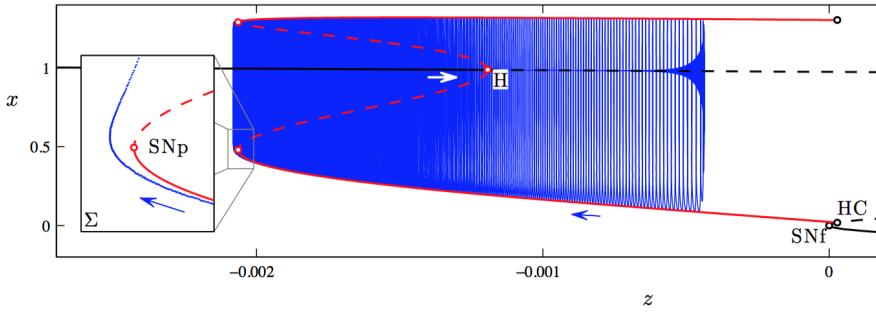


Figure 35: An example of sub-Hopf/fold cycle bursting in the HR system (144), with  $(b_1, s) = (-0.162, -1.95)$ . The other parameter values are given by (145). The bursting trajectory (blue curve) is plotted in projection onto the  $(z, x)$  phase space, along with the bifurcation diagram of the fast system at this value of  $s$ . The bifurcation diagram includes branches of fixed points and periodic orbits. The inset shows the Poincaré map of the bursting trajectory near  $\text{SNp}$ , also plotted in projection onto the  $(z, x)$  phase space. The Poincaré surface  $\Sigma \equiv \{(x, y, z) | 0 = sax^3 - sx^2 - y - bz\}$  is chosen so that the iterates correspond to local extrema in  $x$  of the trajectory.

### 4.3 FROM SPIKING TO BURSTING: TORUS CANARDS

Although the dynamics of spiking and bursting have been studied in detail, the mathematical mechanisms that govern transitions between neuronal states are only now beginning to be understood. The transition from spiking to bursting activity has been shown to involve different mechanisms including the blue sky catastrophe [140], period doubling [22], chaos [107, 147], and mixed-mode oscillations [158]. Recently, it has been proposed that the transition from spiking to bursting can also involve torus canards [7, 86]. In these models, limit cycles in the fast system terminate in a fold. However, these models exhibit unexpected behavior: the dynamics of the full system pass through the fold of limit cycles, but the burst's active phase does not terminate. Instead, the dynamics of the full system move through the fold of limit cycles and follow the branch of repelling limit cycles for some time, resulting in a torus canard.

In this section, we briefly show that torus canards arise naturally in computational neuronal models of multiple time scale type as the HR model. We refer to [20] for further examples; in particular, it is shown in [20] that torus canards arise in well-known neuronal models exhibiting three different classes of bursting: sub-Hopf/fold cycle bursting, circle/fold cycle bursting, and fold/fold cycle bursting.

**TORUS CANARDS IN THE HINDMARSH-ROSE SYSTEM.** We consider the following modified version of the Hindmarsh-Rose (HR) system [71] developed in Ref. [149]

$$\dot{x} = sax^3 - sx^2 - y - bz, \quad (144a)$$

$$\dot{y} = \phi(x^2 - y), \quad (144b)$$

$$\dot{z} = \varepsilon(sa_1x + b_1 - kz). \quad (144c)$$

The small parameter  $\varepsilon$  induces a separation of time scales, so that the voltage variable  $x$  and the gating variable  $y$  are fast and the recovery variable  $z$  is slow.

The HR model is known to exhibit rich dynamics, including square-wave bursting (a.k.a. plateau bursting) and pseudo-plateau bursting [149]. Here, we show that this model also exhibits sub-Hopf/fold cycle bursting (in which the active phase of the burst initiates in a subcritical Hopf bifurcation and terminates in a fold of limit cycles), and that torus canards occur precisely in the transition region from spiking to this type of bursting.

In this section, we first identify the parameter regimes in which the fast system of the HR model has a saddle-node of periodic orbits (Section 4.3) and in which the full HR model has a torus bifurcation (Section 4.3). Once these key ingredients are identified, we show (Section 4.3) that the

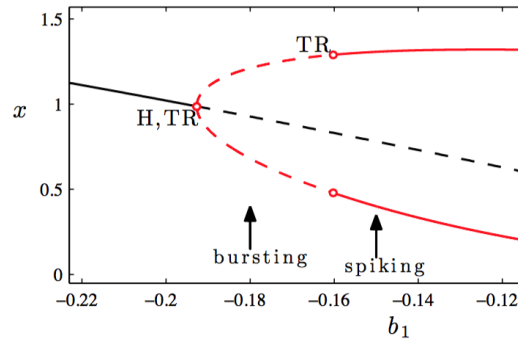


Figure 36: Bifurcation diagram of the HR system (144) at  $s = -1.95$ , including branches of fixed points (black curve) and periodic orbits (two red curves, indicating maximal and minimal values of  $x$  over the orbit). Solid/dashed curves indicate stable/unstable solutions. The torus bifurcation (labelled TR) at  $b_1 \simeq -0.1603$  is supercritical, leading to bursting for smaller values of  $b_1$ .

full HR model includes a torus canard explosion, and that it lies in the transition region between spiking and bursting.

We treat  $b_1$  as the primary control parameter, meaning that we examine the transition from spiking to bursting as  $b_1$  varies. We take  $s$  as a secondary control parameter, and examine how the transition from spiking to bursting behaves at different values of  $s$ . Except where otherwise noted, we set the remaining parameters to

$$\alpha = 0.5, \quad \phi = 1, \quad \alpha_1 = -0.1, \quad k = 0.2, \quad b = 10, \quad \varepsilon = 10^{-5}, \quad (145)$$

which is based on the values used in [149].

**BIFURCATION ANALYSIS OF THE FAST SYSTEM.** The fast system of (144) is obtained by setting  $\varepsilon = 0$ . It is independent of  $b_1$ , so at fixed  $s$  the slow variable  $z$  serves as the bifurcation parameter. Figure 35 shows a bifurcation diagram of the fast system at fixed  $s = -1.95$ . The branch of fixed points is stable for large negative  $z$  values. As  $z$  increases, the fixed point loses stability in a subcritical Hopf bifurcation (H), undergoes a saddle-node bifurcation at large  $z$  (not shown in the figure), then regains stability in a second saddle-node bifurcation (SN). Fixed points between the two saddle-node bifurcations are of saddle-type, with one stable and one unstable eigenvalue. The branch of repelling periodic orbits created in the Hopf bifurcation undergoes a saddle-node bifurcation (SNP) then terminates in a homoclinic bifurcation (Ho) — i.e., a homoclinic connection to the saddle fixed point. Figure 35 also includes a trajectory of the full HR system which illustrates sub-Hopf/fold cycle bursting. With the default choice of parameters, the HR system already exhibits a key feature required for torus canards: a saddle-node of periodic orbits in the fast system.

**TORUS BIFURCATION IN THE FULL SYSTEM.** The second key ingredient to the emergence of torus canards is the presence of a torus bifurcation (TR) in the full system, between the regimes of rapid spiking and bursting. To see that this does occur in the HR system (144), consider the bifurcation diagram of the full system shown in Fig. 36 at fixed  $s = -1.95$ . As  $b_1$  increases, the branch of stable fixed points undergoes a supercritical Hopf bifurcation at  $b_1 \simeq -0.1927$ , creating a branch of stable periodic orbits. This branch of periodic orbits changes stability in two torus bifurcations, the first of which occurs near the Hopf bifurcation where the periodic orbits are of very small amplitude. Beyond the second torus bifurcation at  $b_1 \simeq -0.1603$ , the periodic orbits are stable and correspond to the rapid spiking state of the system. It is this upper torus bifurcation, which lies between the regimes of spiking and bursting, that is associated with torus canards.

**TORUS CANARD EXPLOSION.** The transition from spiking to bursting as  $b_1$  decreases through the torus bifurcation at  $b_1 \simeq -0.1603$  occurs by way of a torus canard explosion. When  $b_1$  is above the torus bifurcation, the periodic orbit of the full system is stable. This trajectory resembles a

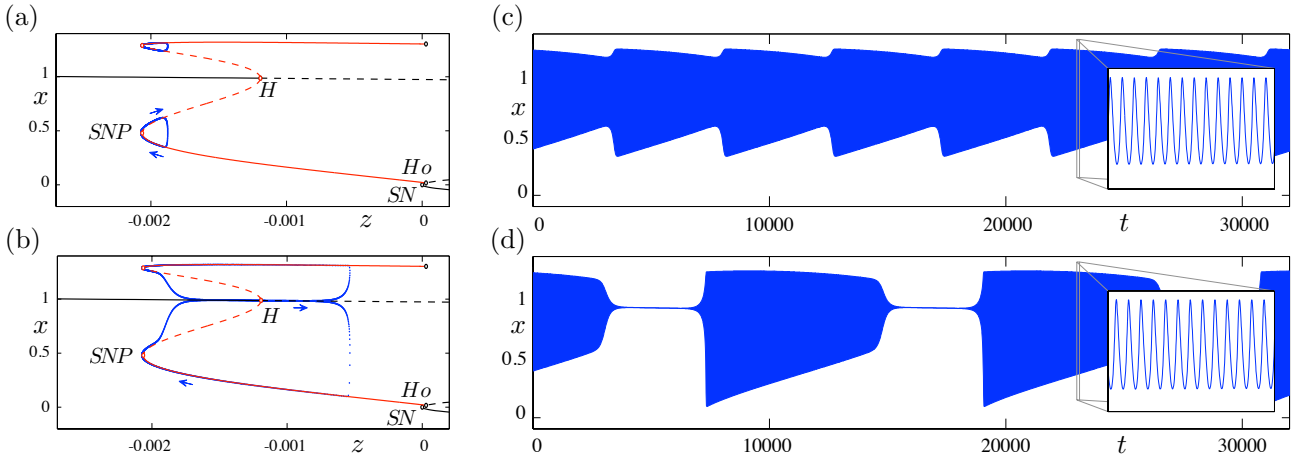


Figure 37: Poincaré map of torus canard trajectories in the HR system (144) at  $s = -1.95$ : (a) torus canard without head at  $b_1 = -0.16046985$ , and (b) torus canard with head at  $b_1 = -0.16047$ . The bifurcation diagrams of the fast system includes branches of fixed points and periodic orbits. The time series of these torus canard orbits are shown in panels (c) and (d), respectively.

periodic orbit taken from the attracting branch of periodic orbits of the fast system at a value of  $z$  near  $SNp$  (refer to the bifurcation diagram in Fig. 35). As  $b_1$  decreases below the torus bifurcation, the rapid spiking begins to modulate in amplitude as the trajectory winds around the attracting torus created near  $SNp$ . Further decrease of  $b_1$  causes the torus to grow, and eventually parts of the torus shadow, in alternation, the attracting and repelling branches of periodic orbits of the fast system. As  $b_1$  decreases further, this leads first to torus canards without heads, then torus canards with heads. To illustrate these dynamics, Fig. 37 (a-b) shows two torus canards in projection onto the  $(z, x)$  phase space, and panels (c-d) show the corresponding time series for the  $x$  coordinate.

This bifurcation sequence, consisting of a family of headless torus canards (Fig. 37 (a)) followed by MMO and a family of torus canards with heads (Fig. 37 (b)), constitutes a torus canard explosion. Moreover, the torus canard explosion marks the transition regime from spiking to sub-Hopf/fold cycle bursting: when  $b_1$  is sufficiently negative (i.e., sufficiently past the torus canard explosion), the trajectory does not follow the branch of repelling periodic orbits and instead falls directly off the saddle-node of periodic orbits, resulting in a large amplitude bursting orbit such as the one shown in Fig. 35 at  $b_1 = -0.162$ .

## “TWO SLOW / TWO FAST” SYSTEMS: BURSTING WITH FOLDED SINGULARITIES

---

Elements of the material presented in this chapter have been published in [29] and submitted [31]. Our contribution concerns the first study of a “two slow / two fast” system possessing both a folded node and square-wave type bursting, hence producing a new type of complex oscillations with multiple time scales, which we termed Mixed-Mode Bursting Oscillations (MMBOs). We constructed the first MMBO model as an extended of the classical HR burster, where we put a slow dynamics on the applied current since it corresponds to the parameter organising the spike-adding canard explosion in the original three-dimensional model (see Chapter 4). We showed the presence of a folded and could recover classical estimates regarding the number of small oscillations in the resulting four-dimensional system. This result is presented in the first section. We have a similar recent result, presented in the second section, where we study the effect of folded-saddle dynamics with bursting due to a Saddle-Node on Invariant Circle (SNIC) bifurcation in the fast subsystem, and we show that many known parabolic bursters have this particular canard structure. We also show that the spike-adding transition in such cases is due to both the presence of a folded-saddle singularity and of a homoclinic connection in the DRS. Finally, we propose a polynomial “two slow / two fast” system which has all these features and possesses the same behaviour as the main conductance-based parabolic burster, that is, the Plant model.

### 5.1 MIXED-MODE BURSTING OSCILLATIONS (MMBOS)

This section concerns the phenomenon of *Mixed-Mode Bursting Oscillations* (MMBOs). These are solutions of fast-slow systems of ordinary differential equations that exhibit both small-amplitude oscillations (SAOs) and bursts consisting of one or multiple large-amplitude oscillations (LAOs). The name MMBO is given in analogy to Mixed-Mode Oscillations (MMOs), which consist of alternating SAOs and LAOs, without the LAOs being organized into burst events. We show how MMBOs are created naturally in systems that have a spike-adding bifurcation, or spike-adding mechanism, and in which the dynamics of one (or more) of the slow variables causes the system to pass slowly through that bifurcation. Canards are central to the dynamics of MMBOs, and their role in shaping the MMBOs is two-fold: saddle-type canards are involved in the spike-adding mechanism of the underlying burster and permit one to understand the number of LAOs in each burst event, and folded-node canards arise due to the slow passage effect and control the number of SAOs. The analysis is carried out for a prototypical fourth-order system of this type, which consists of the third-order Hindmarsh-Rose (HR) system, known to have the spike-adding mechanism, and in which one of the key bifurcation parameters also varies slowly. We also include a discussion of the MMBO phenomenon for the Morris-Lecar-Terman system.

An open question involves what happens when a system exhibits slow passage through the spike-adding bifurcation, and it is this question which we address in the present section. We show that slow passage through a spike-adding bifurcation gives rise to complex oscillations. The solutions exhibit complex oscillations with small-amplitude oscillations around the fold point of the fast nullcline, interspersed with large-amplitude oscillations, but contrary to MMOs, the large-amplitude oscillations occur in bursts. This is why we choose to name this more elaborate type of complex oscillations Mixed-Mode Bursting Oscillations or MMBOs. A principal difference here is that the

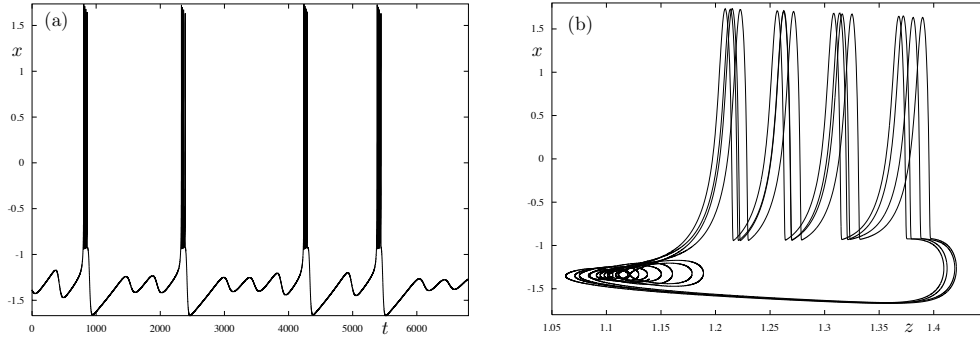


Figure 38: Simulation of system (146)–(149) for  $\varepsilon = 10^{-3}$ ,  $k = 10^{-2}$  and  $h_i = 10^{-2}$  for  $i = x, y, I$ . The orbit shown here is clearly of MMBO type, that is, a succession of small-amplitude slow oscillations and large-amplitude fast oscillations. The observed MMBO pattern is irregular and combines transitions of the type  $4^1$ ,  $4^2$  and  $4^3$ .

system has two fast variables, which allows for fast oscillations; then, the fast component of the periodic attractors are bursts.

MMBOs are also relevant in the modeling of biological rhythms. For instance, the model of pancreatic  $\beta$ -cells proposed by Bertram *et al.* in [14] has the right structure to sustain MMBOs and the time series shown in [14] (e.g. fig.3) clearly displays both small-amplitude slow oscillations and bursts of large-amplitude fast oscillations.

We investigate the presence of MMBOs in the following system:

$$x' = y - ax^3 + bx^2 + I - z, \quad (146)$$

$$y' = c - dx^2 - y, \quad (147)$$

$$z' = \varepsilon(s(x - x_1) - z), \quad (148)$$

$$I' = \varepsilon(k - h_x(x - x_{\text{fold}})^2 - h_y(y - y_{\text{fold}})^2 - h_I(I - I_{\text{fold}})). \quad (149)$$

System (146)–(149) is an extension of the HR burster, where the main bifurcation parameter, the applied current  $I$ , evolves slowly. In equation (149), the  $I$  component of the vector field is an elementary model for dynamical clamping of the current, in that it accounts for the lowest order terms that would be present in a generic dynamical clamping protocol that slowly adjusts the applied current. In equations (146)–(148), which correspond to the HR system, we consider the classical parameter values, as follows:  $a = 1$ ,  $b = 3$ ,  $c = 1$ ,  $d = 5$ ,  $\varepsilon = 0.001$ ,  $s = 4$ ,  $x_1 = -1.618$ ; note that the small parameter  $\varepsilon$  is usually denoted by  $r$ . The critical manifold of the HR burster is the curve

$$S_0 = \{x' = 0\} \cap \{y' = 0\} = \{z = -ax^3 + (b - d)x^2 + I + c\}. \quad (150)$$

The terms  $x_{\text{fold}}$  and  $y_{\text{fold}}$  correspond to the lower fold point of  $S_0$ . Therefore, we have

$$x_{\text{fold}} = \frac{2(b - d)}{3a}, \quad y_{\text{fold}} = c - dx_{\text{fold}}^2. \quad (151)$$

Furthermore, the value  $I_{\text{fold}}$  is chosen so that the slow nullcline of the HR burster  $\{z = s(x - x_1)\}$  goes exactly through the fold of  $S_0$ . Thus, we have

$$I_{\text{fold}} = ax_{\text{fold}}^3 - (b - d)x_{\text{fold}}^2 + s(x_{\text{fold}} - x_1) - c. \quad (152)$$

The main new result is that slow passage through  $I_{\text{fold}}$  combined with a suitable return mechanism leads to MMBOs. More generally, our goals are to understand the dynamics of MMBOs, in particular to show that they result from a slow passage through a spike-adding canard explosion and to show how the number of SAOs is controlled, via folded node theory, by the system parameter  $k$ . Along the way, we will show that the point  $(I_{\text{fold}}, 0)$  in the parameter space  $(I, \varepsilon)$  is the accumulation point of the wedges corresponding to spike-adding transitions. We add that the transition we study



results in a system that has a folded node singularity with a global return that includes bursting dynamics of square wave type and which maps the trajectories leaving the folded node region back to the funnel region of the folded node. This description is a generalization of the characterization of the MMO dynamics given in [18]. These results may be generalized to other problems where a spike-adding transition occurs. The principal requirement is that the parameter which unfolds this transition evolves slowly in the full system.

The HR model has been used as a simple framework for single-cell dynamics, in relation to neurological diseases such as epilepsy [120]. We extend the HR model by putting a slow dynamics on the applied current  $I$ . Kispersky *et al.* [84] created a biophysically accurate model of a stellate cell from the entorhinal cortex and argued that the STO dynamics occurring in this model could be linked to the presence of hyperexcitability in models of temporal lobe epilepsy [95]. This mechanism relies on strong sensitivity of the neuronal model to parameter variation, which is a property of the dynamics considered here. We provide a canonical description of a very sensitive parameter region where small variation of a parameter could lead to large changes of dynamics and in particular of the firing rate. Moreover, the use of a phenomenological model (as opposed to a biophysical model) provides a theoretical/canonical framework to analyze dynamic properties of MMBOs observed in both healthy and diseased neurons in a way that is independent of the details of the participating ionic currents that are responsible for each aspect of the dynamics.

#### 5.1.1 MMBOs as a slow passage through a spike-adding canard explosion

The full system (146)–(149), in which  $I$  is also a slow variable, exhibits a broad class of new solutions known as MMBOs, which are periodic or aperiodic solutions that consist of two distinct phases: a segment of small-amplitude oscillations (SAOs) in alternation with a burst event or multiple burst events, with each burst comprising one or more large-amplitude oscillations (LAOs) or spikes. A prototypical MMBO of the full system has been presented in Fig. 38. There, a variable number of SAOs (ranging from one to three) occur in alternation with a burst event that consists of four LAOs.

We will now study the MMBOs in the slow passage through canard explosion regime. We show that the LAOs occur due to slow passage through the spike-adding bifurcation, coupled with a global return mechanism. In this regime, for moderate values of  $\varepsilon$ , the MMBO patterns found are quite complicated and can evolve dynamically in time. In contrast, in Section 5.1.2, we use the theory of folded nodes for fast-slow systems to show that the number of SAOs in an MMBO may be controlled by the system parameter  $k$ . The observed MMBO patterns are then much more regular and correspond to smaller values of  $\varepsilon$ . The notation for an MMBO with  $s$  SAOs and  $\ell$  LAOs per burst is  $\ell^s$ . With this notation, MMOs are simple examples of MMBOs.

##### 5.1.1.1 Understanding MMBOs as a slow passage through a canard explosion

We now focus on the dynamics of MMBO trajectories as a slow passage through a canard explosion. Hence in this section we consider the case of  $\varepsilon$  relatively large.

The MMBOs are characterized by the number of SAO during the first phase and the number of bursts during the second phase, as well as the number of LAOs within each burst. An elementary example is given by the MMBO shown in Fig. 39(a). It consists of one SAO followed by a single burst event, which consists of eight LAOs, and this pattern repeats five times. Then, after the fifth transition of this type, there is a burst with seven LAOs, which is not preceded by an SAO. Overall, this  $8^1 8^1 8^1 8^1 7^0$  repeats itself for time up to at least  $t = 100,000$ , and only a segment of amplitude about 20,000 is shown.

Within the cycle of the five successive  $8^1$ , the SAO have increasing amplitudes. The time series for the variable  $I$  shown in Fig. 39 reveals that the  $I$  variable repeatedly passes through the interval (centered about  $I = 0.869$ ) corresponding to the spike-adding mechanism; this value corresponds to the  $I$ -value of the folded node, we indicate it as a dashed red curve in both panels (c) and (d) for

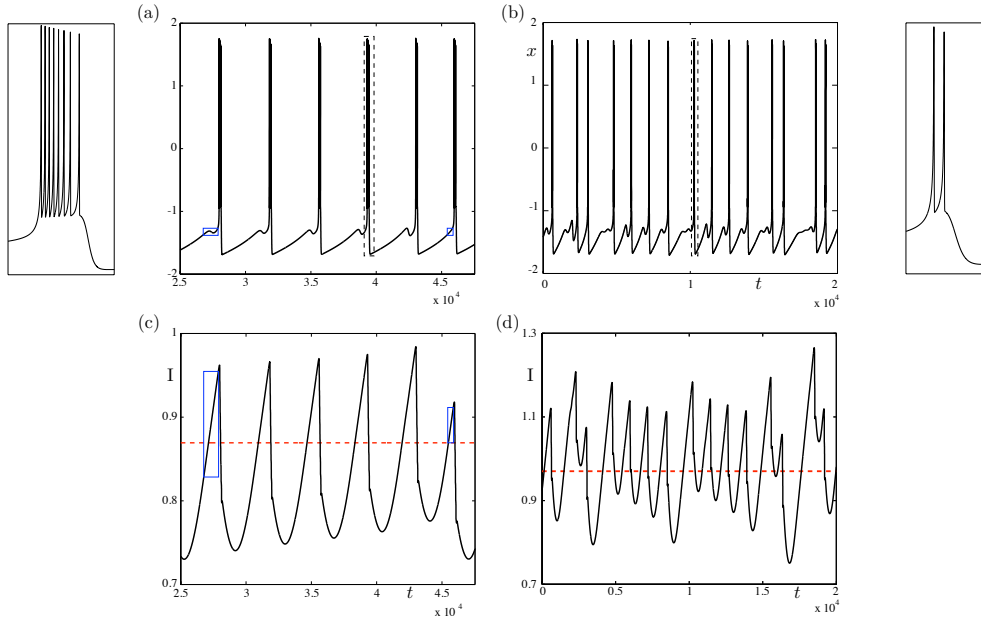


Figure 39: Periodic MMBOs of system (146)–(149), for  $k = 0.45$ ,  $\varepsilon = 2.5 \cdot 10^{-4}$  (panel (a) for the  $x$  variable and panel (c) for the  $I$  variable) and  $k = 0.35$ ,  $\varepsilon = 10^{-3}$  (panels (b) and (d) for the  $x$  variable and the  $I$  variable, respectively); in all panels  $h_x = 5$  and  $h_y = h_I = 10^{-2}$ . In panels (c) and (d), the dashed red curve indicates the value of  $I$  corresponding to the folded node. The unlabelled panels to the side of panel (a) and panel (b) show zooms into one burst of the corresponding MMBO, with 8 LAOs (left panel) and 2 LAOs (right panel).

each value of  $k$ . With each passage, the value of  $z$  at which the jump from the branch of repelling equilibria up to the branch of attracting periodic orbits occurs decreases slightly, so that the resulting SAO has a larger amplitude.

Next, the fact that after the fifth  $8^1$  there is no SAO preceding the LAOs may be understood as follows. From the plots of the  $x$  and  $I$  variables, one sees that if the orbit reaches the fold of  $S_0$  after  $I$  goes above the value of the folded node then it does not complete a SAO but directly jumps to the LAO regime; see the blue boxes in Fig. 39(a) and (c). Hence, there is no SAO preceding the subsequent LAOs. Also, within the sequence of  $8^1$ , the amplitudes of the successive SAOs increase, marking a dynamic approach to the first secondary canard.

Finally, the fact that after the fifth  $8^1$  the following burst has lost one LAO can be understood by looking at the time evolution of  $I$ ; see Fig. 39(c). Indeed, the loss of the SAO due to the slow passage through a canard explosion induces the orbit to jump at the lower fold and start the burst earlier. The dynamics of  $I$  is affected and as a result it changes the location of the homoclinic connection of the fast subsystem, whose associated saddle equilibrium happens for a lower value of  $z$ . This explains why the burst is shorter in this case.

Another prototypical MMBO is shown in Fig. 39 (b), but now the pattern is highly irregular. We see alternations between the basic blocks  $2^2$ ,  $2^0$  and  $2^1$ . Focusing on the LAOs which are not preceded by SAOs, three of which occur in the time series shown, one near the beginning and two near the end, we see from the times series of the  $I$ -variable that the value of  $I$  does not dip below  $I_{\text{fold}}$ , which explains the absence of SAOs. One may use a similar explanation by looking at the behaviour of the  $I$ -variable during the three corresponding peaks.

What we have just seen with the two examples of MMBOs shown in Fig. 39 is valid for “moderate” values of  $\varepsilon$ , that is, such that  $\varepsilon$  does not become very small relative to  $k$ . In this situation, the slow passage through canard explosion can modify dynamically the number of SAOs within one transition, and the  $I$  dynamics can also alter the number of LAOs within each burst due to changes in the location of the homoclinic connection in the underlying fast subsystem. However, in order to understand the MMBO pattern using folded node theory, one has to decrease  $\varepsilon$  substantially.

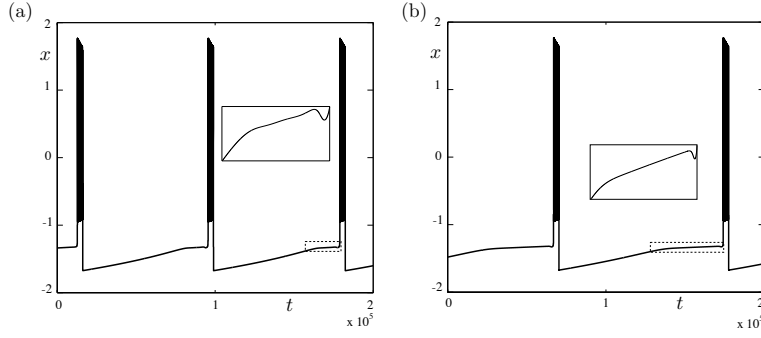


Figure 40: Periodic MMBOs of system (146)–(149), for  $k = 0.45$  (panel (a)) and  $k = 0.35$  (panel (b)) and for  $\varepsilon = 10^{-5}$ ; in both panels  $h_x = 5$  and  $h_y = h_I = 10^{-2}$ . Decreasing  $\varepsilon$  allows to find MMBOs with the correct number of SAOs as predicted by folded node theory via formula (159). In both cases, the number of LAOs is very large, about 200.

The patterns gain more LAOs per burst and become more regular as the parameter  $\varepsilon$  is decreased. The MMBOs shown in Figs. 40 (a) and (b) are for the same parameter values as those shown in Figs. 39 (a) and (b), however the values of  $\varepsilon$  are much smaller. In particular, while one sees the pattern  $8^1 8^1 8^1 8^1 7^0$  for  $k = 0.45$  and  $\varepsilon = 0.001$  in Fig. 39 (a), one sees a periodic  $N^3$  pattern with  $N = 192$  for the much smaller value  $\varepsilon = 10^{-5}$ , as shown in Fig. 40 (a). Similarly, with  $k = 0.35$ , the pattern becomes a regular  $N^5$  pattern with  $N = 194$  for  $\varepsilon = 10^{-5}$ , as shown in Fig. 7(b). The number of spikes per burst has increased dramatically because of the chasm between the fast and slow timescales when  $\varepsilon = 10^{-5}$ . Moreover, as we will show in the following subsection, the number of SAOs has increased from 3 to 5 as  $k$  is decreased, due to the dynamics near the folded node.

### 5.1.2 Controlling the number of SAOs in MMBOs using folded node theory

In Section 5.1.1.1 we have discussed a series of transitions which occur upon variation of  $I$  and lead to MMBO dynamics. As a result one obtains a system with a folded node point and a global return passing through bursting dynamics. This is a generalization of the perspective on MMOs given in [18]; consequently a prototypical context of MMBOs is a combination of folded node dynamics with a global return including bursting dynamics and returning the trajectories which leave the folded node region back to the funnel of the folded node, see also [14]. We now consider the case when  $I < I_{\text{Rmfold}}$  (sufficiently close to  $I_{\text{Rmfold}}$ ). In this case, there is a folded node in the four-dimensional extended Hindmarsh-Rose system (146)–(149). We determine the number of SAOs in a given MMBO by using the local folded node theory from [144] and its extension to systems with two fast dimensions [18].

Changing to the slow time  $\tau = \varepsilon t$  gives the equivalent system

$$\begin{aligned} \varepsilon \dot{x} &= y - ax^3 + bx^2 + I - z, \\ \varepsilon \dot{y} &= c - dx^2 - y, \\ \dot{z} &= s(x - x_1) - z, \\ \dot{I} &= k - h_x(x - x_{\text{fold}})^2 - h_y(y - y_{\text{fold}})^2 - h_I(I - I_{\text{fold}}), \end{aligned} \tag{153}$$

The  $\varepsilon = 0$  limit of system (153) gives the reduced system, that is, differential equations for the slow variables  $z$  and  $I$  constrained by algebraic equations defining the critical manifold  $S_0$ , recall (150). This manifold is a cubic hypersurface in  $\mathbb{R}^4$ . By projection onto the three-dimensional phase space  $(x, z, I)$ ,  $S_0$  is a cubic surface with two curves of fold points (with respect to the fast variable  $x$ )  $F^+$  and  $F^-$ , given by

$$F^+ = \{x = 0\}, \quad F^- = \left\{x = \frac{2(b-d)}{3a}\right\}.$$

Differentiating the algebraic condition (150) defining  $S_0$  with respect to time gives a differential equation for  $x$

$$\begin{aligned} x(3ax - 2(b - d))\dot{x} &= \dot{I} - \dot{z} \\ &= -ax^3 + (b - d)x^2 + I + c - s(x - x_1) + \\ &\quad k - h_x(x - x_{\text{fold}})^2 - h_y(y - y_{\text{fold}})^2 - h_I(I - I_{\text{fold}}). \end{aligned}$$

It is customary to append to that equation one slow equation, for instance that of  $I$ . The resulting two-dimensional system is singular along the fold set  $F = F^+ \cup F^-$  of  $S_0$ . In order to extend that system up to the fold set  $F$ , one typically desingularises it by performing a time rescaling, here with a factor  $x(3ax - 2(b - d))$ ; see for instance [18, 145] for the general theory. Therefore, one obtains a planar non-singular system given by

$$\begin{aligned} \dot{x} &= -ax^3 + (b - d)x^2 + I + c - s(x - x_1) + k - h_x(x - x_{\text{fold}})^2 - h_y(y - y_{\text{fold}})^2 - h_I(I - I_{\text{fold}}) \\ \dot{I} &= x(3ax - 2(b - d)) (k - h_x(x - x_{\text{fold}})^2 - h_y(y - y_{\text{fold}})^2 - h_I(I - I_{\text{fold}})). \end{aligned} \quad (154)$$

System (154)–(155) is the Desingularised Reduced System (DRS). Equilibria of the DRS lying on  $F$  are therefore folded singularities for the original system given that they are not equilibrium solutions there. We focus on the folded singularity satisfying  $x_f \neq 0$ , that is,

$$x_f = \frac{2(b - d)}{3a} = x_{\text{fold}}. \quad (156)$$

From the previous equality comes immediately that  $y_f = y_{\text{fold}}$ . Using the  $x$ -equation of the DRS, we find that

$$I_f = \frac{ax_{\text{fold}}^3 - (b - d)x_{\text{fold}}^2 - c + s(x_{\text{fold}} - x_1) - k - h_I I_{\text{fold}}}{1 - h_I}.$$

In the first four terms of the numerator above, we recognise the expression of  $I_{\text{fold}}$  given in (169). Therefore, we have

$$I_f = I_{\text{fold}} - \frac{k}{1 - h_I}. \quad (157)$$

Now, the Jacobian matrix of the DRS at the folded singularity  $(x_f, I_f)$  is given by

$$\begin{pmatrix} -s & 1 - h_I \\ (6ax_f - 2(b - d))(k - h_I(I_f - I_{\text{fold}})) & 0 \end{pmatrix}.$$

Using (176) and (177), we see that the lower left entry further simplifies to

$$2(b - d) \frac{k}{1 - h_I}.$$

Consequently, the two eigenvalues of the folded singularity are given by

$$\lambda_{\pm} = 0.5 \left( -s \pm \sqrt{s^2 + 8k(b - d)} \right),$$

which gives a node provided that  $s^2 + 8k(b - d) > 0$  and  $b - d < 0$ . Finally, we obtain the following expression for the eigenvalue ratio  $\mu$  at the folded node

$$\mu = \frac{\lambda_+}{\lambda_-} = \frac{s \left( s - \sqrt{s^2 + 8k(b - d)} \right) + 4k(b - d)}{4k(d - b)}. \quad (158)$$

This ratio  $\mu$  determines  $n$ , the number of SAOs, as follows. The general theory, see for instance [18], states that for  $0 < \varepsilon \ll 1$  small enough, there are at most  $n + 1$  small oscillations near the folded node, that is,  $n$  secondary canards and  $n + 1$  sectors of rotation, where

$$2n + 1 < \frac{1}{\mu} < 2n + 3 \quad (n \in \mathbb{N}).$$

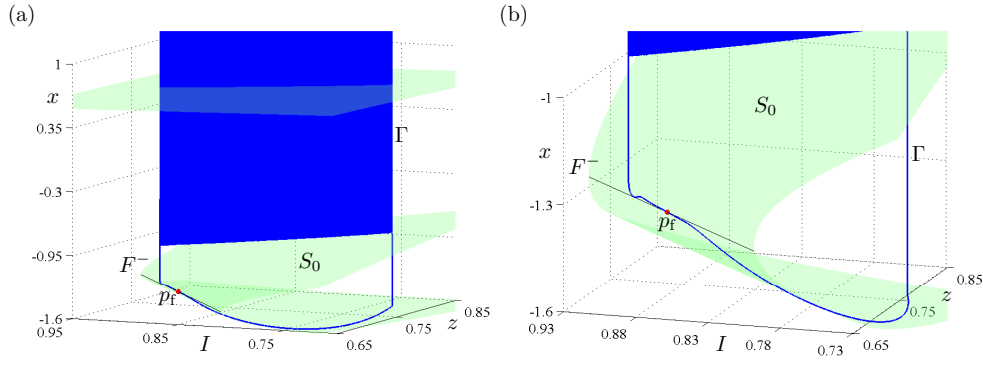


Figure 41: Periodic  $192^3$ -MMBOs of system (146)–(149), obtained for  $k = 0.45$ , that is,  $1/\mu \approx 6.74$ , and  $\varepsilon = 10^{-5}$ , and projected onto the  $(x, z, I)$ -space; also shown are the critical manifold  $S_0$  and the lower fold curve  $F^-$ . Panel (b) is an enlargement of panel (a) near the folded node  $p_f = (x_f, y_f, z_f, I_f)$ .

In the present case, for the fixed (classical) parameter values  $s = 4$ ,  $b = 3$  and  $d = 5$ , formula (158) reduces to

$$\mu = \frac{2(1 - \sqrt{1 - k}) - k}{k}. \quad (159)$$

In Fig. 40, we show a periodic MMBO pattern  $1_3^{192}$  obtained by direct simulation for  $k = 0.45$ , that is,  $1/\mu \approx 6.74$ , and  $\varepsilon = 10^{-5}$ . Therefore, based on (159), one expects at most three small oscillations and three sectors of rotation, separated by the strong canard  $\gamma_s$  and two secondary canards. We show both the time profile of that solution as well as its projection onto the  $(x, y, z)$ -space. Reducing  $\varepsilon$  allows one to observe the correct number of SAOs around the folded node  $p_f$  of the system, as predicted by theory; see [18]. Indeed, in Fig. 40(a), we find 3 SAOs, as predicted by formula (159). Similarly, for  $k = 0.35$ , the theory predicts  $1/\mu \approx 9.32$ , that is, 5 SAOs and that is exactly what is shown in Fig. 40(b), which shows the MMBO pattern of  $194^5$ .

The number of SAOs will typically be constant and maximal only for MMBOs which are not close to spike adding in their burst segment. As an MMBO undergoes a spike adding transition the return point on the stable slow manifold can move quite wildly, passing between different sectors of rotation. This can result in the presence of very complicated patterns, not just in the part of the burst segment of the dynamics but also in the segment corresponding to SAOs.

## 5.2 SPIKE-ADDING MECHANISM IN PARABOLIC BURSTERS

We now move to another example of “two slow/two fast” system where the bursting dynamics is organised by folded-singularity canards. Surprisingly, this new case happens to coincide with an important class of bursters, namely, parabolic bursters. The work presented in this section therefore sheds new mathematical insights on neuroscience models that exhibit parabolic bursting, and also proposes a novel four-dimensional canonical and polynomial-based parabolic burster. In addition to this new polynomial system, the set of models considered here include the four-dimensional biophysical conductance-based model of the *Aplysia* R15 neuron known as Plant’s model, and minimal models for parabolic bursting with phase equations, in particular the three-dimensional theta model by Rinzel; for a discussion on the role of canards in the two-dimensional so-called *Atoll* or *theta* model by Ermentrout and Kopell, see [31]. Revisiting these models from the perspective of slow-fast dynamics reveals that the number of spikes per burst may vary upon parameter changes, however the spike-adding process occurs in a brutal (explosive) fashion that involves canards. This spike-adding canard explosion phenomenon is analysed by using tools from GSPT in tandem with numerical bifurcation techniques. The same geometric bifurcation structure persists across the three- and four-dimensional models of parabolic bursting that we consider, that is, spikes within the burst



are incremented via the crossing of an excitability threshold given by a particular type of canard orbit, namely the strong canard of a folded-saddle singularity.

Bursting oscillations are said to be parabolic when the burst initiates and terminates with arbitrary low frequency, hence exhibiting a parabolic-shaped curve when measuring the interspike intervals along a burst. In the time domain the observed oscillatory pattern consists of periodic bursts of activity “superimposed” onto a slow wave, which can be explained by the interaction between two oscillatory processes, one evolving on a slow timescale and the other evolving on a fast timescale. Mathematically, this bursting type translates to dynamical-system models with at least four state variables, two slow variables and two fast variables. The dynamics of the slow and fast variables can be further reduced to phase variables (by using polar coordinate transformations), resulting in either planar or three-dimensional models if the coordinate transformation is applied either to the fast processes or to both slow and fast processes. However, it is worth mentioning that Izhikevich [78] has proposed other types of parabolic bursters using hybrid models, without the underlying slow wave; such models will not be considered in the present work.

Parabolic bursting was first observed in *Aplysia* R15 ganglion cells and the first biophysical (Hodgkin-Huxley type) model was proposed by R. E. Plant and collaborators [123], this model being rapidly referred to as *Plant’s model*. This work inspired research within the field of mathematical and computational neuroscience to develop novel techniques based on numerical bifurcation analysis and singular perturbation, which enabled the analysis and classification of bursting cells into easily distinguishable groups (e.g. parabolic, elliptic and square-wave). Within parabolic bursting, this classification process started with the pioneering work of R. E. Plant [124, 122] where a comparison between the parabolic bursting behaviour of the full system and the behaviour of the fast system was made. Subsequently, J. Rinzel [131, 4] studied more thoroughly a modified version of Plant’s model, from the perspective of slow-fast dynamics, in particular using *slow-fast dissection* [130] (see below) and averaging [142]. Rinzel also developed a three-dimensional phase model for parabolic bursting, which the present work revisits using slow-fast theory in Section 5.2.1.2. In parallel to the work of Rinzel and co-authors, throughout the 1980s, Ermentrout and Kopell [48] further reduced parabolic bursting canonical models to two phase variables (so-called *Ermentrout-Kopell canonical model*, *theta* or *Atoll model*) and studied the bifurcation structure of this canonical model. In the mid-1990s, Soto-Treviño *et al.* [143] revisited the Ermentrout-Kopell theorem and managed to weaken the required assumption for the reduction.

Computational neuroscience studies have tried to explore the use of parabolic bursters to model various aspects of neurophysiological data, for example, neurons [124, 122], muscle cells [123], or cortical cells [56]. The envisaged thought is that these results will inform experimental neuroscience and explain the importance of bursting as well as the functional properties of the type of bursting. Presently, much is unknown, but a general consensus is that bursts are responsible for controlling and maintaining steady rhythms, for example, breathing and locomotion (central pattern generators). Several studies have also shown that bursting neurons can encode information in the number of spikes per bursts: as the stimulus varies, so does the length of individual bursts. More difficult to explain is the functional role of the various bursts types. However, It is thought that the burst type could be specialized to carry different type of information (i.e. stimulus features) and much work is still being carried out to understand what features depend on the mathematical properties of the underlying burst type [137]. The present study addresses one key aspect, which is explaining via slow-fast theory how spikes are added to the burst with respect to an input. Therefore this work contributes to the larger body of theoretical studies that hypothesize that instantaneous spike variation carries information [128].

As explained at the beginning of Chapter 4, slow-fast dissection is a little more delicate in the case of parabolic bursting systems, due to the presence of two slow variables and, hence, two main parameters in the fast subsystem. The way to obtain information from the fast subsystem is then to compute curves of bifurcation points in two parameters (the two frozen slow variables) and trace them, in a three-dimensional phase-space projection, together with the projection of the critical



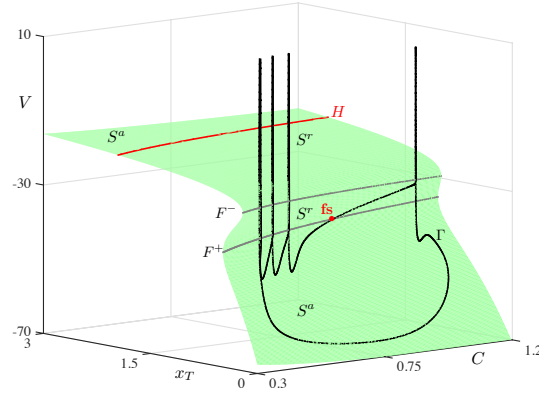


Figure 42: Bursting solution of Plant’s model (42) containing a canard segment, represented in three-dimensional projection onto the  $(x_T, C, V)$ -space. The black orbit  $\Gamma$  is a limit cycle with three fully developed spikes and one spike “almost” formed (close to longest canard). It follows both the attracting sheet  $S^a$  and one repelling sheet  $S^r$  of the critical manifold  $S^0$  (green surface), whose fold curves  $F^\pm$  separate the external sheets (lower  $S^a$  and upper  $S^r$ ) from the central repelling sheet  $S^r$ . The underlying folded saddle is shown by a red dot and labelled fs.

manifold, which can be parametrized by these two parameters of the fast subsystem; see Fig. 42, which shows the result of this procedure. The periodic solution of the full four-dimensional system (black) is superimposed onto the (green) surface  $S^0$  of equilibria of the fast subsystem. This surface  $S^0 := \{\mathbf{f} = \mathbf{0}\}$  is of course the critical manifold of the system. It is folded along two curves,  $F_\pm$ , that correspond to curves of saddle-node bifurcations of equilibria of the fast subsystem. The fold curves are equivalently defined by the algebraic condition  $\det(\mathbf{f}_x) = 0$ , where  $\mathbf{f}_x$  denotes the Jacobian of (143) with respect to the fast variables. It is well-known since [130] that in parabolic bursters, the fast oscillations are initiated and terminated when the orbit passes through one of the fold curves  $F_\pm$ , where the centre manifolds of the saddle-node equilibria of the fast subsystem form an invariant circle, which by perturbation creates limit cycles with very large period. This bifurcation of the fast subsystem is called a Saddle-Node on Invariant Circle (SNIC) bifurcation, also referred to as circle bifurcation. From the classification in [76], parabolic bursting then corresponds to a SNIC-SNIC bursting.

The slow-fast dissection method, used in the context of parabolic bursting in [131, 4], allows to decompose the system (143) into its fast and slow subsystems, typically denoted by FAST and SLOW respectively, and to analyse them separately: in FAST, one eliminates the slow variables by considering their dynamics frozen and, hence, assuming that they act as parameters in the equations for the fast variables; in SLOW, one eliminates the fast variables by using a quasi-steady state approximation, assuming that the slow dynamics is restricted to the manifold of equilibria of the fast equations (fast nullsurface, i.e. the critical manifold  $S^0$ ), and by using fast averaging in the regime where the fast variables oscillate. Then, a bifurcation analysis of the resulting flows is performed in both approximations, and the resulting separate dynamics are reconciled in order to inform about the original full system; see in particular [131, 4, 142] for a fruitful application of this technique to parabolic bursting systems, in particular, to Plant’s model. However, one can push more the singular perturbation analysis by desingularising the slow flow in the vicinity of fold curves of the critical manifold in order to investigate the possibility for canard-type solutions and analyse their organisation in the singular phase space. In systems with two slow variables, this deginsularisation procedure may reveal the classical phase portrait of an equilibrium (node, saddle, focus, saddle-node) located on the fold curve of the critical manifold; one then speaks of a *folded singularity* and one can prove that this point (which is not an equilibrium of the full system) can generate canard dynamics for  $\varepsilon > 0$  small enough. This desingularisation approach is classical in canard problems [28, 93, 144] but, to be the best of our knowledge, it has not been previously employed

in parabolic bursters. Therefore, the present Section revisits the slow flow of parabolic bursting and studies its singular limit near non-hyperbolic regions of the critical manifold  $S^0$ . In the case of the three-dimensional theta model by Rinzel and the four-dimensional model by Plant, we identify a folded-saddle singularity that generates canard solutions for  $0 < \varepsilon \ll 1$ . Moreover, the folded saddle organises the addition of new spikes. For the case of two-dimensional Atoll model, we show that the spike adding is explained by so-called jump-on canards. The spike-adding phenomenon appears to be a general feature of bursting oscillations and contributions towards this direction was provided by our latest work on square-wave bursters [29]. This phenomenon is a consequence of the multiple-timescale structure of most bursting models and results from the existence of canard solutions.

This contribution also complements previous knowledge on this type of bursting by showing that, in the case of three-dimensional and four-dimensional parabolic bursters, there must be a homoclinic bifurcation occurring in the desingularised slow flow, involving the folded saddle, on top of the well-known family of SNIC bifurcations in the fast flow. Moreover, for the parabolic bursters that we have considered, the spike-adding transition can be continuous or discontinuous but it always involves canard solutions. The distinction between these two cases is related to the intrinsic geometry of the problem, more precisely, to the presence or not of a second fold curve on the critical manifold, on top of the curve of SNIC points of the fast subsystem. For instance, Plant's model is based on the Hodgkin-Huxley formalism and it has a cubic-shaped critical manifold; therefore the spike-adding is continuous. However, Rinzel's model is based on the theta model of Ermentrout and Kopell [48] and, therefore, contains a phase variable  $\theta$  which makes its associated critical manifold  $2\pi$ -periodic, each connected component having only one fold curve. Consequently, the canard-mediated spike-adding mechanism in Rinzel's model is discontinuous. This understanding leads us to the derivation of a novel canonical (polynomial based) four-dimensional parabolic burster. Our new polynomial approximation of Plant's model is inspired from the Hindmarsh-Rose burster [71] but with an additional slow dynamics on the applied current, very much in the flavour of the model derived by the authors in [29] to introduce Mixed-Mode Bursting Oscillations (MMBOs). The added slow dynamics creates a folded-saddle singularity on the SNIC fold curve of the critical manifold. This is in contrast to the model studied in [29], where this singularity is a folded node. Instead, for our proposed canonical model, we construct the model in such a way that it possesses a folded saddle and features a continuous spike-adding transition via associated canards. As a consequence, the model entirely matches the dynamics of the Plant's model. However, note that it is possible to have a folded node (and, therefore, MMBOs) in Plant's model and in Rinzel's model, when varying a few parameters away from the classical set of parameter values; see Section 5.2.2.

The methods applied in the present work include singular perturbation theory, the dissection method, and it also involves the use of numerical continuation algorithms for slow-fast systems [28]. Specifically, trajectory segments (such as canard orbits) are computed as solutions to two-point boundary-value problems in conjunction with a numerical continuation strategy, which allows to obtain a one-parameter family of such solutions. We have used the software package AUTO [38] to perform these computations (both bifurcation analysis and computation of canard segments); see the demo files `fnc` included in the manual of AUTO for details. In addition, we use the software package MATHEMATICA [106] to perform algebraic manipulation in the singular limit of Plant's model; see Section 5.2.1.1 below.

### 5.2.1 Plant's model and its new polynomial approximation

#### 5.2.1.1 Plant's biophysical model of the *Aplysia* R15 neuron

We begin our study of spike-adding in parabolic bursters with Richard Plant's biophysical model for the *Aplysia* R15 bursting neuron, which was introduced in 1978 [121], later simplified in 1981 [122],

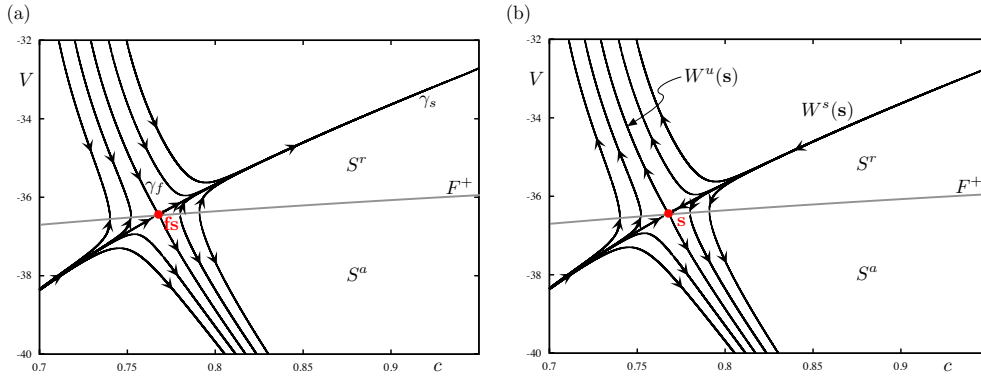


Figure 43: (a) Slow flow of Plant's model (42), computed by solving the associated Differential-Algebraic Equation (163) (DAE). (b) Flow of the Desingularized Reduced System (DRS) for Plant's model, showing the characteristics of a saddle equilibrium  $s$  with its stable manifold  $W^s(s)$  and its unstable manifold  $W^u(s)$ . In the "true" reduced flow, it implies that this point is a folded saddle  $fs$  and the two special trajectories are the strong canard  $\gamma_s$  and the faux canard  $\gamma_f$ .

and ever since considered as a classical conductance-based parabolic burster. The final version is a five-dimensional model given as follows:

$$\begin{aligned} \dot{V} &= (g_I s_I^3(V) y_I + g_T x_T) (V_I - V) + \left( g_K x_K^4 + \frac{g_p c}{K_p + c} \right) (V_K - V) + g_L (V_L - V) = f(V, x_T, x_K, y_I, c), \\ \dot{x}_i &= (s_i(V) - x_i) / \tau_{x_i}, \quad i = T, K \\ \dot{y}_I &= (z_I(V) - y_I) / \tau_{y_I}, \\ \dot{c} &= \rho (K_c x_T(V) (V_{Ca} - V) - c); \end{aligned} \tag{160}$$

see [122] for details on the sigmoid-shaped activation functions and classical parameter values. The preliminary studies by Plant in [122] hinted that there is an underlying slow sub-system of model (160). However, given that the model is based on the Hodgkin-Huxley formalism, it was not clear how to identify an obvious time-scale separation (i.e. a small parameter  $\varepsilon$ ). In addition, Plant hinted at the spike-adding phenomenon without analysing it mathematically. In [131], Rinzel revisited Plant's work by employing his then newly developed slow-fast dissection method. The approach taken to identify the separation of time scale was by direct simulations of system (160), where two slow variables, namely,  $x_T$  and  $c$ , and three fast variables,  $V$ ,  $x_K$  and  $y_I$  were identified. Rinzel understood the shape of parabolic bursting by analyzing the bifurcation structure of the fast system. Specifically, it becomes clear that the fast system has a curve of SNIC when freezing the remaining two slow variables and considering them as parameters. Following this approach, we can formally recast system (160) as a slow-fast system, the timescale separation parameter  $\varepsilon$  being equal to  $\min(1/\tau_{x_T}, \rho)$ . Moreover, by virtue of the well-established singular perturbation theory we can now further analyze the slow-fast structure of the problem when  $\varepsilon$  tends to zero. Doing so in the (equivalent) slow-time parametrisation of system (160) yields the critical manifold  $S^0$ , which is given by the following set of algebraic equations:

$$\begin{aligned} f(V, x_T, x_K, y_I, c) &= 0, \\ x_K &= s_K(V), \\ y_I &= z_I(V). \end{aligned} \tag{161}$$

A visualisation of the corresponding surface (shown in green in Fig. 42) confirms that it has locally two fold curves  $F^\pm$ . It is also straightforward to verify numerically that the outer sheets  $S^a$  of  $S^0$  are attracting while the middle sheet  $S^r$  is repelling. Using geometric singular perturbation theory for systems with two slow variables (see e.g. [28] for details), we can find a folded-saddle singularity  $fs$  in this system, that is, a point that allows the slow dynamics to follow the lower attracting sheet  $S^a$

of  $S^0$  and subsequently its central repelling sheet  $S^r$ , without jumping when reaching the fold curve  $F^+$ . Note that there is a second repelling part on  $S^0$ , on the other side of the upper fold curve  $F^-$ ; this is due to the presence of a curve of Hopf bifurcation points of the fast subsystem on the upper sheet of  $S^0$ , which divides this sheet into an attracting part and a repelling part. This is typical of parabolic bursting and explains the actual burst, which is due to the presence of a two-parameter family of limit cycles in the fast subsystem. In particular, we can show that for the parameter values corresponding to Fig. 42, which are in the range considered by Plant and Rinzel, the so-called *normal switching conditions* [111] are not satisfied; that is,

$$(f_{x_T} \dot{x}_T + f_c \dot{c})|_{f_s} = 0, \quad (162)$$

where  $f_x$  denotes the partial derivative of  $f$  with respect to variable  $x$ . This algebraic calculation is messy for system (42) due to its strong nonlinearities (sigmoid-type functions) and high dimension. We have performed these calculations with the software MATHEMATICA [106], however we refrain from showing the rather lengthy expressions that we obtained. The evaluation of formula (162) at the numerically computed point,  $f_s$ , indeed gives zero. To confirm these symbolic computations, we provide a numerical evidence of the presence of a folded saddle in system (42) by computing the flow of the reduced system

$$\begin{aligned} f(V, x_T, x_K, y_I, c) &= 0, \\ x_K &= s_K(V), \\ y_I &= z_I(V), \\ \dot{x}_T &= k(s_i(V) - x_i), \\ \dot{y}_I &= (z_I(V) - y_I)/\tau_{y_I}, \\ \dot{c} &= K_c x_T(V)(V_{Ca} - V) - c, \end{aligned} \quad (163)$$

where we rewrite  $1/\tau_{x_T}$  as  $\rho k$ . Fixing the ratio between  $\rho$  and  $\tau_{x_T}$  enables to consider that system (42) has two slow variables and to derive the Differential-Algebraic Equation (163) (DAE) which governs the reduced system of Plant's model. The associated slow flow takes place on the critical manifold  $S^0$  and approximates the slow dynamics of system (42) in the singular limit  $\varepsilon = 0$ . System (163) can be simulated using adequate numerical schemes for DAEs and we obtain the computed reduced slow flow presented in Fig. 43 panel (a); the computation was performed using the DAE solver implemented within the software package XPPAUT [47]. This phase portrait is typical of a folded-saddle singularity (indicated by a red dot). Indeed, by reversing the time orientation on the repelling sheet  $S^r$  of the critical manifold we obtain the phase portrait shown in panel (b), which possess a saddle equilibrium  $s$  with its stable manifold  $W^s(s)$  and its unstable manifold  $W^u(s)$ . This corresponds to the so-called Desingularised Reduced System (DRS) of Plant's model (see Section 5.2.1.2 below). The true reduced flow on the critical manifold is shown in panel (a), where the singularity on the fold curve  $F^+$  is not an equilibrium point but instead a folded singularity, which may be reached in finite time and crossed. This means that the flow goes through this point, crosses it, and continues on the other side giving rise to canard dynamics. Two singular canards exist and these correspond to the special trajectories  $W^{s,u}(s)$  of the DRS: these are the strong canard  $\gamma_s$  and the "faux" canard  $\gamma_f$  (named this way because it connects the repelling side to the attracting side instead of the opposite as a normal canard). We refer the reader to the next section for details about these concepts, in the context of a simpler vector field where all calculations can be easily carried out by hand. The limit cycle  $\Gamma$  shown on Fig. 42 illustrates well the effect of the folded-saddle singularity  $f_s$  on the burst part of this periodic solution. For the chosen value of parameter  $G_I$ , one can compute (using AUTO [38]) such a limit cycle, which contains a long segment crossing from the attracting to the (central) repelling sheet of  $S^0$ . Such a segment may be called a canard segment, and the overall cycle is a canard of folded-saddle type. It is clear from this figure that the fourth spike of this bursting cycle is different in nature from the other three, in that it corresponds to a jump from  $F^-$  as opposed to a jump from  $F^+$  for the first three spikes. This suggests that, in order to "add" one more spike

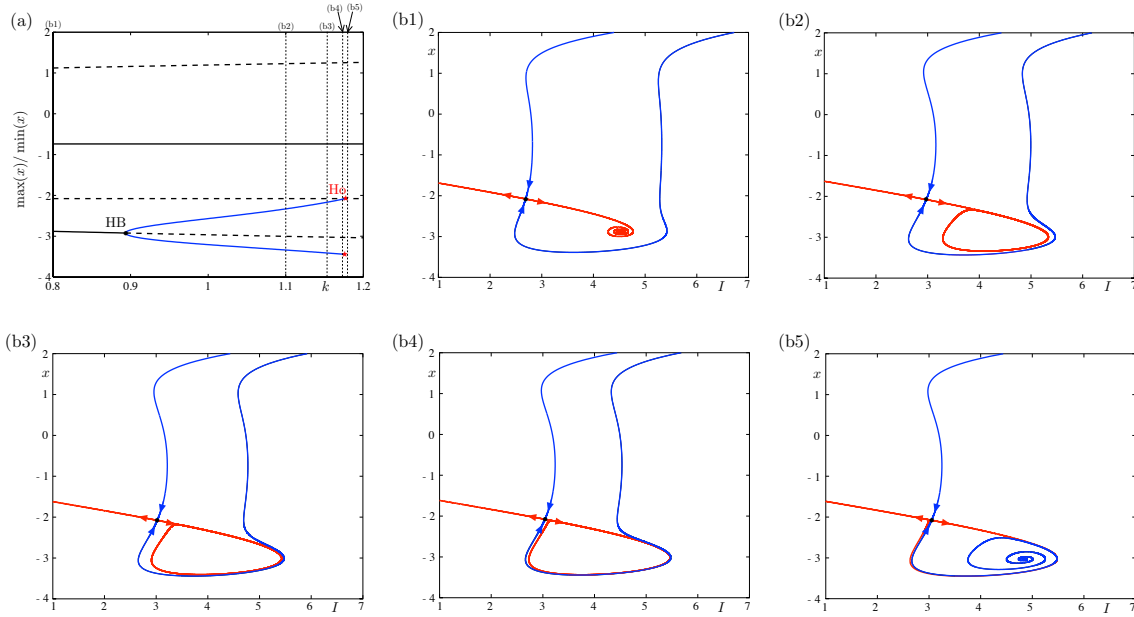


Figure 44: Main dynamical elements of the slow flow of the canonical parabolic bursting model (164). Panel (a): Bifurcation structure of the DRS with respect to parameter  $k$ . Panels (b1)-(b5): phase portrait of the DRS for a few selected values of  $k$  across the bifurcation diagram shown in panel (a).

upon parameter variation, system (42) must possess a family of limit cycles with canard segments that extend from one fold curve to the other. This is related to the existence of an important maximal canard solution — maximal in the sense that it follows the repelling part of  $S^0$  from one fold curve to the other —, termed the strong canard, and defined geometrically in the singular limit as the stable manifold of the folded saddle (seen as an equilibrium of the desingularised reduced system); see sections 5.2.2 and 5.2.1.2 for details. The *singular* strong canard perturbs to a trajectory of the full system for  $0 < \varepsilon \ll 1$ , which in this context is part of a limit cycle lying on the first quasi-vertical segment of the branch shown in Fig. 48 (a). The entire process described above forms the *canard-mediated spike-adding explosion*, the explosive feature being a trademark of canard phenomena. The addition of a spike, upon parameter variation, therefore corresponds to the crossing of the strong canard, which for this case corresponds to the excitability threshold. That role of excitability threshold for the strong canard associated with a folded saddle has already been analysed in [112] in a different model, and it is directly related to the role of stable manifolds of saddle equilibria as repelling slow manifolds in planar excitable models [30, 78]. Moreover, this canard transition between bursting cycles with  $n$  spikes per burst and cycles with  $n + 1$  spikes per burst is continuous, as can be observed in Fig. 48 (a). This is mainly due to the geometry of the critical manifold, which is cubic-shaped, and therefore allows the strong canard to extend all through the (central) repelling sheet of the critical manifold and to connect to a second repelling sheet  $S^+$  along the fold curve  $F^-$ . However, the final spike-adding (in this case the fifth canard explosion) terminates due to a homoclinic bifurcation of the full system. The maximum number of spikes that the model may add upon parameter variations depends on other system parameters, in particular those affecting the timescales.

#### 5.2.1.2 A canonical model with two slow variables and two fast variables

Given the complexity of Plant's model, that is, its large dimension and strong nonlinearities, a natural question is then whether one can construct a canonical model of the spike-adding mechanism in such parabolic bursters. The present section investigates this by inspiring from the polynomial spiking models such as the FitzHugh-Nagumo model [53, 114], and polynomial bursting models such as the Hindmarsh-Rose model [71]. We can now make a link to our work [29] presented in Section 5.1, where we have shown how to construct a four-dimensional model with slow passage through burst-



ing oscillations, hence creating a folded-node singularity. This then enables the generation of both Small-Amplitude Oscillations (SAOs) and bursting oscillations, that is, MMBO. Following these ideas, we construct a model with a slow passage through a three-dimensional burster (a variant of the Hindmarsh-Rose burster) whose fast subsystem possesses a SNIC bifurcation in such a way to make this slow passage create a folded-saddle singularity in the resulting four-dimensional system. This gives rise to the following canonical model:

$$\begin{aligned} x' &= c(x - x^3/3 - y + z + I), \\ y' &= (x^2 + dx - by + a)/c, \\ z' &= \varepsilon(z - s(x - x_1)), \\ I' &= \varepsilon(k - h_x(x - x_{\text{fold}})^2 - h_y(y - y_{\text{fold}})^2 - h_I(I - I_{\text{fold}})), \end{aligned} \quad (164)$$

where  $I$  is the applied current that evolves slowly. The system parameters are  $a, b, c$  and  $d$  and  $x_{\text{fold}}, y_{\text{fold}}$  and  $I_{\text{fold}}$  are constants whose meaning will be explained below. Since system (164) is based on a variant of the Hindmarsh-Rose (HR) burster, then the resulting canonical construction allows for the fast subsystem of (164) to display a SNIC bifurcation, an essential element in order to obtain parabolic bursting in the extended model. The  $I$ -equation of (164) was chosen so as to have the lowest-order terms possible while producing the adequate oscillatory behaviour for the current. For the first three equations of (164), which correspond to the HR model, we consider the classical parameter values, that is:  $a = 0.08, b = 0.71, c = 3, d = 1.8, \varepsilon = 0.002, s = 4, x_1 = -1.6$ . Note that the small parameter  $\varepsilon$  is usually denoted by  $r$ ; the parameter values of the return mechanism ( $I$ -equation) are all chosen strictly positive. The key dynamics of the proposed model are the SNIC bifurcation in the fast system and a homoclinic-like loop in the reduced system, which connects the folded saddle to itself. We argue that the transition to parabolic bursting is given by the breaking of this connection. If the connection breaks in one direction then the resulting dynamics is a slow periodic orbit. If the connection breaks in the opposite direction then the resulting slow dynamics is a passage through a jump point followed by a fast excursion along the SNIC orbit, which is equivalent to the first parabolic burst. The transition between these two types of behavior occurs via a folded-saddle canard. The results on the sequence of bifurcations in the slow system are more conveniently stated in the context of the DRS. This system is derived from the reduced system through a singular time rescaling which removes the singularity at the folded line and turns the folded saddle point into a saddle equilibrium [10, 144]. In what follows we employ the standard steps of slow-fast analysis of (164), leading up to the DRS system, which enables us to restate our claims in this setting.

The critical manifold of (164) is the two-dimensional surface  $S_0 = \{x' = 0\} \cap \{y' = 0\}$ , that is the manifold defined by the constraints:

$$y = \frac{1}{b}(x^2 + dx + a) \quad (165)$$

$$z = \frac{x^3}{3} + \frac{x^2 + dx + a}{b} - x - I. \quad (166)$$

Note that  $S_0$  is parametrized by  $x$  and  $I$  and has a fold line given by the image of the line  $\{x = x_{\text{fold}}\}$ , where

$$x_{\text{fold}}^2 + \frac{2}{b}x_{\text{fold}} + \frac{d}{b} - 1 = 0, \quad (167)$$

In particular  $x_{\text{fold}}$  appearing in (164) is the solution of (167) corresponding to the lower fold line of (164) and  $y_{\text{fold}}$  is the  $y$  value corresponding to the fold line. Solving (167) yields

$$x_{\text{fold}\pm} = -\frac{1}{b} \left( 1 \pm \sqrt{1 + b(b - d)} \right), \quad y_{\text{fold}\pm} = \frac{x_{\text{fold}\pm}^2 + dx_{\text{fold}\pm} + a}{b}. \quad (168)$$

Furthermore, the value  $I_{\text{fold}}$  is chosen so that the slow nullcline of the modified HR burster  $\{z =$



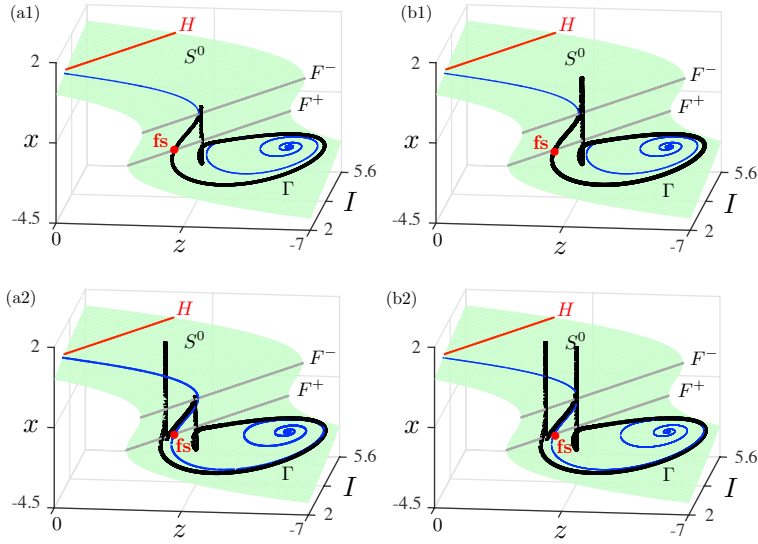


Figure 45: Solutions of the canonical parabolic bursting system (164) containing canard segments during the adding of the first spike in panels (a1)-(b1), and that of the second spike in panels (a2)-(b2). In each panel, the black orbit  $\Gamma$  is a limit cycle with one fully developed spike and one spike “almost” formed (close to maximal canard). It follows both attracting and repelling parts of the critical manifold (green surface). The blue curve is the *singular strong canard*, corresponding to the stable manifold of the folded saddle (red dot labelled fs) seen as a saddle equilibrium of the DRS.

$s(x - x_1)$  passes exactly through the fold of  $S_0$ . Thus, we have

$$I_{\text{fold}\pm} = \frac{x_{\text{fold}}^3}{3} + \frac{x_{\text{fold}\pm}^2 + dx_{\text{fold}\pm} + a}{b} - x_{\text{fold}\pm} - s(x_{\text{fold}\pm} - x_1). \quad (169)$$

In fact, only the lower fold will be involved in the presence of a folded saddle in the full four-dimensional model. Rescaling time by introducing  $\tau = \varepsilon t$  gives the equivalent system

$$\begin{aligned} \varepsilon \dot{x} &= c(x - x^3/3 - y + z + I), \\ \varepsilon \dot{y} &= (x^2 + dx - by + a)/c, \\ \dot{z} &= z - s(x - x_1), \\ \dot{I} &= k - h_x(x - x_{\text{fold}})^2 - h_y(y - y_{\text{fold}})^2 - h_I(I - I_{\text{fold}}). \end{aligned} \quad (170)$$

Setting  $\varepsilon = 0$  in (170) results in the singular approximation of the slow dynamics. This reduced system is composed by differential equations for the slow variables  $z$  and  $I$  constrained by algebraic equations defining the fast nullsurface, that is, the critical manifold  $S_0$ , recall (165) and (166). The resulting flow is the so-called slow flow, already mentioned in previous sections, and whose analysis crucially reveals the presence of a homoclinic bifurcation through the folded saddle as a key element to the spike-adding process. The manifold  $S^0$  is a cubic surface in  $\mathbb{R}^4$  and its projection onto the three-dimensional phase space  $(x, z, I)$ , is a cubic hypersurface with two curves of fold points (with respect to the fast variable  $x$ )  $F^+$  and  $F^-$ , given by

$$F^+ = \{x = x_{\text{fold}+}\}, \quad F^- = \{x = x_{\text{fold}-}\}.$$

Note that algebraic condition (166) gives an expression of  $z$  as a function of  $x$ . Differentiating (166) with respect to time and using (170) we obtain a differential equation for  $x$

$$(x^2 + \frac{2}{b}x + \frac{d}{b} - 1)\dot{x} = \dot{z} + \dot{I} \quad (171)$$

$$= \frac{x^3}{3} + \frac{x^2 + dx + a}{b} - x - I - s(x - x_1) + \quad (172)$$

$$k - h_x(x - x_{\text{fold}})^2 - h_y(y - y_{\text{fold}})^2 - h_I(I - I_{\text{fold}}). \quad (173)$$

We can now express the reduced system in terms of the variables  $x$  and  $I$ , using (171) and the constraints (165) and (166). This procedure gives the following formulation of the reduced system:

$$\begin{aligned} \left(x^2 + \frac{2}{b}x + \frac{d}{b} - 1\right) \dot{x} &= \frac{x^3}{3} + \frac{x^2 + dx + a}{b} - x - I - s(x - x_1) + k - h_x(x - x_{\text{fold}})^2 - h_y(y - y_{\text{fold}})^2 - h_I(I - I_{\text{fold}}) \\ \dot{I} &= (k - h_x(x - x_{\text{fold}})^2 - h_y(y - y_{\text{fold}})^2 - h_I(I - I_{\text{fold}})). \end{aligned} \quad (174)$$

The resulting system is formulated in terms of  $x$  and  $I$  and the constraints (165) and (166) have been eliminated. Note that (182) is singular along the fold set  $F = F^+ \cup F^-$ , which reflects that singularity of  $S_0$ . In order to extend the domain of definition of (182) up to the fold set  $F$ , one typically desingularises it by performing a singular time rescaling, here with a factor  $x(3ax - 2(b - d))$ ; see for instance [18, 28] for the general theory. Therefore, one obtains a planar non-singular system given by

$$\begin{aligned} \dot{x} &= \frac{x^3}{3} + \frac{x^2 + dx + a}{b} - x - I - s(x - x_1) + k - h_x(x - x_{\text{fold}})^2 - h_y(y - y_{\text{fold}})^2 - h_I(I - I_{\text{fold}}) \\ \dot{I} &= \left(x^2 + \frac{2}{b}x + \frac{d}{b} - 1\right) (k - h_x(x - x_{\text{fold}})^2 - h_y(y - y_{\text{fold}})^2 - h_I(I - I_{\text{fold}})). \end{aligned} \quad (175)$$

System (175) is called the *Desingularised Reduced System (DRS)*. Equilibria of the DRS lying on  $F$  are called *pseudo-equilibria* or *folded singularities* for the original system given that they are not equilibrium solutions there. We focus on the folded singularity satisfying  $x_f \neq 0$ , that is,

$$x_f = -\frac{1}{b} \left(1 + \sqrt{1 + b(b - d)}\right) = x_{\text{fold}+}. \quad (176)$$

From the previous equality it follows immediately that  $y_f = y_{\text{fold}+}$ . Using the  $x$ -equation of the DRS, we find that

$$I_f = \frac{x_f^3/3 + (x_f^2 + dx_f + a)/b - x_f - s(x_f - x_1) + k + h_I I_{\text{fold}+}}{1 + h_I}.$$

In the first four terms of the numerator above, we recognise the expression of  $I_{\text{fold}+}$  given in (169). Therefore, we have

$$I_f = I_{\text{fold}+} + \frac{k}{1 + h_I}. \quad (177)$$

Now, the Jacobian matrix of the DRS at the folded singularity  $(x_f, I_f)$  is given by

$$\begin{pmatrix} -s & -(1 + h_I) \\ 2\left(x_f + \frac{1}{b}\right)(k - h_I(I_f - I_{\text{fold}})) & 0 \end{pmatrix}.$$

Using (176) and (177), we see that the lower left entry further simplifies to

$$2\left(x_f + \frac{1}{b}\right) \frac{k}{1 + h_I}.$$

Consequently, the condition to have a saddle (strictly negative determinant) is that  $x_f < -1/b$  ( $k$  has been chosen strictly positive), that is,

$$b(b - d) > -1.$$

Our further exploration of DRS system (175) relies on numerics, with the relevant orbits shown in Fig. 44. Our careful numerics show that (175) has the following sequence of dynamics, upon the variation of the parameter  $k$ .

1. Stable equilibrium.
2. Hopf bifurcation leading to a stable limit cycle.

3. Homoclinic bifurcation involving the saddle which corresponds to the folded saddle point.

The corresponding dynamics of the full system (164) with  $\varepsilon > 0$ :

1. Stable equilibrium.
2. Hopf bifurcation leading to a stable slow limit cycle.
3. A complex sequence of bifurcations born out of the homoclinic connection when  $\varepsilon = 0$  is replaced  $\varepsilon > 0$  and leading from a stable slow limit cycle to a solution with a parabolic burst.

It is not hard to show using classical methods that, with  $\varepsilon > 0$ , near the homoclinic connection there exist slow stable limit cycles as well as dynamics consisting of slow passage near the homoclinic orbit, jumps and passage near the SNIC orbit, arising as a recurrent sequence. The latter type of orbit is a parabolic burst with one spike. These two regions of dynamics correspond to breaking the connection via parameter  $k$  in the opposite directions. Note that by the results of [10, 144] there exists a unique canard solution near the folded saddle. Numerical exploration with AUTO [38] shows a homotopy transition upon variation of  $k$  from the region of slow oscillations to the region of parabolic bursting, see Fig. 48 (in the cases of Plant and Rinzel models, respectively). As  $k$  is increased further, additional spikes are added and each spike adding transition involves a passage of trajectories near the folded saddle canard. We believe that the entire sequence of bifurcations is very intricate and it would be a challenging problem to obtain its full picture. A more in-depth study of this system will be a subject of future work. Fig. 45 shows a bursting cycle with a (close to) maximal canard segment that clearly follows the strong canard associated with the folded saddle fs.

### 5.2.2 Rinzel's three-dimensional theta model

This section focuses on Rinzel's theta model [131], which is a phenomenological version of Plant model. We show that this model also possesses a folded-saddle singularity that organises the spike-adding mechanism however, via a discontinuous process in parameter space. The model is three-dimensional and given as follows:

$$\begin{aligned}\theta' &= 1 - \cos \theta + A(x, y), \\ x' &= \varepsilon_x (x_\infty(\theta) - x), \\ y' &= \varepsilon_y (y_\infty(\theta) - y),\end{aligned}\tag{178}$$

where  $A(x, y) = \tanh(ax - by + I)$  and  $s_\infty(\theta) = \sin(p_s + \theta)$  for  $s = x, y$ . The quantities  $a, b, I$  are parameters, and  $\varepsilon_s$  ( $s = x, y$ ) are small positive constants. The variable  $\theta$  is a phase variable, therefore the phase space of system (178) is  $S^1 \times \mathbb{R}^2$ . To facilitate a slow-fast analysis of system (178), we henceforth write:  $\varepsilon_y = \varepsilon$  and  $\varepsilon_x = k\varepsilon_y = k\varepsilon$ . Thus we will study the following slow-fast system with one fast variable and two slow variables

$$\begin{aligned}\theta' &= 1 - \cos \theta + A(x, y), \\ x' &= \varepsilon k (x_\infty(\theta) - x), \\ y' &= \varepsilon (y_\infty(\theta) - y).\end{aligned}\tag{179}$$

Changing to the fast time yields the following equivalent parametrisation of system (179)

$$\begin{aligned}\varepsilon \dot{\theta} &= 1 - \cos \theta + A(x, y) = f(\theta, x, y), \\ \dot{x} &= k(x_\infty(\theta) - x), \\ \dot{y} &= (y_\infty(\theta) - y).\end{aligned}\tag{180}$$

The critical manifold  $S^0$  of system (180) is given by

$$S_0 := \{ \cos \theta = 1 + A(x, y) \}.\tag{181}$$

In what follows we will show that the critical manifold  $S^0$ , given by equation (181), possesses a folded-saddle singularity and that geometrically the repelling part of  $S^0$  extends up to infinity thereby inducing spike-adding via a discontinuous process. To begin with, note that  $S^0$  defines a  $2\pi$ -periodic surface, with fold curve  $F$  defined by  $\{f_\theta = \sin \theta = 0\}$ , that is, corresponding to  $\theta = 0 \bmod 2\pi$ ; see Fig. 46 for a phase-space representation of the critical manifold. Indeed, for  $\theta = 0 \bmod \pi$ , the equation defining the critical manifold is not satisfied since  $|A(x, y)| < 1$ . Therefore, the fold curve  $F$  is simply  $\{\theta = 0 \bmod 2\pi\}$ , which is equivalent to  $A(x, y) = 0$  in the  $(x, y)$ -plane of slow variables, that is, the straight line of equation:  $ax - by + I = 0$ . It follows from slow-fast theory that systems with two slow variables and one fast variable, with a folded critical manifold, can display canard solutions; see Chapter 3. In this context, canards correspond to connection between two-dimensional attracting and repelling slow manifolds, which are possible when folded singularities are present on the fold curve of the critical manifold. We now show that indeed  $S^0$  possesses a folded singularity of saddle-type. Taking the singular limit ( $\varepsilon = 0$ ) of system (180) results in a DAE whereby the dynamics of the slow variables  $x$  and  $y$  are now constrained by an algebraic equation that corresponds to the critical manifold. This gives an approximation of the slow dynamics of the original problem but now taking place exactly on the critical manifold. In this framework, the dynamics of the fast variable  $\theta$  is hidden within the algebraic constraint and its standard to differentiate the constraints with respect to time in order to uncover the dynamics for  $\theta$  in the slow limit, which results in:

$$-f_\theta \dot{\theta} = f_x \dot{x} + f_y \dot{y}. \quad (182)$$

As long as  $f_x \dot{x} + f_y \dot{y} \neq 0$ , which corresponds to the normal switching condition, then equation (182) is singular whenever  $f_\theta = 0$ , that is, along the fold of  $S^0$ . In the original system, this situation gives rise to a switch from slow to fast dynamics and the associated point on the fold near which this switch happens is called a *jump point*. It marks the transition from slow dynamics near an attracting sheet of the critical manifold  $S^0$ , to fast motion in the direction of the fast variable orthogonally to the fold of  $S^0$ . If the normal switching condition fails, then the singularity in equation (182) can be resolved due to the cancellation of a single zero. Therefore, the dynamics of the reduced system can flow through such a point (i.e. a folded singularity) on the fold curve. This means that there is the possibility for trajectories of the reduced system to flow continuously from an attracting sheet to a repelling sheet of  $S^0$  through a folded singularity, namely the singular canards.

An alternative way to resolve the singularity is to consider the complete reduced system, that is, equation (182) together with the differential equation for one slow variable, for instance,  $x$ ; with the system we are investigating, this gives

$$\begin{aligned} -f_\theta \dot{\theta} &= f_x \dot{x} + f_y \dot{y}, \\ \dot{x} &= k(x_\infty(\theta) - x). \end{aligned} \quad (183)$$

Rescaling time by a factor  $-f_\theta$  in (183) yields the DRS

$$\begin{aligned} \theta' &= f_x \dot{x} + f_y \dot{y}, \\ x' &= -f_\theta k(x_\infty(\theta) - x), \end{aligned} \quad (184)$$

where  $y$  is replaced by its expression as a function of  $\theta$  and  $x$  on the critical manifold. It is now clear that the failure of the normal switching condition at a point on the fold curve of  $S_0$  corresponds to an equilibrium point of the DRS on this fold curve. That is, folded singularities of the reduced system are equilibria of the DRS located on the fold curve of  $S_0$ . Therefore, singular canards exist near folded singularities, that is, in the  $\varepsilon = 0$  limit of system (180). They may or may not persist for  $0 < \varepsilon \ll 1$  small enough, and it depends on the type of folded singularity.

Applying the aforementioned steps (for the resolution of the singularity) to the Rinzel's phase models gives the following failure of the normal switching conditions:

$$A_x(x, y)k(x_\infty(\theta) - x) + A_y(x, y)(y_\infty(\theta) - y) = 0, \quad (185)$$

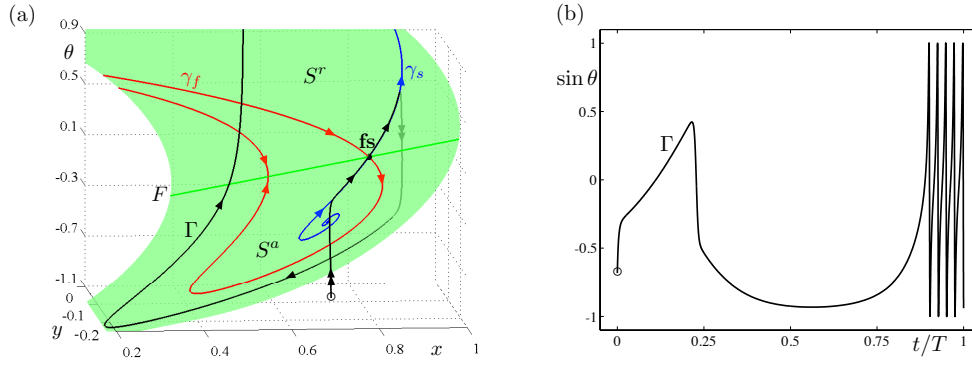


Figure 46: Solution of Rinzel's theta model (180) containing a canard segment. Panel (a) shows the trajectory in the phase space together with the critical manifold  $S_0$  (attracting sheet  $S^a$  and repelling sheet  $S^r$ , the fold curve  $F$ , the folded saddle (black dot) and its (un)stable manifolds (strong  $\gamma_s$  and faux  $\gamma_f$  singular canards). Panel (b) shows the time profile of the same trajectory, the plotted output being  $\sin \theta$ . In each panel, the circle denotes the initial condition.

with  $A_x(x, y) = a(1 - A^2(x, y))$  and  $A_y(x, y) = -b(1 - A^2(x, y))$ . Moreover, condition (185) must be fulfilled on the fold of  $S_0$ , that is, for  $\theta = 0 \bmod 2\pi$ , where the term  $A(x, y)$  vanishes. Hence, equation (185) reduces to

$$ak(x_\infty(\theta) - x) - b(y_\infty(\theta) - y) = 0, \quad (186)$$

with:  $y = (ax + I)/b$ . Therefore, the coordinates of the folded singularities of system (180) are

$$\begin{aligned} \theta_{fs} &= 0 \bmod 2\pi, \\ x_{fs} &= \frac{ak \sin p_x - b \sin p_y + I}{a(k-1)}, \\ y_{fs} &= \frac{ax_{fs} + I}{b}. \end{aligned} \quad (187)$$

The Jacobian matrix at the folded singularity  $(\theta_{fs}, x_{fs}, y_{fs})$  has the following form

$$J_{fs} = \begin{pmatrix} ak \cos p_x - b \cos p_y & -ak \\ -k(\sin p_x - x_{fs}) & 0 \end{pmatrix}, \quad (188)$$

Therefore, the condition for the folded equilibrium to be a saddle of the DRS is

$$ak^2(\sin p_x - x_{fs}) > 0, \quad (189)$$

which, according to the expression of  $x_{fs}$  in (187), gives

$$\frac{k^2}{|k-1|} (b \sin p_y - a \sin p_x - I) > 0, \quad (190)$$

that is,

$$I < b \sin p_y - a \sin p_x. \quad (191)$$

It is not difficult to check that for parameter values typically used in system (178) (see for instance [131]), the folded singularity  $fs := (\theta_{fs}, x_{fs}, y_{fs})$  given by (187) is a folded saddle. An illustration of the singular strong canard,  $\gamma_s$ , flowing along the critical manifold  $S_0$  through the folded saddle, is shown in Fig. 46 (a). Away from the singular limit, Fig. 46 (a) also shows a trajectory  $\Gamma$ , solution of the full system (180) with initial condition indicated by a circle, which closely follows the strong singular canard. That is, in accordance to Fenichel theory [52], the solution is attracted and flows ( $O(\varepsilon)$ -close) along the attracting sheet  $S^a$  of the critical manifold. Subsequently it passes

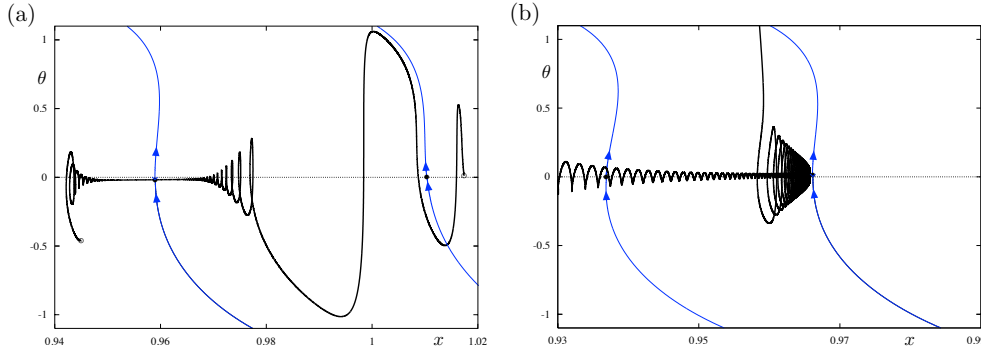


Figure 47: Solutions of Rinzel's theta model (180) corresponding to case 2, projected onto the  $(x, \theta)$  plane and superimposed on top of the invariant manifolds of the two equilibria of the DRS for the same value of  $I$ . Panel (a):  $I = -0.05$ , the folded equilibrium (right) is a folded saddle and the true equilibrium is a node (left), which attracts the overall dynamical of the full system. Panel (b):  $I = 0.05$ , the situation is opposite and the oscillatory pattern of the full dynamics is shaped by the passage through the folded node and near the true saddle.

near  $f_s$ , where Fenichel theory does not apply anymore, and then continues close to the repelling side  $S^r$  of the critical manifold. Then it jumps (back to the attracting side) and finally flows until it is ejected when reaching the fold curve at a jump point. The same orbit segment of the full system is shown in the time domain in Fig. 46 (b).

Returning back to the geometry of the  $(2\pi$ -periodic) critical manifold  $S^0$ , we note that every connected component of the manifold has a single fold and consequently both the repelling and the attracting sheet of the critical manifold extend to infinity; see Fig. 46 (a). It turns out that the single fold curve corresponds here as well to a curve of SNIC points of the fast subsystem; this is a clear trademark of all parabolic bursters. Therefore the repelling segment of the strong singular canard extends to infinity and the spike-adding process is discontinuous in parameter space; see Fig. 48 (b) for an illustration of this discontinuous spike-adding bifurcation scenario. Specifically, each branch of limit cycles with a given number of spikes per burst terminates at a homoclinic bifurcation, and all but the first one (born at a Hopf bifurcation) also stems from a homoclinic bifurcation. This is in contrast to Plant's model, where the solution branch of limit cycles gaining more and more spikes as a parameter is varied, is continuous; see Fig. 48 (a) for an illustration of this continuous spike-adding bifurcation scenario. This difference emerges due to the finite length of the repelling sheet of the critical manifold—and also of the strong singular canard—and the fact that this repelling sheet connects two attracting sheets.

Finally note, that the DRS of system (180) has an additional branch of equilibria, which are equilibria of the full system. In [131], two cases were considered depending of the relative size of  $\varepsilon_x$  with respect to  $\varepsilon_y$ : case 1 when  $k = \frac{\varepsilon_x}{\varepsilon_y} \gg 1$  and case 2 when  $k \ll 1$ . In each case, varying parameter  $I$  allows to move the system across the bursting regime; see figures 8 and 9 of [131]. Note that relation (191) is independent of  $k$ , therefore in either case (1 and 2) by varying  $I$  one observes the same bifurcations of the underlying structure of folded singularities within the system; see Fig 47 for an illustration. In particular, varying parameter  $I$  changes the type of folded singularity from one type to the other via a so-called folded-saddle node type II (FSNII), which occurs when the branch of folded singularities intersects the branch of true singularities of the system; see [93] for more details about this scenario. The condition for FSN II in system (46) is given as follows:

$$I = b \sin p_y - a \sin p_x. \quad (192)$$

The main difference between the two cases is the type of folded singularity that organises the dynamics in the bursting regime. In case 1 (figure 8 of [131]), the bursting is initiated when the limit cycle of the slow subsystem collides with the fold curve of the critical manifold, making a homoclinic connection with the folded saddle. The burst then terminates when  $I$  satisfies equation (192). An interesting topic for future work will be to investigate more closely the transition from bursting to



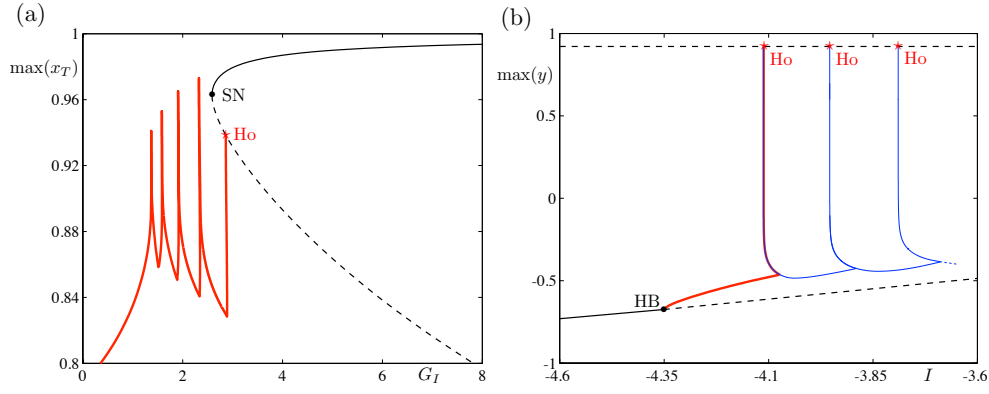


Figure 48: Comparison between two different spike-adding mechanisms : Plant's model in panel (a) vs Rinzel's theta model in panel (b). The adding is discontinuous in the former and continuous in the latter. Solutions branches shown are branches of equilibria (black), branches limit cycles born at a Hopf bifurcation labelled HB (red), and branches of limit cycles whose onset and offset correspond to a homoclinic bifurcation labelled Ho (red). Stable (resp. unstable) equilibrium branches are traced in solid (resp. dashed) lines.

spiking in this case, which may be related to the torus canard phenomenon [20, 86]. In contrast, case 2 sees the burst initiate through the FSN II transition and terminates with the disappearance of an unstable limit cycle of the average system studied in [131]. In both cases, the FSN II corresponds to one end of the bursting regime. Note that folded nodes can also appear in Plant's model, however the set of parameters have to be adjusted away from the typical parameters considered by Plant; we do not present this parameter regime here. A follow-up study will analyse more closely the transition from the folded-saddle to the folded-node regime, via the folded-saddle node bifurcation, in link with a change of type of homoclinic bifurcation (presumably, from SNIC to saddle-homoclinic bifurcation via saddle-node homoclinic bifurcation).

## BIBLIOGRAPHY

---

- [1] E. L. Allgower and K. Georg. Numerical path following. In P. G. Ciarlet and J.-L. Lions, editors, *Handbook of Numerical Analysis*, volume 5, pages 3–207. North Holland Publishing, 1997.
- [2] V. I. Arnol'd, V. S. Afrajmovich, Yu. S. Il'yashenko, and P. L. Shil'nikov. *Dynamical Systems V: Bifurcation Theory and Catastrophe Theory*. Encyclopædia of Mathematical Sciences. Springer-Verlag, Berlin, 1994.
- [3] D. Avitabile, M. Desroches, and S. Rodrigues. On the numerical continuation of isolas of equilibria. *International Journal of Bifurcation and Chaos*, **22**(11):1250277, 2012.
- [4] S. M. Baer, J. Rinzel, and H. Carrillo. Analysis of an autonomous phase model for neuronal parabolic bursting. *Journal of Mathematical Biology*, **33**(3):309–333, 1995.
- [5] D. Barkley. Slow manifolds and mixed-mode oscillations in the Belousov–Zhabotinskii reaction. *The Journal of Chemical Physics*, **89**(9):5547–5559, 1988.
- [6] B. P. Belousov. A periodically acting reaction and its mechanism. In *Collection of short papers on Radiation Medicine for 1958*, Med. Publ., pages 145–147. Moscow, 1959.
- [7] G. N. Benes, A. M. Barry, T. J. Kaper, M. A. Kramer, and J. Burke. An elementary model of torus canards. *Chaos*, **21**(2):023131, 2011.
- [8] E. Benoît. Systèmes lents-rapides dans  $\mathbb{R}^3$  et leurs canards. In *Troisième rencontre du Schnepfenried*, volume 109–110 of *Astérisque*, pages 159–191. Société Mathématique de France, 1983.
- [9] E. Benoît. Enlacements de canards. *Comptes-Rendus de l'Académie des Sciences de Paris - Série I*, **300**(8):225–230, 1985.
- [10] E. Benoît. Canards et enlacements. *Publications Mathématiques de l'Institut des Hautes Études Scientifiques*, **72**(1):63–91, 1990.
- [11] E. Benoît and C. Lobry. Les canards de  $\mathbb{R}^3$ . *Comptes-Rendus de l'Académie des Sciences de Paris - Série I*, **294**(14):483–488, 1982.
- [12] E. Benoît, J.-L. Callot, F. Diener, and M. Diener. Chasse au canard. *Collectanea Mathematica*, **31**(1–2):37–119, 1981.
- [13] R. Bertram, M. J. Butte, T. Kiemel, and A. Sherman. Topological and phenomenological classification of bursting oscillations. *Bulletin of Mathematical Biology*, **57**(3):413–439, 1995.
- [14] R. Bertram, J. Rhoads, and W. P. Cimborá. A phantom bursting mechanism for episodic bursting. *Bulletin of Mathematical Biology*, **70**(7):1979–1993, 2008.
- [15] M. Brøns. Bifurcations and instabilities in the Greitzer model for compressor system surge. *Mathematical Engineering in Industry*, **2**(1):51–63, 1988.
- [16] M. Brøns and K. Bar-Eli. Canard explosion and excitation in a model of the Belousov-Zhabotinskii reaction. *The Journal of Physical Chemistry*, **95**(22):8706–8713, 1991.
- [17] M. Brøns and K. Bar-Eli. Asymptotic analysis of canards in the EOE equations and the role of the inflection line. *Proceedings of the Royal Society of London. Series A: Mathematical and Physical Sciences*, **445**(1924):305–322, 1994.

- [18] M. Brøns, M. Krupa, and M. Wechselberger. Mixed mode oscillations due to the generalized canard phenomenon. In *Bifurcation theory and spatio-temporal pattern formation*, volume 49 of *Fields Institute Communications*, pages 39–63. American Mathematical Society, Providence, RI, 2006.
- [19] J. W. Bruce and P. J. Giblin. *Curves and Singularities: a geometrical introduction to singularity theory*. Cambridge university press, 1992.
- [20] J. Burke, M. Desroches, A. M. Barry, T. J. Kaper, and M. A. Kramer. A showcase of torus canards in neuronal bursters. *The Journal of Mathematical Neuroscience (JMN)*, 2(3), 2012.
- [21] M. O. Cunningham, M. A. Whittington, A. Bibbig, A. Roopun, F. E. N. LeBeau, A. Vogt, H. Monyer, E. H. Buhl, and R. D. Traub. A role for fast rhythmic bursting neurons in cortical gamma oscillations in vitro. *Proceedings of the National Academy of Sciences of the United States of America*, 101(18):7152–7157, 2004.
- [22] G. Cymbalyuk and A. Shil'nikov. Coexistence of tonic spiking oscillations in a leech neuron model. *Journal of Computational Neuroscience*, 18(3):255–263, 2005.
- [23] M. Desroches and M. R. Jeffrey. Canards and curvature: the “smallness” of  $\varepsilon$  in slow-fast dynamics. *Proceedings of the Royal Society of London. Series A: Mathematical and Physical Sciences*, 467(2132):2040–2021, 2011.
- [24] M. Desroches, B. Krauskopf, and H. M. Osinga. Mixed-mode oscillations and slow manifolds in the self-coupled FitzHugh-Nagumo system. *Chaos*, 18(1):015107, 2008.
- [25] M. Desroches, B. Krauskopf, and H. M. Osinga. The geometry of slow manifolds near a folded node. *SIAM Journal on Applied Dynamical Systems*, 7(4):1131–1162, 2008.
- [26] M. Desroches, B. Krauskopf, and H. M. Osinga. The geometry of mixed-mode oscillations in the Olsen model for the peroxidase–oxidase reaction. *Discrete and Continuous Dynamical Systems Series S*, 2(4):807, 2009.
- [27] M. Desroches, B. Krauskopf, and H. M. Osinga. Numerical continuation of canard orbits in slow-fast dynamical systems. *Nonlinearity*, 23(3):739, 2010.
- [28] M. Desroches, J. Guckenheimer, B. Krauskopf, C. Kuehn, H. M. Osinga, and M. Wechselberger. Mixed-mode oscillations with multiple time scales. *SIAM Review*, 54(2):211–288, 2012.
- [29] M. Desroches, T. J. Kaper, and M. Krupa. Mixed-mode bursting oscillations: Dynamics created by a slow passage through spike-adding canard explosion in a square-wave burster. *Chaos*, 23(4):046106, 2013.
- [30] M. Desroches, M. Krupa, and S. Rodrigues. Inflection, canards and excitability threshold in neuronal models. *Journal of Mathematical Biology*, 67(4):989–1017, 2013.
- [31] M. Desroches, M. Krupa, and S. Rodrigues. Spike-adding mechanism in parabolic bursters: the role of folded-saddle and jump-on canards. *Preprint (submitted)*, 2015.
- [32] F. Diener and M. Diener. *Nonstandard analysis in practice*. Springer-Verlag, Berlin/New York, 1995.
- [33] M. Diener. The canard unchained or how fast/slow dynamical systems bifurcate. *The Mathematical Intelligencer*, 6(3):38–49, 1984.
- [34] E. J. Doedel. Nonlinear numerics. *Journal of the Franklin Institute*, 334(5-6):1049–1073, 1997.
- [35] E. J. Doedel. Lecture notes on numerical analysis of nonlinear equations. In B. Krauskopf, H. M. Osinga, and J. Galán-Vioque, editors, *Numerical Continuation Methods for Dynamical Systems: Path following and boundary value problems*, pages 1–50. Springer-Verlag, New York, 2007.

- [36] E. J. Doedel, H. B. Keller, and J.-P. Kernévez. Numerical analysis and control of bifurcation problems. i: Bifurcation in finite dimensions. *International Journal of Bifurcation and Chaos*, **1**(03): 493–520, 1991.
- [37] E. J. Doedel, H. B. Keller, and J.-P. Kernévez. Numerical analysis and control of bifurcation problems. ii: Bifurcation in infinite dimensions. *International Journal of Bifurcation and Chaos*, **1**(04):745–772, 1991.
- [38] E. J. Doedel, A. R. Champneys, T. F. Fairgrieve, Yu. A. Kuznetsov, B. E. Oldeman, R. C. Paffenroth, B. Sandstede, X. J. Wang, and C. Zhang. Auto-07p: Continuation and bifurcation software for ordinary differential equations. Available at <http://cmvl.cs.concordia.ca/auto>, 2007.
- [39] F. Dumortier. Compactification and desingularization of spaces of polynomial Liénard equations. *Journal of Differential Equations*, **224**(2):296–313, 2006.
- [40] F. Dumortier. Canard explosion and position curves. In A. Johann, H.-P. Kruse, F. Rupp, and S. Schmitz, editors, *Recent Trends in Dynamical Systems*, pages 51–78. Springer, 2013.
- [41] F. Dumortier and R. Roussarie. Canard cycles and center manifolds. *Memoirs of the American Mathematical Society*, **121**(577), 1996.
- [42] F. Dumortier and R. Roussarie. Bifurcation of relaxation oscillations in dimension two. *Discrete and Continuous Dynamical Systems - Series A*, **19**(4):631–674, 2007.
- [43] F. Dumortier, D. Panazzolo, and R. Roussarie. More limit cycles than expected in Liénard equations. *Proceedings of the American Mathematical Society*, **135**(6):1895–1904, 2007.
- [44] W. Eckhaus. Relaxation oscillations including a standard chase on French ducks. In F. Verhulst, editor, *Asymptotic Analysis II*, volume **985** of *Lecture Notes in Math.*, pages 449–494. Springer-Verlag, New York, 1983.
- [45] J. P. England, B. Krauskopf, and H. M. Osinga. Computing one-dimensional global manifolds of Poincaré maps by continuation. *SIAM Journal on Applied Dynamical Systems*, **4**(4):1008–1041, 2005.
- [46] J. P. England, B. Krauskopf, and H. M. Osinga. Computing two-dimensional global invariant manifolds in slow–fast systems. *International Journal of Bifurcation and Chaos*, **17**(03):805–822, 2007.
- [47] G. B. Ermentrout. *Simulating, analyzing, and animating dynamical systems: a guide to XPPAUT for researchers and students*. SIAM, 2002.
- [48] G. B. Ermentrout and N. J. Kopell. Parabolic bursting in an excitable system coupled with a slow oscillation. *SIAM Journal on Applied Mathematics*, **46**(2):233–253, 1986.
- [49] N. Fenichel. Persistence and smoothness of invariant manifolds. *Indiana University Mathematical Journal*, **21**(3):193–226, 1971.
- [50] N. Fenichel. Asymptotic stability with rate conditions. *Indiana University Mathematical Journal*, **23**(12):1109–1137, 1974.
- [51] N. Fenichel. Asymptotic stability with rate conditions II. *Indiana University Mathematical Journal*, **26**(1):81–93, 1977.
- [52] N. Fenichel. Geometric singular perturbation theory. *Journal of Differential Equations*, **31**(1): 53–98, 1979.

- [53] R. FitzHugh. Mathematical models of threshold phenomena in the nerve membrane. *The bulletin of mathematical biophysics*, **17**(4):257–278, 1955.
- [54] R. FitzHugh. Impulses and physiological states in theoretical models of nerve membrane. *Biophysical journal*, **1**(6):445, 1961.
- [55] J.-P. Francoise. *Oscillations en biologie: analyse qualitative et modèles*. Springer-Verlag, Berlin/New York, 2005.
- [56] A. Ghosh, D. Roy, and V. K. Jirsa. Simple model for bursting dynamics of neurons. *Physical Review E*, **80**(4):041930, 2009.
- [57] J.-M. Ginoux and B. Rossetto. Differential geometry and mechanics: Applications to chaotic dynamical systems. *International Journal of Bifurcation and Chaos*, **16**(04):887–910, 2006.
- [58] M. Golubitsky and D. G. Schaeffer. *Singularities and Groups in Bifurcation Theory, vol. 1*. Springer-Verlag, New York, 1988.
- [59] M. Golubitsky, K. Josić, and T. J. Kaper. An unfolding theory approach to bursting in fast-slow systems. In H. W. Broer, B. Krauskopf, and G. Vegter, editors, *Global analysis of dynamical systems: Festschrift dedicated to Floris Takens on the occasion of his 60th birthday*, pages 277–308. Institute of Physics Publishing, Bristol, 2001.
- [60] J. Guckenheimer. Computing periodic orbits. In J. L. Lumley, editor, *Fluid Mechanics and the Environment: Dynamical Approaches*, pages 117–119, Berlin/New York, 2001. Springer.
- [61] J. Guckenheimer. Return maps of folded nodes and folded saddle-nodes. *Chaos*, **18**(1):015108, 2008.
- [62] J. Guckenheimer. Singular Hopf bifurcation in systems with two slow variables. *SIAM Journal on Applied Dynamical Systems*, **7**(4):1355–1377, 2008.
- [63] J. Guckenheimer and R. Haiduc. Canards at folded nodes. *Moscow Mathematical Journal*, **5**(1):91–103, 2005.
- [64] J. Guckenheimer and P. Holmes. *Nonlinear oscillations, dynamical systems, and bifurcations of vector fields*. Springer, 1983.
- [65] J. Guckenheimer and C. Kuehn. Computing slow manifolds of saddle type. *SIAM Journal on Applied Dynamical Systems*, **8**(3):854–879, 2009.
- [66] J. Guckenheimer and M. D. LaMar. Periodic orbit continuation in multiple time scale systems. In B. Krauskopf, H. M. Osinga, and J. Gálan-Vioque, editors, *Numerical Continuation Methods for Dynamical Systems*, pages 253–267. Springer, 2007.
- [67] J. Guckenheimer and B. Meloon. Computing periodic orbits and their bifurcations with automatic differentiation. *SIAM Journal on Scientific Computing*, **22**(3):951–985, 2001.
- [68] J. Guckenheimer, K. Hoffman, and W. Weckesser. Numerical computation of canards. *International Journal of Bifurcation and Chaos*, **10**(12):2669–2688, 2000.
- [69] M. E. Henderson. Multiple parameter continuation: Computing implicitly defined k-manifolds. *International Journal of Bifurcation and Chaos*, **12**(03):451–476, 2002.
- [70] J. L. Hindmarsh and R. M. Rose. A model of the nerve impulse using two first-order differential equations. *Nature*, **296**:163–164, 1982.
- [71] J. L. Hindmarsh and R. M. Rose. A model of neuronal bursting using three coupled first order differential equations. *Proceedings of the Royal society of London. Series B: Biological sciences*, **221**(1222):87–102, 1984.

- [72] M. W. Hirsch, C. C. Pugh, and M. Shub. *Invariant Manifolds*, volume 583 of *Lecture Notes in Mathematics*. Springer-Verlag, Berlin/New York, 1977.
- [73] A. L. Hodgkin and A. F. Huxley. A quantitative description of membrane current and its application to conduction and excitation in nerve. *The Journal of physiology*, 117(4):500–544, 1952.
- [74] J. L. Hudson, M. Hart, and D. Marinko. An experimental study of multiple peak periodic and nonperiodic oscillations in the Belousov–Zhabotinskii reaction. *The Journal of Chemical Physics*, 71(4):1601–1606, 1979.
- [75] E. M. Izhikevich. Subcritical elliptic bursting of Bautin type. *SIAM Journal on Applied Mathematics*, 60(2):503–535, 2000.
- [76] E. M. Izhikevich. Neural excitability, spiking and bursting. *International Journal of Bifurcation and Chaos*, 10(06):1171–1266, 2000.
- [77] E. M. Izhikevich. Synchronization of elliptic bursters. *SIAM Review*, 43(2):315–344, 2001.
- [78] E. M. Izhikevich. *Dynamical systems in neuroscience*. MIT press, 2007.
- [79] C. K. R. T. Jones. Geometric singular perturbation theory. In R. Johnson, editor, *Dynamical Systems, C.I.M.E Lectures, Montecatini Terme, June 1994*, volume 1609 of *Lecture Notes in Mathematics*, pages 44–120. Springer-Verlag, Berlin/New York, 1995.
- [80] T. J. Kaper. An introduction to geometric methods and dynamical systems theory for singular perturbation problems. In *Proceedings of Symposia in Applied Mathematics*, volume 56, pages 85–132. American Mathematical Society, 1999.
- [81] T. J. Kaper and C. K. R. T. Jones. A primer on the exchange lemma for fast-slow systems. In C. K. R. T. Jones and A. I. Khibnik, editors, *Multiple-time-scale dynamical systems*, volume 122 of *IMA Volumes in Mathematics and its Applications*, pages 65–87. Springer, 2001.
- [82] J. Keener and J. Sneyd. *Mathematical Physiology*. Springer-Verlag, Berlin/New York, 1998.
- [83] J. K. Kevorkian and D. Cole. *Multiple scale and singular perturbation methods*. Springer-Verlag, 1996.
- [84] T. Kispersky, J. A. White, and H. G. Rotstein. The mechanism of abrupt transition between theta and hyper-excitable spiking activity in medial entorhinal cortex layer II stellate cells. *PloS one*, 5(11):e13697, 2010.
- [85] M. T. M. Koper. Bifurcations of mixed-mode oscillations in a three-variable autonomous Van der Pol-Duffing model with a cross-shaped phase diagram. *Physica D*, 80(1–2):72–94, 1995.
- [86] M. A. Kramer, R. D. Traub, and N. J. Kopell. New dynamics in cerebellar purkinje cells: torus canards. *Physical Review Letters*, 101(6):068103, 2008.
- [87] B. Krauskopf and H. M. Osinga. Computing geodesic level sets on global (un)stable manifolds of vector fields. *SIAM Journal on Applied Dynamical Systems*, 2(4):546–569, 2003.
- [88] B. Krauskopf and H. M. Osinga. Computing invariant manifolds via the continuation of orbit segments. In B. Krauskopf, H. M. Osinga, and J. Galán-Vioque, editors, *Numerical Continuation Methods for Dynamical Systems: Path following and boundary value problems*, pages 117–154. Springer-Verlag, New York, 2007.
- [89] B. Krauskopf, H. M. Osinga, E. J. Doedel, M. E. Henderson, J. Guckenheimer, A. Vladimírsky, M. Dellnitz, and O. Junge. A survey of methods for computing (un)stable manifolds of vector fields. *International Journal of Bifurcation and Chaos*, 15(03):763–791, 2005.



- [90] M. Krupa and P. Szmolyan. Extending slow manifolds near transcritical and pitchfork singularities. *Nonlinearity*, **14**(6):1473–1491, 2001.
- [91] M. Krupa and P. Szmolyan. Relaxation oscillation and canard explosion. *Journal of Differential Equations*, **174**(2):312–368, 2001.
- [92] M. Krupa and P. Szmolyan. Extending geometric singular perturbation theory to nonhyperbolic points—fold and canard points in two dimensions. *SIAM Journal on Mathematical Analysis*, **33**(2):286–314, 2001.
- [93] M. Krupa and M. Wechselberger. Local analysis near a folded saddle-node singularity. *Journal of Differential Equations*, **248**(12):2841–2888, 2010.
- [94] M. Krupa, N. Popović, and N. Kopell. Mixed-mode oscillations in three time-scale systems: A prototypical example. *SIAM Journal on Applied Dynamical Systems*, **7**(2):361–420, 2008.
- [95] S. S. Kumar and P. S. Buckmaster. Hyperexcitability, interneurons, and loss of GABAergic synapses in entorhinal cortex in a model of temporal lobe epilepsy. *The Journal of neuroscience*, **26**(17):4613–4623, 2006.
- [96] P. A. Lagerstrom. *Matched asymptotic expansions: ideas and techniques*. Springer-Verlag, 1988.
- [97] D. Linaro, A. R. Champneys, M. Desroches, and M. Storace. Codimension-two homoclinic bifurcations underlying spike adding in the hindmarsh–rose burster. *SIAM Journal on Applied Dynamical Systems*, **11**(3):939–962, 2012.
- [98] A. Lins, W. De Melo, and C. C. Pugh. On Liénard’s equation. In *Geometry and topology (Proc. III Latin Amer. School of Math., Inst. Mat. Pura Aplicada CNPq, Rio de Janeiro, 1976)*, volume **597** of *Lecture Notes in Mathematics*, pages 335–357. Springer, Berlin, 1977.
- [99] P. De Maesschalck. Gevrey normal form for nilpotent contact points of order two. *Discrete and Continuous Dynamical Systems Series A*, **34**(2):677–688, 2014.
- [100] P. De Maesschalck and M. Desroches. Numerical continuation techniques for planar slow-fast systems. *SIAM Journal on Applied Dynamical Systems*, **12**(3):1159–1180, 2013.
- [101] P. De Maesschalck and F. Dumortier. Time analysis and entry-exit relation near planar turning points. *J. Differential Equations*, **215**(2):225–267, 2005.
- [102] P. De Maesschalck and F. Dumortier. Classical Liénard equations of degree  $n \geq 6$  can have  $\lfloor \frac{n-1}{2} \rfloor + 2$  limit cycles. *J. Differential Equations*, **250**(4):2162–2176, 2011.
- [103] P. De Maesschalck and F. Dumortier. Bifurcations of multiple relaxation oscillations in polynomial Liénard equations. *Proceedings of the American Mathematical Society*, **139**(6):2073–2085, 2011.
- [104] P. De Maesschalck, F. Dumortier, and R. Roussarie. Cyclicity of common canard cycles. *Indagationes Mathematicae*, **22**(3):165–206, 2011.
- [105] F. Marino, G. Catalán, P. Sánchez, S. Balle, and O. Piro. Thermo-optical “canard orbits” and excitable limit cycles. *Physical Review Letters*, **92**(7):73901, 2004.
- [106] MATHEMATICA. Wolfram Research, Inc. *Champaign, IL*, 1988–2015.
- [107] G. S. Medvedev. Transition to bursting via deterministic chaos. *Physical Review Letters*, **97**(4):048102, 2006.
- [108] A. Milik and P. Szmolyan. Multiple time scales and canards in a chemical oscillator. In C. K. R. T. Jones and A. I. Khibnik, editors, *Multiple time scale dynamical systems*, volume **122** of *IMA Volumes in Mathematics and its Applications*, pages 117–140. Springer, 2001.

- [109] A. Milik, P. Szmolyan, H. Löffelmann, and E. Gröller. Geometry of mixed-mode oscillations in the 3-D autocatalator. *International Journal of Bifurcation and Chaos*, 8(03):505–519, 1998.
- [110] E. F. Mishchenko and N. Kh. Rozov. *Differential equations with small parameters and relaxation oscillations (translated from Russian)*. Plenum Press, 1980.
- [111] E. F. Mishchenko, Yu. S. Kolesov, A. Yu. Kolesov, and N. Kh. Rhozov. *Asymptotic Methods in Singularly Perturbed Systems*. Monographs in Contemporary Mathematics. Consultants Bureau, New York, 1994.
- [112] J. Mitry, M. McCarthy, N. J. Kopell, and M. Wechselberger. Excitable neurons, firing threshold manifolds and canards. *The Journal of Mathematical Neuroscience (JMN)*, 3(12), 2013.
- [113] J. Moehlis. Canards for a reduction of the Hodgkin–Huxley equations. *Journal of mathematical biology*, 52(2):141–153, 2006.
- [114] J. S. Nagumo, S. Arimoto, and S. Yoshizawa. An active pulse transmission line simulating nerve axon. *Proceedings of the IRE*, 50(10):2061–2070, 1962.
- [115] J. Nowacki, H. M. Osinga, and K. Tsaneva-Atanasova. Dynamical systems analysis of spike-adding mechanisms in transient bursts. *The Journal of Mathematical Neuroscience (JMN)*, 2(1), 2012.
- [116] M. Okuda. A new method of nonlinear analysis for shaping and threshold actions. *Journal of the Physical Society of Japan*, 41(5):1815–1816, 1976.
- [117] F. W. J. Olver, D. W. Lozier, R. F. Boisvert, and C. W. Clark. *NIST handbook of mathematical functions*. Cambridge University Press, 2010.
- [118] H. M. Osinga and K. Tsaneva-Atanasova. Dynamics of plateau bursting depending on the location of its equilibrium. *Journal of Neuroendocrinology*, 22(12):1301–1314, 2010.
- [119] B. Peng, V. Gaspar, and K. Showalter. False bifurcations in chemical systems: canards. *Philosophical Transactions of the Royal Society of London. Series A: Physical and Engineering Sciences*, 337(1646):275–289, 1991.
- [120] B. Percha, R. Dzakpasu, M. Żochowski, and J. Parent. Transition from local to global phase synchrony in small world neural network and its possible implications for epilepsy. *Physical Review E*, 72(3):031909, 2005.
- [121] R. E. Plant. The effects of calcium++ on bursting neurons. a modeling study. *Biophysical journal*, 21(3):217, 1978.
- [122] R. E. Plant. Bifurcation and resonance in a model for bursting nerve cells. *Journal of Mathematical Biology*, 11(1):15–32, 1981.
- [123] R. E. Plant and M. Kim. On the mechanism underlying bursting in the aplysia abdominal ganglion R15 cell. *Mathematical Biosciences*, 26(3):357–375, 1975.
- [124] R. E. Plant and M. Kim. Mathematical description of a bursting pacemaker neuron by a modification of the hodgkin-huxley equations. *Biophysical journal*, 16(3):227, 1976.
- [125] J. Platkiewicz and R. Brette. A threshold equation for action potential initiation. *PLoS computational biology*, 6(7):e1000850, 2010.
- [126] S. A. Prescott, Y. De Koninck, and T. J. Sejnowski. Biophysical basis for three distinct dynamical mechanisms of action potential initiation. *PLoS computational biology*, 4(10):e1000198, 2008.

- [127] W. C. Rheinboldt. *Numerical analysis of parametrized nonlinear equations*. Wiley-Interscience, 1986.
- [128] F. Rieke, D. Warland, R. de Ruyter van Steveninck, and W. Bialek. *Spikes: exploring the neural code*. MIT press, 1999.
- [129] J. Rinzel. Excitation dynamics: insights from simplified membrane models. *Federation Proceedings*, **44**(15):2944–2946, 1985.
- [130] J. Rinzel. A formal classification of bursting mechanisms in excitable systems. In *Proceedings of the International Congress of Mathematicians*, volume **1**, pages 1578–1593, 1986.
- [131] J. Rinzel and Y. S. Lee. Dissection of a model for neuronal parabolic bursting. *Journal of Mathematical Biology*, **25**(6):653–675, 1987.
- [132] A. Rossokhin and Y. Saakyan. Study of the dependence of the generation threshold of the nerve impulse on the mode of formation of the input signal on the basis of the hodgkin-huxley model. *Biophysics*, **37**(6):969–973, 1992.
- [133] H. G. Rotstein, N. N. Kopell, A. M. Zhabotinsky, and I. R. Epstein. Canard phenomenon and localization of oscillations in the belousov–zhabotinsky reaction with global feedback. *The Journal of chemical physics*, **119**(17):8824–8831, 2003.
- [134] R. Roussarie. Putting a boundary to the space of Liénard equations. *Discrete and Continuous Dynamical Systems. Series A*, **17**(2):441–448, 2007.
- [135] J. E. Rubin and M. Wechselberger. Giant squid – hidden canard: the 3D geometry of the Hodgkin-Huxley model. *Biological Cybernetics*, **97**(1):5–32, 2007.
- [136] J. E. Rubin and M. Wechselberger. The selection of mixed-mode oscillations in a Hodgkin-Huxley model with multiple timescales. *Chaos*, **18**(1):015105, 2008.
- [137] I. Samengo, G. Mato, D. H. Elijah, S. Schreiber, and M. A. Montemurro. Linking dynamical and functional properties of intrinsically bursting neurons. *Journal of Computational Neuroscience*, **35**(2):213–230, 2013.
- [138] M. Sekerli, C. A. Del Negro, R. H. Lee, and R. J. Butera. Estimating action potential thresholds from neuronal time-series: new metrics and evaluation of methodologies. *Biomedical Engineering, IEEE Transactions on*, **51**(9):1665–1672, 2004.
- [139] R. Seydel. *Practical bifurcation and stability analysis, Third edition*. Springer, 2010.
- [140] A. Shil’nikov and G. Cymbalyuk. Transition between tonic spiking and bursting in a neuron model via the blue-sky catastrophe. *Physical Review Letters*, **94**(4):048101, 2005.
- [141] K. Showalter, R. M. Noyes, and K. Bar-Eli. A modified oregonator model exhibiting complicated limit cycle behavior in a flow system. *The Journal of Chemical Physics*, **69**(6):2514–2524, 1978.
- [142] P. Smolen, D. Terman, and J. Rinzel. Properties of a bursting model with two slow inhibitory variables. *SIAM Journal on Applied Mathematics*, **53**(3):861–892, 1993.
- [143] C. Soto-Treviño, N. J. Kopell, and D. Watson. Parabolic bursting revisited. *Journal of Mathematical Biology*, **35**(1):114–128, 1996.
- [144] P. Szmolyan and M. Wechselberger. Canards in  $\mathbb{R}^3$ . *Journal of Differential Equations*, **177**(2):419–453, 2001.

- [145] F. Takens. Constrained equations, a study of implicit differential equations and their discontinuous solutions. In P. Hilton, editor, *Structural Stability, the Theory of Catastrophes and Applications in the Sciences*, volume 525 of *Lecture Notes in Mathematics*, pages 143–234. Springer-Verlag, New York, 1976.
- [146] D. Terman. Chaotic spikes arising from a model of bursting in excitable membranes. *SIAM Journal on Applied Mathematics*, 51(5):1418–1450, 1991.
- [147] D. Terman. The transition from bursting to continuous spiking in excitable membrane models. *Journal of Nonlinear Science*, 2(2):135–182, 1992.
- [148] A. N. Tikhonov, A. B. Vasil'eva, and A. G. Sveshnikov. *Differential Equations*. Springer Series in Soviet Mathematics. Springer-Verlag, 1985.
- [149] K. Tsaneva-Atanasova, H. M. Osinga, T. Rieß, and A. Sherman. Full system bifurcation analysis of endocrine bursting models. *Journal of theoretical biology*, 264(4):1133–1146, 2010.
- [150] L. E. Tsitolovsky and N. V. Babkina. Neurons evaluate both the amplitude and the meaning of signals. *Brain Research*, 946(1):104–118, 2002.
- [151] L. E. Tsitolovsky and A. Shvedov. Instrumental conditioning of the activity of putative command neurons in the mollusk helix. *Brain Research*, 745(1):271–282, 1997.
- [152] B. van der Pol. A theory of the amplitude of free and forced triode vibrations. *Radio Review*, 1:701–710, 754–762, 1920.
- [153] B. van der Pol. On “Relaxation Oscillations” I. *Philosophical Magazine Series 7*, 2(11):978–992, 1926.
- [154] B. van der Pol. The nonlinear theory of electric oscillations. *Proceedings of the Institute of Radio Engineers*, 9(22):1051–1086, 1934.
- [155] M. Wechselberger. Extending Melnikov theory to invariant manifolds on non-compact domains. *Dynamical Systems: An International Journal*, 17(3):215–233, 2002.
- [156] M. Wechselberger. Existence and bifurcations of canards in  $\mathbb{R}^3$  in the case of a folded node. *SIAM Journal on Applied Dynamical Systems*, 4(1):101–139, 2005.
- [157] A. T. Winfree. Spiral waves of chemical activity. *Science*, 175(4022):634–636, 1972.
- [158] J. Wojcik and A. Shilnikov. Voltage interval mappings for activity transitions in neuron models for elliptic bursters. *Physica D*, 240(14):1164–1180, 2011.